



January 2020

Detection And Characteristics Of Blowing Snow At McMurdo Station, Antarctica During The Aware Field Campaign

Nicole Loeb

Follow this and additional works at: <https://commons.und.edu/theses>

Recommended Citation

Loeb, Nicole, "Detection And Characteristics Of Blowing Snow At McMurdo Station, Antarctica During The Aware Field Campaign" (2020). *Theses and Dissertations*. 3381.
<https://commons.und.edu/theses/3381>

This Thesis is brought to you for free and open access by the Theses, Dissertations, and Senior Projects at UND Scholarly Commons. It has been accepted for inclusion in Theses and Dissertations by an authorized administrator of UND Scholarly Commons. For more information, please contact und.common@library.und.edu.

DETECTION AND CHARACTERISTICS OF BLOWING SNOW AT MCMURDO
STATION, ANTARCTICA DURING THE AWARE FIELD CAMPAIGN

by

Nicole Amber Loeb
Bachelor of Science, University of Manitoba, 2018

A Thesis
Submitted to the Graduate Faculty
of the
University of North Dakota
in partial fulfillment of the requirements

for the degree of
Master of Science


Grand Forks, North Dakota

December
2020

Copyright 2020 Nicole Loeb

Name: Nicole Loeb
Degree: Master of Science

This document, submitted in partial fulfillment of the requirements for the degree from the University of North Dakota, has been read by the Faculty Advisory Committee under whom the work has been done and is hereby approved.

DocuSigned by:

770518977679460...

Aaron Kennedy

DocuSigned by:

104ECAF70EE940A...

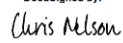
Michael Poellot

DocuSigned by:

780F0C9F1355746C...

David Delene

This document is being submitted by the appointed advisory committee as having met all the requirements of the School of Graduate Studies at the University of North Dakota and is hereby approved.

DocuSigned by:

2E0AF088C733403...

Chris Nelson
Dean of the School of Graduate Studies

11/24/2020

Date

PERMISSION

Title Detection and characteristics of blowing snow at McMurdo Station,
 Antarctica during the AWARE Field Campaign

Department Atmospheric Sciences

Degree Master of Science

In presenting this thesis in partial fulfillment of the requirements for a graduate degree from the University of North Dakota, I agree that the library of this University shall make it freely available for inspection. I further agree that permission for extensive copying for scholarly purposes may be granted by the professor who supervised my thesis work or, in his absence, by the Chairperson of the department or the dean of the School of Graduate Studies. It is understood that any copying or publication or other use of this thesis or part thereof for financial gain shall not be allowed without my written permission. It is also understood that due recognition shall be given to me and to the University of North Dakota in any scholarly use which may be made of any material in my thesis.

Nicole Amber Loeb
24 November 2020

TABLE OF CONTENTS

LIST OF FIGURES	iii
LIST OF TABLES	viii
ACKNOWLEDGMENTS	x
ABSTRACT	xi
CHAPTER 1. BACKGROUND & INTRODUCTION	1
1.1. Impacts of Blowing Snow	1
1.2. Properties of Blowing Snow	4
1.2.1. Physical Process of Blowing Snow	4
1.2.2. Microphysical Properties of Blowing Snow	6
1.3. Remote-Sensing Observations of Blowing Snow	7
1.3.1. Ground-Based Remote-Sensing of Blowing Snow	8
1.3.2. Satellite-Based Remote-Sensing of Blowing Snow	9
1.4. Blowing Snow in Antarctica	10
1.4.1. Importance of Blowing Snow in the Antarctic Climate	10
1.4.2. 2016 AWARE Field Campaign	12
1.5. Objectives	13

CHAPTER 2: DATA SOURCES	21
2.1. Human Observations	21
2.2. AMF2 Instrumentation	22
2.2.1. Meteorological Instrumentation at the AMF2	22
2.2.2. Parsivel ² Optical Disdrometer	24
2.2.3. Vaisala CL31 Ceilometer	26
2.2.4. High Spectral Resolution Lidar	27
2.2.5. Sky Radiometers for Downwelling Radiation	28
2.2.6. Micropulse Lidar	29
2.2.7. Ka-band ARM Zenith Radar	30
2.2.8. Summary of Remote Sensing Instrumentation	31
CHAPTER 3: METHODOLOGY	49
3.1. Climatology of Human Observations of Blowing Snow at McMurdo Station	49
3.2. Ceilometer-Based Blowing Snow Detection Algorithm	49
3.3. A Revised Blowing Snow Detection Algorithm	51
3.3.1. Temporal Averaging	51
3.3.2. Meteorological Thresholds	52
3.4. Assessment of Algorithm Performance	52

3.5. Multi-Instrument Blowing Snow Depth Estimation	53
3.5.1. Attenuated Backscatter Coefficient	54
3.5.2. Linear Depolarization Ratio	55
3.5.3. Color Ratio	56
3.5.4. Probabilistic Blowing Snow Depth Estimation	57
3.5.5. Blowing Snow Depth Assessment Methods.....	58
CHAPTER 4: CASE STUDIES.....	69
4.1. 4-5 July 2016.....	69
4.2. 2 July 2016	71
4.3. 12 June 2016.....	72
CHAPTER 5: RESULTS AND DISCUSSION	81
5.1. Human-Observed Climatology of Blowing Snow	81
5.2. Blowing Snow Detection Algorithm Results.....	82
5.2.1. Comparison to Human Observations.....	82
5.2.2. Sensitivity Testing	85
5.2.3. Fog.....	87
5.2.4. Parsivel ² Particle Observations.....	88
5.3. Probabilistic Blowing Snow Algorithm Results	90

5.3.1. Criteria Analysis	90
5.3.2. Probabilistic Blowing Snow Depth	90
5.3.3. Sensitivity Testing	94
5.4. Environmental Properties of Blowing Snow	96
5.4.1. Blowing Snow Occurrence by Meteorological Variables	96
5.4.2. Connections Between Blowing Snow Depth and Meteorological Variables ..	98
CHAPTER 6: CONCLUSIONS	134
APPENDIX A: List of Instrumentation at the AMF2	139
REFERENCES	141

LIST OF FIGURES

Figure	Page
1. Temporal evolution of temperature (black) and moisture (red) structure during a BLSN event. Figure adapted from Palm et al. (2018).	16
2. Graphic depiction of the movement of particles in BLSN and its effect on the vertical wind profile (adapted from Nishimura and Nemoto 2005). The dotted line represents the top of the snowpack, and the dashed line represents the top of the saltation layer. Z represents altitude, $U(z)$ represents the initial vertical wind speed profile, and $U'(z)$ represents the vertical wind speed profile altered due to BLSN. Transport is initiated by the wind at A. Collisions with the snowpack occur at B, dislodging more particles to be transported. Particles begin to be carried in suspension by the wind at C.	17
3. Image from Dr. Aaron Kennedy's snowflake camera in Grand Forks, North Dakota at 07:31:13 UTC on 12 February 2020 showing several broken snow crystals (appearing as brighter particles) surrounded by other fragmented (darker) BLSN particles.....	18
4. Average winter (April - October) (a) BLSN frequency and (b) average annual sublimation from 2007-2015 based on CALIPSO and MERRA-2 data (Palm et al. 2017).	19
5. Map showing the location of McMurdo Station and the Western Antarctic Ice Sheet field site.....	20
6. Daily Observation Worksheet from McMurdo Station, Antarctica for 12 June 2016.	32
7. MET instrumentation at the DOE ARM Southern Great Plains site (Ritsche and Prell 2011).....	33
8. 5-minute mean a) 10 m wind speed, b) 2 m visibility, and c) 2 m RH at McMurdo Station on 12 June 2016 from the MET datastream.	34
9. Image of a Parisvel ² optical disdrometer at the University of North Dakota Oakville Prairie Observatory taken by Aaron Kennedy.	35
10. Logarithmic 1-min particle size densities at McMurdo Station on 12 June 2016 measured by the Parisvel2.	36

11. Image of the Vaisala CL31 ceilometer at Princess Elisabeth station in Eastern Antarctica. Figure adapted from Gossart et al. (2017).	38
12. Logarithmic backscatter coefficient and lowest detected cloud base height (shown in black) detected by a Vaisala CL31 ceilometer at McMurdo Station on 12 June 2016.	39
13. Image of a HSRL with its protective cover removed (Goldsmith 2016). The protective covering is shown behind the HSRL.	40
14. 5-minute average a) attenuated backscatter coefficient and b) linear depolarization ratio from the HSRL for 12 June 2016 at McMurdo Station.	41
15. 5-minute mean a) attenuated backscatter coefficient and b) linear depolarization ratio from the MPL for 12 June 2016 at McMurdo Station.	43
16. Image of the KAZR deployed at DOE ARM Southern Great Plains site (Widener et al. 2012).	45
17. 5-minute mean a) radar reflectivity and b) mean Doppler velocity at McMurdo Station on 12 June 2016 measured by KAZR.	46
18. Flowchart describing the BLSN detection algorithm (adapted from Gossart et al. 2017).	59
19. Diagrams of (a) clear-sky BLSN, (b) clouds/precipitation with BLSN, and (c) heavy mixed events. Orange and dark blue lines represent the clear-sky signal and idealized backscatter coefficient profile from the ceilometer, respectively.	60
20. 95 th percentile clear sky backscatter profile for McMurdo Station during the AWARE Campaign. The lowest 100 m of the profile is highlighted in the inset.	61
21. Clear sky 30 m averaged attenuated backscatter coefficient profiles for the ceilometer (CEIL), MPL, and HSRL.	63
22. Flowchart describing the BLSN depth detection algorithm applied to backscatter coefficient profiles from the ceilometer (CEIL), MPL, and HSRL.	65
23. Flowchart describing the BLSN depth detection algorithm applied to LDR profiles from the MPL and HSRL.	66

24. Flowchart describing the BLSN depth detection algorithm applied to color ratio profiles.	67
25. a) Human observations, b) five-minute average ceilometer attenuated backscatter coefficient, c) five-minute average Parsivel ² particle number density, and d) five-minute average wind speed (green), visibility (orange), and RH (blue) from MET instrumentation on 4-5 July 2016 at McMurdo Station. BLSN tops derived from the five-minute algorithm are denoted by black stars, diamonds, and dots corresponding to Categories 1, 2, and 3, respectively.	75
26. a) 5-minute averaged ceilometer backscatter coefficient (as used in the 5-min algorithm), b) 30 m averaged ceilometer backscatter coefficient, c) MPL backscatter coefficient, d) MPL LDR, e) HSRL backscatter coefficient, f) color ratio, and g) probabilistic algorithm results for 4-5 July 2016. Black dots indicate the top of the BLSN plume as indicated by the single algorithm. The gray line shows the BLSN depth indicated by the probabilistic algorithm.	76
27. As in Figure 25, but for 2 July 2016.	77
28. As in Figure 26, but for 2 July 2016.	78
29. As in Figure 25, but for 12 June 2016.	79
30. As in Figure 26, but for 12 June 2016.	80
31. Boxplots of a) annual and b) monthly frequencies of BLSN from human observations at McMurdo Station, Antarctica. The box represents the interquartile range of the distribution, and the whiskers cover the minimum and maximum of the data within 1.5 times the interquartile range of the median. Observations falling outside of the whiskers (outliers) are shown as empty black circles. The orange solid and green dashed lines represent the median and mean of the distribution, respectively. Red dots show the observed frequency in 2016 during the AWARE Campaign.	100
32. Seasonal proportion of human BLSN observations occurring with other phenomena at McMurdo Station. a) Climatological average for 2002 to 2018 and b) during the AWARE campaign.	101
33. Monthly hours of BLSN detected by humans, ceilometer-based algorithms, and the visibility sensor during the 2016 AWARE campaign.	102

34. Monthly hours of BLSN detected by a) the Gossart algorithm, b) the 5-min NT algorithm, and c) the 5-min algorithm, divided into the category of BLSN detected. Monthly hours of human-observed BLSN are shown in black for comparison.....	104
35. Percent correct by month for each algorithm during 2016.	105
36. Monthly hours of fog and BLSN separated by category for the 5-min algorithm with varied RH thresholds. Human observations are shown in black dots.	109
37. a) Boxplots showing the distribution of mean particle counts from the Parsivel ² for each category based on the five-minute algorithm. The orange solid and green dashed lines represent the median and mean of the distribution, respectively. b) Mean particle number density distributions from Parsivel ² for each category.	110
38. Logarithmic particle number density distributions from the Parsivel ² for 2 m s ⁻¹ wind speed increments for a) AWARE Campaign observations, b) observations from the Phoenix APS site, and c) BLOWN-UNDER.....	111
39. Monthly hours of BLSN for each algorithm and human observations of BLSN with and without falling snow during a) all BLSN detected by the five-minute algorithm, and b) only Category 3 BLSN.	112
40. Monthly cases (blue bars) mean BLSN depth (black line) detected by the probabilistic algorithm.....	114
41. Boxplots of detected BLSN depth for the probabilistic algorithm and five-minute algorithm for the 41 case days, and the five-minute algorithm for all of 2016. The box represents the interquartile range of the distribution, and the whiskers cover the minimum and maximum of the data within 1.5 times the interquartile range of the median. Observations falling outside of the whiskers (outliers) are shown as black dots. Orange (green) lines show the median (mean) depth of the distribution.....	115
42. Histograms of BLSN depths detected by a) the five-minute algorithm and b) the probabilistic algorithm for the 41 case days.....	116
43. Histograms of the differences between the probabilistic and five-minute BLSN depths (probabilistic - 5 min) for each category.....	117

44. Two-dimensional histograms of probabilistic vs. five-minute algorithm BLSN depths. The dashed lines represent the 1:1 relationship.	118
45. Two-dimensional histograms of BLSN depth vs. depth detected by the contributing algorithms. The dashed lines represent the 1:1 relationship.	120
46. Boxplots of BLSN depths detected by the 30 m CEIL algorithm for the various sensitivity tests. Sensitivity tests are as defined in Table 15. Orange (green) line shows the median (mean) depth of the distribution.	123
47. As in Figure 46, but for the MPL BS algorithm.	124
48. As in Figure 46, but for the HSRL BS algorithm.	125
49. As in Figure 46, but for the MPL LDR algorithm.	126
50. As in Figure 46, but for the HSRL LDR algorithm.	127
51. As in Figure 46, but for the CR algorithm.	128
52. As in Figure 46, but for the probabilistic depth algorithm.	129
53. Two-dimensional histograms of a) 2 m visibility versus 10 m wind speed, and b) wind speed versus temperature for all BLSN detections by the five-minute algorithm. Dots in a) denoted the visibility bin with the highest occurrence for each wind speed bin. The dashed line in b) shows the relationship derived by Li and Pomeroy (1997b).	130
54. Percent of observations in each wind speed/temperature bin associated with BLSN detections. Bins are as those shown in Figure 53b. The dashed line shows the relationship derived by Li and Pomeroy (1997b).	131
55. Distribution of 10 m wind direction occurrence for each five-minute period during 2016 for a) all times and b-d) Category 1-3 BLSN cases. Blue (red) bars represent the percent of wind (BLSN) observations in each 10° wind direction bin.	132
56. Two-dimensional histograms of probabilistic BLSN depth vs. meteorological variables from the MET instrumentation.	133

LIST OF TABLES

Table	Page
1. Periods of missing data for the ceilometer during 2016 determined through manual inspection and ARM data quality reports. The likelihood of BLSN during each period is based on human reporting of BLSN and other available observations.	37
2. As in Table 1 but for the HSRL.	42
3. As in Table 1, but for the MPL.	44
4. As in Table 1, but for the KAZR.	47
5. Summary of properties of the remote sensing instrumentation discussed in Sections 2.2.3-2.2.7.	48
6. 2x2 Contingency table for comparisons between human observations and algorithm results. BLSN refers to periods in which BLSN was detected, and non-BLSN means it was not observed. Human and algorithm refer to the human observations and algorithm results, respectively.	62
7. Altitude and clear sky threshold backscatter coefficient for the lowest usable bin for the 30 m and five-minute averaged ceilometer, MPL, and HSRL observations.	64
8. Criteria for validity of each algorithm.	68
9. Seasonal and total BLSN hours and frequencies for each algorithm shown in Figure 33. The five-minute algorithm is further broken down into BLSN categories.	103
10. Impacts of clear-sky backscatter coefficient percentile on algorithm characteristics. The 95 th percentile (used in the five-minute algorithm) results are included for comparison.	106
11. As in Table 10, but for the wind speed threshold.	107
12. As in Table 10, but for the visibility threshold.	108

13. Annual and seasonal hours of BLSN for each algorithm during BLSN times detected by the five-minute algorithm. Percentages given are the proportion of five-minute algorithm detections that met said criteria.	113
14. Number of analyzed hours and detected BLSN depth for the probabilistic and 5-min BLSN algorithms for BLSN case days.	119
15. List of sensitivity tests applied to the probabilistic algorithm.	121
16. Instruments deployed to McMurdo Station (adapted from Lubin et al. 2015).	139

ACKNOWLEDGMENTS

I would like to thank my thesis advisor, Aaron Kennedy, for great support and guidance throughout the project. When Dr. Kennedy asked me to join this project, I thought I'd give it a shot, and it opened my eyes to my love of polar weather and climate issues. I now plan to pursue these topics as I move forward in my career, so I am very thankful to be a part of this project. I would also like to thank my committee members, David Delene and Michael Poellot for their helpful comments and edits throughout the thesis process.

Additionally, I thank Michael Ritsche and his colleagues at ARM for reprocessing the ceilometer data, Israel Silber for providing MPL calibration constants and guidance, as well as Alexandra Gossart for assistance with the ceilometer BLSN detection algorithm, and the Lidar group at the University of Wisconsin-Madison for providing the high-resolution HSRL data. I also would like to thank the Antarctic Meteorological Research Center (AMRC) and the McMurdo Station Meteorology Office for the human observation data and Mark Seefeldt for sharing Parsivel² data from the Phoenix site. In addition, thank you to the DOE ASR program for funding the presented research.

Lastly, I would like to recognize my family and friends who have supported me throughout this process. Firstly, to Greg, thank you for encouraging me and keeping me positive throughout all of the craziness that has occurred in 2020. I'd also like to thank the wonderful community of graduate students at UND that were along for the ride with me. I would not have been able to complete this project without the support of my loved ones, and for that I am very grateful.

ABSTRACT

Blowing snow is an impactful process in cold climates that affects regional thermodynamics, radiation properties, and the surface mass balance of snow. Though it has significant climatic impacts, the process is still poorly understood and not widely included in weather and climate models. In 2016, the AWARE Field Campaign saw the deployment of a large suite of in situ and remote sensing instruments to McMurdo Station, Antarctica allowing for investigation of blowing snow. A ceilometer-based blowing snow detection algorithm used elsewhere in Antarctica is applied to data from AWARE, yielding a blowing snow frequency of 14.1% compared to 8.2% as detected by human observers. To increase confidence in detections, the algorithm is updated to have shorter temporal averaging and to include a variety of meteorological thresholds to limit false detections due to fog. The revised algorithm detected a blowing snow frequency of 7.8%, which is in closer agreement with human observations. A multi-instrument probabilistic depth algorithm is developed to increase confidence in the depth estimations given for detected blowing snow. This algorithm is applied to 41 blowing snow case days and found an average depth of 218.3 m and a mean absolute difference of 97.6 m when compared to the results of the ceilometer-based algorithm. The largest differences between the two algorithms were found during intense events occurring with precipitation. The results of this study help to aid the modelling community in reproducing the process and its impact on the regional climate.

CHAPTER 1

BACKGROUND & INTRODUCTION

The movement of surface snow by wind is a common phenomenon in high latitude regions, and is often referred to as snow transport (Li and Pomeroy 1997a). The redistribution of surface snow is typically broken down into two processes: blowing and drifting snow. The distinction between these two types of snow transport is the height at which the process occurs. Mahesh et al. (2003) defines blowing snow (BLSN) as “masses of snow particles carried by the wind to fill the near-surface atmospheric layer and to limit the horizontal visibility”. The Atmospheric Environment Service (part of Environment and Climate Change Canada) states that BLSN can obscure visibility from the surface up to 9.7 km altitude (Li and Pomeroy 1997a). Drifting snow only includes cases of BLSN where the transportation layer is less than 2 m in depth (Li and Pomeroy 1997a; Leonard et al. 2012; Gossart et al. 2017). These definitions are consistent with those given by the American Meteorological Society Glossary of Meteorology, although the National Weather Service (NWS) often states "eye-level" vs. providing an exact height as the distinction between the two processes (NOAA 1998).

1.1. Impacts of Blowing Snow

BLSN has economic impacts in cold regions since the low visibilities can cause dangerous transportation conditions (Rooney 1967; Changnon and Changnon 1978; Hershey and Osborne 2008) and extended power and communications outages (Burrows et al. 1979). In regions where these conditions are common, structures must be designed such that they can handle the weight of the drifts that build as a product of the transportation

of snow (DeGaetano et al. 1997). The redistribution of moisture can have implications on available moisture for agriculture (Hershey and Osborne 2008). Major events can also lead to widespread loss of livestock and wildlife (Graff and Strub 1975).

Additionally, the transportation of snow has significant impacts on the energy budgets of cold climate regions. BLSN plumes can alter the surface radiation budget, commonly increasing the surface albedo of the region and reducing the surface temperature (Bintanja 2001; Yang and Yau 2011; Leonard et al. 2012). This cooling increases the stability of the surface inversion layer (Bintanja 2001; Yang and Yau 2011). This effect depends on the surface in which the snow is blowing over. For example, if BLSN is occurring over a city with dark cement surfaces, it increases the albedo more than a case over a snow-covered field or ice surface. The depth of the BLSN plume affects the behavior of longwave radiation, altering the depth of the surface inversion (Mahesh et al. 2003). Particles in the air increase friction and resistance, having a strong impact on vertical wind speed gradients (Bintanja 2001).

BLSN has a thermodynamic impact that is associated with the process of sublimation. As particles are lifted, a higher proportion of each particle's surface area is exposed to the air, increasing the rate at which particles may sublimate if the relative humidity (RH) is less than 100% (Déry and Yau 2002; Palm et al. 2017). As BLSN is initiated, sublimation increases due to the increased ventilation of particles. The presence of particles in the air causes increased turbulence, which mixes warmer air above the inversion down towards the surface, increasing the temperature and making the layer nearly isothermal. The mixing of warmer, drier air into the layer prevents the BLSN layer from becoming fully saturated. The humidity of the layer tends to decrease with height, as entrainment plays a bigger role

towards the top of the plume. The extent of sublimation varies depending on the size and quantity of particles suspended in the air, as well as the temperature and humidity of the layer (Palm et al. 2017). Smaller particles, which are more likely further aloft (see Section 1.2.2. Microphysical Properties of), sublimate faster than the larger particles found near the surface due to drier air and their higher surface area to mass ratio (Pomeroy and Male 1988). Sublimation may increase by up to 80% due to entrainment or advection of dry air into a BLSN plume (Bintanja 2001). Because sublimation is a cooling process, it can cause a dynamic response if it is widespread. A modelling study by Yang and Yau (2011) found that BLSN can cause cyclolysis and anticyclogenesis due to these effects, leading to changes in the evolution of synoptic scale systems (Yang and Yau 2011) and low-level flow (Bintanja 2001). Additionally, BLSN particles act to increase the absorption of longwave radiation while reflecting incoming shortwave energy (Yang et al. 2014; Palm et al. 2018b).

Palm et al. (2018b) provided a summary of the net effect of BLSN plumes on the thermodynamic structure and radiative balance of the lower atmosphere (summarized in Figure 1). The described processes act to alter the temperature and moisture content of the layer. Generally, prior to BLSN initiation, a strong inversion layer exists above the surface. As BLSN occurs, the temperature of the layer increases and becomes nearly isothermal due to mechanical mixing of air into the layer from above the inversion and absorption of longwave radiation. The strength of the warming is related to the depth of the layer, with deeper layers seeing stronger surface warming. RH increases as sublimation occurs, but typically does not reach saturation due to the drier air being mixed in from above the inversion.

BLSN modifies the properties of the surface snow pack by transportation and sublimation (Budd 1966; Bintanja and Reijmer 2001; Déry and Yau 2002; Lenaerts et al. 2010). These processes can significantly impact the surface mass balance in regions where BLSN is common, such as Antarctica and the Northern Canada. For example, BLSN transportation and sublimation combined has been estimated to remove over 50% of fallen snow in coastal regions of Antarctica (Scarchilli et al. 2010). Palm et al. (2017) calculated that the Antarctic continent loses an average of 393.4 ± 197 Gt of snow annually to BLSN sublimation. This estimate is based upon satellite observations and atmospheric reanalysis data, and can be used as a rough approximation of the impact of the process. Further observations are required to validate and reduce the uncertainty of these numbers.

1.2. Properties of Blowing Snow

1.2.1. Physical Process of Blowing Snow

For BLSN to occur, the wind must be strong enough to dislodge particles from the surface snowpack (Figure 2). The wind speed at which this occurs, known as the threshold wind speed, varies depending on the properties of the surface snow. This is because the cohesive forces between individual particles must be overcome by the shear force exerted by the wind (Kind 1981; Li and Pomeroy 1997a; Leonard et al. 2012). A simple relationship exists between particle size and the wind speed needed to begin movement (Kind 1981; Leonard et al. 2012). The surface of the snowpack is typically made up of many particles of different sizes, complicating said relationship. Small particles tend to be shielded from the wind by larger particles, increasing the necessary wind speed to begin drift (Schmidt 1982; Leonard et al. 2012). The cohesion between particles also becomes more important than particle size alone in surfaces with variable particle sizes (Schmidt 1982).

Li and Pomeroy (1997a) investigated the factors affecting threshold wind speeds for BLSN. Snow elasticity and kinetic friction both increase with decreasing temperatures, requiring higher wind speeds to dislodge particles. Warm snow surface temperatures see high threshold wind speeds due to liquid water cohesion. For dry snow that has not reached temperatures above 0°C, the wind threshold is lowest around -25°C, increasing at both warmer and colder temperatures, based on surface observations from Canadian weather stations. Wet snow shows higher threshold wind speeds in all cases, with a steep increase as temperatures warm to approximately 0°C. There is significant variability in threshold wind speed at a given temperature due to factors including snow particle properties and the approximations made to estimate snow surface temperature.

Once transport is initiated, larger particles bounce along the surface as they move with the wind while smaller particles may be suspended in the air (Li and Pomeroy 1997a; Nishimura and Nemoto 2005). A particle is only lifted from the surface if the vertical component of the wind speed is at least the same magnitude as the particle's fall velocity (Kind 1981). Saltation is the primary mode of transport in the lowest few centimeters above the surface, while particles above are supported by the vertical component of the wind (Kind 1981; Pomeroy and Male 1988). Saltating snow loses much of its kinetic energy during its collisions with the surface (Kind 1981), but the collision displaces surface particles, reducing the wind speed required to move additional snow from the surface (Li and Pomeroy 1997a; Leonard et al. 2012). By the definitions made earlier, BLSN cases herein include both processes as observations are made above the saltation layer (Leonard et al. 2012). These transport mechanisms can be seen in Figure 2. As the particles begin to move, the suspended particles increase friction and act to reduce wind speed in the column.

1.2.2. Microphysical Properties of Blowing Snow

A gamma distribution has been shown to fit near-surface (0-10 m) BLSN particle size distributions in both the Arctic and Antarctic (Budd 1966; Schmidt 1982; Nishimura and Nemoto 2005). The average particle size decreases quickly with height after the first 2 m (Budd 1966) and varies depending on the extent of turbulence in the layer (Pomeroy and Male 1988). Nishimura and Nemoto (2005) used in-situ measurements recorded over October and November 2000 in western Antarctica to study particle size distribution and mass flux during BLSN events. Four snow particle counters, three ultrasonic anemometers, thermometers, and humidity sensors were mounted on a 30 m tower. Particle size distributions were measured at a variety of heights and the distributions agreed with previous studies such as Li and Pomeroy (1997a); the distribution of particle sizes was wider at low elevations, trending towards smaller particles with height. It was also observed that the particle size distribution is much wider and has a bi-modal distribution at higher elevations if BLSN is concurrent with precipitation.

BLSN particles tend to be irregularly-shaped and non-uniform (Budd 1966). An image showing fragmented BLSN particles is shown in Figure 3. This early study hypothesized that many of the discrepancies between the predictions of existing snow drift theory and measurements can be explained by the varying particle sizes and distribution of fall velocities. Particles are broken from the surface snow pack and continue to shatter as they bounce along the surface (Pomeroy and Male 1988). Suspended particles tend to be rounded and smooth due to sublimation on particle edges (Pomeroy and Male 1988).

Pomeroy and Male (1988) modelled a BLSN plume to investigate the optical characteristics of BLSN, which are closely tied to the shape of the particles. When looking

at individual particles, large variations in extinction were observed for particles of approximately the same size. The optical properties are further complicated by considering the irregular nature of the particles, with many particles generating wave-like signals. These wave-like effects were shown to average out to approximately the interference expected from an ice sphere when looking at ensembles of particles together. Observation of microphysical properties of BLSN show amorphous BLSN particles can be approximated as ice spheres, assuming small cross-sectional area, with relatively low error. The small size and spheroidal shape of BLSN particles influence remote sensing observations of the process

1.3. Remote-Sensing Observations of Blowing Snow

A variety of remote-sensing projects have been performed to better observe and understand BLSN. These include ground-based studies with lidar and radar, and satellite-based studies. Limitations exist for both types of work. Ground-based studies have no obstruction due to cloud cover, but BLSN can occur below the minimum detection height of some platforms. Meanwhile, satellite studies have used space-borne lidar that is unable to penetrate optically thick clouds. Gossart et al. (2020) estimated that 90% of BLSN in coastal Antarctica occurs during cloudy conditions, and is likely missed by space-borne lidar. In summary, satellite studies are optimal for getting a broader spatial understanding of the process, as measurements are made over broad geographic areas, rather than point measurements where ground-based instruments are deployed. In the following sections, some notable ground- and satellite-based remote sensing BLSN studies are discussed.

1.3.1. Ground-Based Remote-Sensing of Blowing Snow

Mahesh et al. (2003) investigated BLSN with a micropulse lidar (MPL) at the South Pole Station between 1999 and 2002. BLSN occurred on forty days during the study period. The top of the BLSN layer was determined by identifying a surface-based peak in backscatter coefficient that is above the background molecular backscatter signal. The mean layer thickness for the 40 cases was 416 m, although half of the plumes had depths < 200 m. BLSN was usually limited to the surface inversion layer and below. No relationship was found between wind speed and depth of BLSN layer. It was hypothesized this was because particles remained suspended in the air after being lofted, allowing for weaker wind speeds during portions of the event.

A climatology of high Arctic winter tropospheric particles was produced by investigating observations from a high spectral resolution lidar (HSRL) and millimeter-wave cloud radar (MMCR) deployed at the Zero-altitude PEARL Auxiliary Laboratory in Eureka, Nunavut from 2005 to 2008 (Bourdages et al. 2009). Layers were analyzed by looking at the color ratio, the backscatter coefficient, and linear depolarization ratio. This study did not explicitly investigate BLSN but observed boundary-layer ice crystals in 1338 h of observations. These layers were constrained to the lowest 750 m of the atmosphere. The depolarization found in these layers was inconsistent between cases, with a wide variety of values being observed. Analysis of the color ratio showed that low-level ice crystals were likely contaminating the retrievals of aerosol properties at this location. The results presented in this study help to more accurately classify remotely-sensed observations of different types of tropospheric particles in high latitude regions.

Building on previous lidar-based studies, Gossart et al. (2017) developed an algorithm to detect BLSN based on backscatter profiles from a ground-based ceilometer. This algorithm used vertical backscatter profiles, as in Mahesh et al. (2003), and is discussed in detail in Chapter 3. Ceilometer data were analyzed at Neumayer III and Princess Elisabeth stations in western Antarctica from 2010 to 2016. The algorithm agreed with human observations of BLSN 78% of the time. At these locations, availability of fresh snow was as important as wind speed, as 92% of BLSN observed occurred during or shortly after a synoptic-scale precipitation event.

1.3.2. Satellite-Based Remote-Sensing of Blowing Snow

Several studies have used satellite-borne observations to study BLSN in remote regions. Active and passive remote sensing were used in concert by Palm et al. (2011) to investigate BLSN frequency over Antarctica. An algorithm was developed using ICESat (75 m resolution) and the Cloud-Aerosol Lidar with Orthogonal Polarization (CALIOP) onboard the Cloud Aerosol Lidar and Infrared Pathfinder Satellite Observations (CALIPSO). BLSN was detected with backscatter cross-section profiles (like ground-based studies), a digital elevation model, and 10 m wind speed from the Goddard Earth Observing System 5 (GEOS-5). The elevation model was used to remove the signal due to the ground itself, and measurements were checked to determine if the backscatter coefficient was above $2.5 \times 10^{-2} \text{ km}^{-1} \text{ sr}^{-1}$ and the wind speed was above 4 ms^{-1} . This algorithm was applied over Antarctica from 2007 to 2009, and spatial and temporal patterns as well as characteristics of BLSN plumes were investigated. It was found that regional frequencies did not shift significantly from year to year, though East Antarctica had higher interannual variability. The average depth of the BLSN layers investigated was 120 m, with

an average optical depth of 0.2.

Later, Palm et al. (2017) measured BLSN over Antarctica using CALIOP along with Modern-Era Retrospective analysis for Research and Applications, Version 2 (MERRA-2) reanalysis data (Gelaro et al. 2017) to quantify the extent of surface snow transport and sublimation from BLSN for the period of 2007-2015. To reduce false detection of BLSN, the layer mean depolarization and color ratio were assessed, and the analysis layer was limited to the lowest 500 m AGL. MERRA-2 provided the necessary temperature, humidity, and wind speeds at the location and times of BLSN profiles to estimate sublimation and snow transport. It was found that the spatial patterns of transport agreed with recent modelling studies (ex. Déry and Yau 2002), but the extent of the sublimation observed was larger than expected. Maximum sublimation values of 250 ± 125 mm snow water equivalent annually were found within 200 km of the coast, where relatively warmer air is found, increasing local sublimation. Interannual variability was found to be 10-15%, and was largely attributed to precipitation and temperature differences.

1.4. Blowing Snow in Antarctica

1.4.1. Importance of Blowing Snow in the Antarctic Climate

Recent studies have identified that Western Antarctica is one of the most rapidly warming regions on Earth; Bromwich et al. (2013) found the warming trend to be $2.2 \pm 1.2^\circ\text{C}$ per decade between 1958 and 2010. This dramatic warming has implications for the surface mass balance of the Antarctic Ice Sheet. The surface mass balance represents the balance of inputs and outputs to the system, which is given by:

$$S = \int (P - E - M - Q_t - Q_s) dt \quad (1)$$

where S represents the surface mass balance, P is precipitation, E denotes surface evaporation and sublimation, M represents surface melt and runoff, and Q_t and Q_s represent BLSN transport and sublimation, respectively (Palm et al. 2017). As the climate warms, the melting of the ice sheet has been shown to be a large contributor to sea level rise (Giovinetto et al. 1992; Gallée et al. 2001). Modelling the ice sheet's surface mass balance accurately is pivotal to understanding the contributions it will make to the changing climate. Surface processes, such as BLSN, play a role in redistribution and sublimation of surface mass alter the surface mass balance, particularly at regional and local scales. Better understanding BLSN in Antarctica may help to better model the region's surface mass balance.

The frequency of BLSN varies across Antarctica due to topography and climate dynamics of the region. Although much of the continent is very remote, estimations of the frequency of BLSN have been made for several regions. Human-observations indicate that BLSN occurs 33.8% of the time at the South Pole Station, with annual frequencies ranging from 22.1% to 53.3% (Mahesh et al. 2003). Palm et al. (2017) estimated that winter BLSN frequency along the Antarctic coast is approximately 15-20% while megadune regions of the ice sheet can see BLSN frequencies reaching up to 75% (Figure 4a). Moisture is more bountiful in coastal regions allowing for higher amounts of precipitation compared to the inland portions of the continent. Many BLSN events occur within 24-48 hours of a precipitation event (Gossart et al. 2017) meaning that the coastal regions may see frequent BLSN.

Previous studies have suggested that sublimation occurring with BLSN removes substantial amounts of snow from the Antarctic continent (Giovinetto et al. 1992; Gallée et

al. 2001; Déry and Yau 2002). Giovinetto et al. (1992) estimated that BLSN and drifting snow move approximately 1.2×10^{14} kg year⁻¹ at 70°S. It is believed mass transport is much higher over the central regions of the ice sheet but this is more difficult to assess due to the lack of observations (Giovinetto et al. 1992). Déry and Yau (2002) estimated the average annual BLSN sublimation rate over the Antarctic Ice Sheet using ERA15 reanalysis data and found it to be in excess of 50 mm snow water equivalent per year along the fringes of the ice sheet (shown in Figure 4b).

Antarctica often sees strong katabatic winds flowing towards the ocean. Katabatic winds are gravity-driven flows due to air temperature/density differences (Kodama et al. 1985). As sublimation occurs with BLSN, cooling causes air density to increase, therefore accelerating the katabatic flow by up to 30% (Kodama et al. 1985). Zhdanov (1977) made observations of BLSN plumes associated with the katabatic winds based on satellite observations. More recently, Scarchilli et al. (2010) observed the same phenomenon using visible imagery from NASA's Terra and Aqua satellites. The shadows cast by these plumes suggested depths greater than 100 m, altering the outgoing longwave radiation in the region (Yang et al. 2014).

1.4.2. 2016 AWARE Field Campaign

The U.S. Department of Energy (DOE) Atmospheric Radiation Measurement (ARM) West Antarctic Radiation Experiment (AWARE) Field Campaign took place in 2016 to investigate cryospheric loss in the West Antarctic Ice Sheet (WAIS). McMurdo Station on Ross Island (77°51'S, 166°40'E) was the central facility for the project, with an additional mobile facility deployed at the WAIS (79°28'S, 112°5'W) during the summer (Lubin et al. 2020). The locations of the sites are shown in Figure 5. The full ARM Mobile Facility

(AMF2) was deployed to McMurdo Station for all of 2016. A full list of instruments in the AMF2 are listed in Appendix A.

The primary goal of the AWARE Campaign was to investigate the surface energy budget and thermodynamic structure of the atmosphere in Western Antarctica (Lubin et al. 2015). At McMurdo Station, priority was placed on studying the importance of mixed-phased clouds and aerosols with respect to the radiation budget and understanding cloud microphysical properties (Lubin et al. 2015). While understanding BLSN in the region was not explicitly a goal of the campaign, the campaign provides a unique opportunity to study the process with a wide variety of instruments deployed for a full year, supplying continuous, quality-controlled data.

1.5. Objectives

Although the effects of BLSN are vital to understanding the climate of high-latitude regions, this phenomenon is still poorly understood and not widely included in weather and climate models (Gallée et al. 2001). While BLSN models exist to simulate plumes and regional surface mass balance, there are several issues that limit their accuracy. A primary issue limiting the accuracy of these models, and the ability to correctly parameterize the process in weather and climate models, is a lack of observations and understanding of the process itself. The varying parameterizations bring difficulty to modelling the surface mass balance of ice sheets in the polar regions (Leonard et al. 2012). Better understanding of the process will allow for the improvements of model parameterizations and estimates of snow transport and sublimation.

The occurrence of BLSN in Western Antarctica is analyzed by applying the ceilometer-based detection algorithm derived in Gossart et al. (2017) to the observations

from McMurdo Station during AWARE. The algorithm has been shown to perform well in Eastern Antarctica, but it is hypothesized that it produces a positive bias over the true frequency of BLSN because of the lack of meteorological thresholds and lengthy temporal averaging applied to ceilometer backscatter observations. Additionally, the estimation of BLSN depth during complex events was noted to be questionable based on limitations of the ceilometer.

The objective of this study is to implement improvements to the Gossart et al. (2017) BLSN detection algorithm to increase confidence in its detections and to provide a more robust estimation of plume depth during events occurring with precipitation. In situ observations from the AMF2 of basic meteorological properties are incorporated into the algorithm to provide confirmation that BLSN may truly be occurring and the temporal averaging is reduced to lessen the positive bias in BLSN frequencies. The frequency of BLSN is compared to human observations to grossly assess validity of detections, as human observations are subjective and cannot be considered ground truth. Given the limitations of the ceilometer profile analysis in complex scenes, such as precipitation mixed with BLSN, alterations are made to the algorithm by supplementing it with a variety of remote sensing observations available during AWARE. These additional observations improve the ability for the algorithm to detect the top of the BLSN layer, particularly during precipitation events. The updated algorithms will help to gain an in-depth understanding of the frequency and characteristics of BLSN during the AWARE Field Campaign.

In summary, the performed analysis will provide the most comprehensive remotely-sensed study of BLSN to date at any location in the world. In turn, it will better characterize the plume height during complex events which will aid in understanding the amount of

surface snow being removed. Further, more robust estimations of BLSN occurrence and depth are an excellent resource for model validation and these properties will be distributed to the ARM user community to aid other researchers.

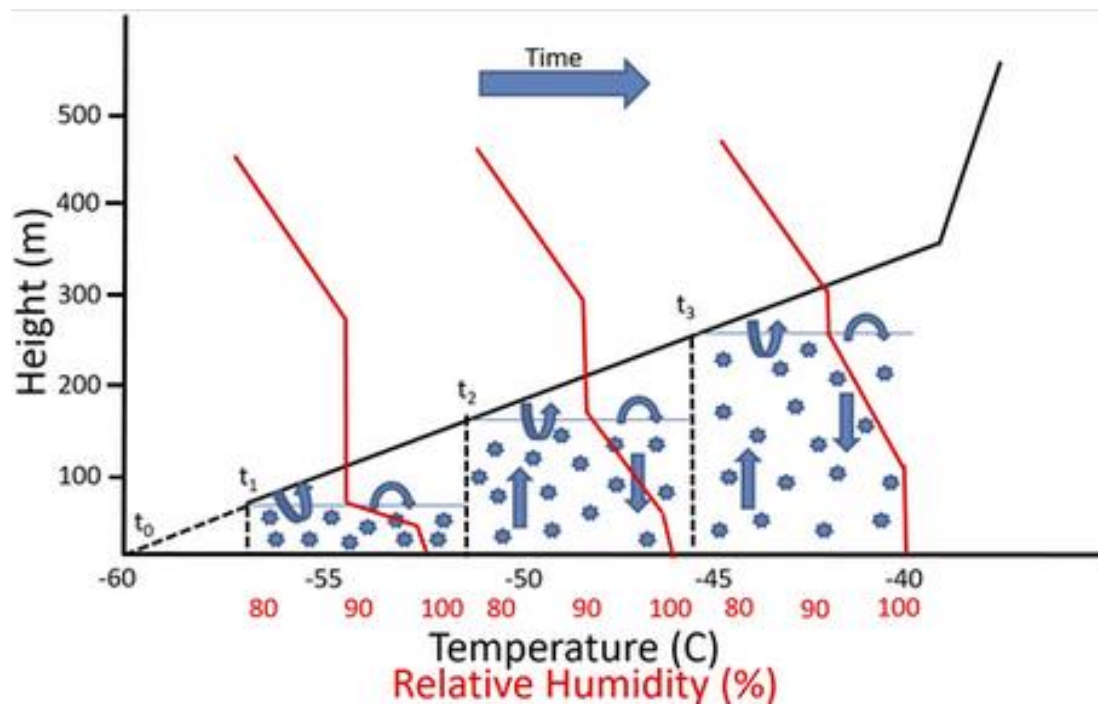


Figure 1. Temporal evolution of temperature (black) and moisture (red) structure during a BLSN event. Figure adapted from Palm et al. 2018.

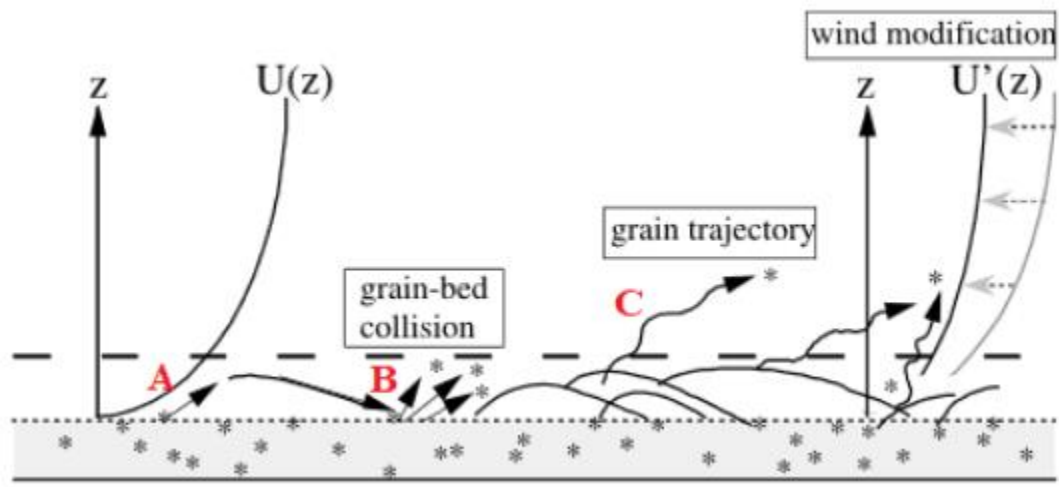


Figure 2. Graphic depiction of the movement of particles in BLSN and its effect on the vertical wind profile (adapted from Nishimura and Nemoto 2005). The dotted line represents the top of the snowpack, and the dashed line represents the top of the saltation layer. Z represents altitude, $U(z)$ represents the initial vertical wind speed profile, and $U'(z)$ represents the vertical wind speed profile altered due to BLSN. Transport is initiated by the wind at A. Collisions with the snowpack occur at B, dislodging more particles to be transported. Particles begin to be carried in suspension by the wind at C.



Figure 3. Image from Dr. Aaron Kennedy's snowflake camera in Grand Forks, North Dakota at 07:31:13 UTC on 12 February 2020 showing several broken snow crystals (appearing as brighter particles) surrounded by other fragmented (darker) BLSN particles.

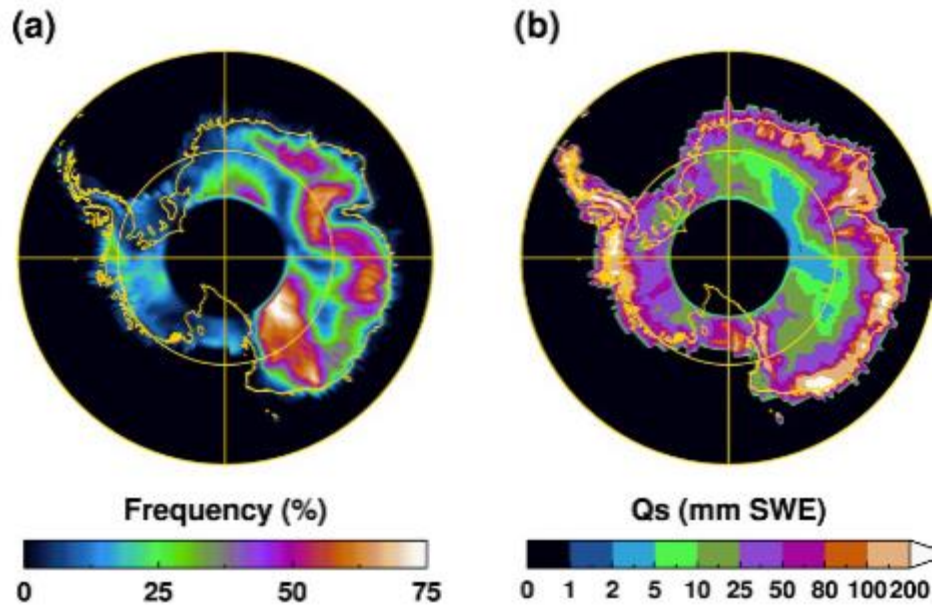


Figure 4. Average winter (April - October) (a) BLSN frequency and (b) average annual sublimation from 2007-2015 based on CALIPSO and MERRA-2 data (Palm et al. 2017).



Figure 5. Map showing the location of McMurdo Station and the Western Antarctic Ice Sheet field site

CHAPTER 2

DATA SOURCES

2.1. Human Observations

Surface weather conditions are recorded by human observers at McMurdo Station for every three-hour period. These observations are available from 1999 to present from the Antarctic Meteorological Research Center (AMRC) at the University of Wisconsin-Madison. For the purposes of this study, only complete years of records (2002-2018) were analyzed. Freezing precipitation (snow, snow grains, or ice crystals), fog/mist, and BLSN conditions are recorded as the length of time for each three-hour period that said condition occurred. The daily observer spreadsheets from McMurdo Station were accessed from the AMRC repository (<ftp://amrc.ssec.wisc.edu/archive/>). Figure 6 shows an example of a daily observation worksheet. The date, hours, and timing of each weather condition from each daily worksheet were aggregated into csv files to compare with algorithm results.

Several potential issues need to be considered when comparisons are made to instrumentation at the AMF2. First, the observation sites are not collocated. The human observations are made in McMurdo Station (10 m elevation) while the AMF2 is located near the observation hill southeast of town (78 m elevation). The complex terrain of Ross Island suggests that location alone could cause some differences in the two datasets. Human observations also have a degree of subjectivity; observations may be inconsistent between different observers and human error is possible even from the standpoint of simple data entry (Hanesiak and Wang 2005; Elevant 2010). Additionally, it is dark in Antarctica for approximately half of the year, making it more difficult to observe surface weather

conditions as noted in other high latitude studies (Hanesiak and Wang 2005). Collectively, it is probable that the human observed frequency of BLSN at McMurdo Station is biased compared to observations at the AMF2. Shorter BLSN events could easily be missed by human observers, leading to reduced frequencies being reported. On the other hand, it is also possible that estimations of the length of events may be longer or shorter than the actual period of BLSN, and periods of cyclic BLSN may be overestimated.

2.2. AMF2 Instrumentation

Deployment of the AMF2 at McMurdo Station started in November 2015, but the data were of variable quality until 1 January 2016. For this reason, this study analyzes data from 1 January 2016 to 1 January 2017. All AMF2 observations are subject to ARM's stringent data quality protocol, including automated quality control checks and data quality reports that notify the user of periods of missing or suspect data. Examples of data from 12 June 2016, a day with falling snow and BLSN at McMurdo Station, are used for all instruments described in this section.

2.2.1. Meteorological Instrumentation at the AMF2

The surface meteorological station equipment (MET) deployed with the AMF2 in McMurdo Station and WAIS is composed of a variety of in situ sensors to measure basic meteorological properties (Ritsche and Prell 2011). An image of the MET at the DOE ARM Southern Great Plains site is shown in Figure 7. The measurements encompassed by MET include barometric pressure, temperature, RH, wind speed, and wind direction (Ritsche and Prell 2011). All sensors were supplied by Vaisala, including a barometer, present weather detector, and ultrasonic wind detectors installed at 1 m, 2 m, and 10 m AGL, respectively

(Ritsche and Prell 2011). An example of output from the MET instrumentation is shown in Figure 8.

The Vaisala HMP155 measures air temperature using platinum resistance sensors, and RH with respect to liquid water directly based on voltage measurements using capacitance measurements from a water vapor absorbing thin polymer film (Ritsche and Prell 2011). Although this study focuses on solid hydrometeors, supercooled liquid was shown to be present in the lower atmosphere during the AWARE Field Campaign (Silber et al. 2018a), so use of RH with respect to water is deemed appropriate to distinguish fog from BLSN. To confirm this, RH with respect to ice was calculated using vapor pressure measurements from the HMP155, and only small differences (0-5%) between the value provided and calculated RH were found. The uncertainty associated with the RH measurements is $\pm(1.0 + 0.008 \times \textit{reading})\%$; for example, if the measured RH is 85%, the associated uncertainty would be $\pm 1.68\%$ (Vaisala Oyj 2020). The uncertainty associated with temperature measurements is $\pm(0.226 - 0.0028 \times |\textit{temperature}|)\text{°C}$ (Vaisala Oyj 2020). This means that for a measured temperature of -30°C , the uncertainty is $\pm 0.142\text{°C}$.

The Vaisala Ultrasonic WS425 sensor is composed of an array of three ultrasonic transducers on a horizontal plane and measures the transit time between transducers to measure the wind vector and derive the horizontal wind speed and direction (Vaisala Oyj 2010). Invalid measurements can occur when raindrops or ice pellets hit the sensor, but are removed using a signal processing technique (Vaisala Oyj 2010). Wind speed measurements are subject to an uncertainty of $\pm 0.135 \text{ m s}^{-1}$ or 3% of the measurement (whichever is greater), while wind direction accuracy is within 2° (Vaisala Oyj 2010).

The final measurement from the instrumentation suite that is used in this study is visibility from the Vaisala PWD22 sensor. The PWD22 uses a forward scattering visibility meter, measuring the amount of incident light that is scattered in the forward direction by particles between the transmitter and receiver, yielding measurements with an accuracy of $\pm 10\%$ (Vaisala Oyj 2004). The connection of the sensors to data loggers used single-ended 0 to 1 V measurement, rather than a four-wire bridge. Data are available from the meteorological sensors from 17 November 2015 to 1 January 2017 with no downtime noted by ARM, though manual inspection saw short periods in which a single sensor may have failed.

2.2.2. Parsivel² Optical Disdrometer

The OTT Particle Size and Velocity disdrometer (Parsivel²) is an optical disdrometer allowing for the measurement of different forms of precipitation (OTT HydroMet 2016). An image of the Parsivel² is shown in Figure 9. The instrument uses a 650 nm laser to produce a horizontal sheet of light with a surface area of 27 mm by 180 mm onto a single photodiode, recording the shadow of particles that pass through by the reduction in voltage measured. This allows for direct measurement of particle size and fall speed. The following variables can then be derived: particle size spectrum, type and intensity of precipitation, kinetic energy, radar reflectivity, and horizontal visibility. Particles up to 25 mm in diameter can be measured by the instrument, sorted into 32 size classes of varying widths. The two size bins of smallest diameter (< 0.25 mm) are typically not used due to low signal-to-noise ratio (Battaglia et al. 2010). Particle fall speeds are also sorted into 32 classes, with 0.2 and 25 m s^{-1} being the minimum and maximum detectable fall speeds, respectively (OTT HydroMet 2016). An example of output from the Parisvel² at McMurdo Station is

shown in Figure 10. The Parsivel² was deployed from 19 November 2015 to 1 January 2017. The only period of missing data noted during the official campaign dates was from 31 January to 4 February 2016. Manual inspection showed that data were also missing on 22 October and 30 December 2016. Based on assessment of other observations, it is unlikely that BLSN occurred during these periods.

The Parsivel² was designed for measurement of liquid precipitation; therefore, limitations exist to its use when studying snow. The diameters measured by the instrument are given as the diameter of a sphere with equivalent volume for a raindrop (Battaglia et al. 2010). Battaglia et al. (2010) investigated the errors introduced by this assumption when using the Parsivel to observe snow particles. With regards to particle diameter, the highest uncertainty in measured particle diameter is found with the smallest particle sizes, as shape and orientation are more unclear. Fall velocities are found to be underestimated for particles with a widest horizontal dimension of less than 10 mm and overestimated for larger particles (by 30-40%). Maahn (2010) found a positive bias in precipitation rate during BLSN events in measurements from northern Norway. Friedrich et al. (2013) also identified an artifact in Parsivel² measurements in observations from six separate instruments deployed into hurricanes. Unrealistically large particle number concentrations were observed for large particles (> 5 mm diameter) at high wind speeds (beginning around 10 ms⁻¹). It was hypothesized that this effect was caused by particles moving through the instrument's field of view at an angle. These effects need to be considered when investigating Parsivel² observations during BLSN events.

2.2.3. Vaisala CL31 Ceilometer

The Vaisala CL31 ceilometer is a lidar system that transmits at a single-wavelength (910 nm at 25°C), measuring the backscatter coefficient with an avalanche photodiode receiver (Morris 2016). An image of a vertically pointing CL31 is shown in Figure 11. The CL31 yields data with 16 s temporal resolution and 10 m vertical resolution up to approximately 7.5 km above the instrument. Accuracy is considered within $\pm 1\%$ for backscatter coefficient and ± 5 m for retrieved height (Morris 2016). An example of backscatter coefficient from the ceilometer is shown in Figure 12. The ceilometer began collecting data on 30 November 2015 and was removed on 2 January 2017. Periods of missing data from the ceilometer are noted in Table 1.

The ceilometer uses overlapping transmitting and receiving optics such that beam overlap occurs closer to the instrument than many other remote sensing instruments, producing data only 10 m above instrument level (Morris 2016). The instrument includes a built-in filter to correct unrealistically high backscatter coefficient values in the first range bin due to window obstruction (Gossart et al. 2017). This filter introduces artifacts into the data in the first range bin, resulting in values that are consistently higher than that in the following bins. For this reason, the first range bin is not used in the BLSN detection algorithm. The ceilometer also uses relatively low energy (310 W), allowing for more economical operation (Morris 2016). Since the energy of the emitted pulses is quite low, many pulses are averaged to reduce random background noise (Morris 2016). The low emitted energy can introduce attenuation issues, particularly in mixed events where snow is both falling and blowing due to many particles being present in the sample volume. While this is not expected to affect the retrieval of BLSN plume heights for cases under clear sky,

it may cause issues in determining the depth of layers with more complicated hydrometeor profiles.

2.2.4. High Spectral Resolution Lidar

The high spectral resolution lidar (HSRL) is a ground-based system measuring vertical profiles of variables such as backscatter coefficient, and depolarization. An image of a HSRL is shown in Figure 13. The instrument is absolutely calibrated with respect to the molecular scattering measured at each point in the vertical profile (Goldsmith 2016). The presence of particles in air is determined by measuring the Doppler frequency shift of returned photons. For molecular scattering, the Doppler shift is broad (approximately Maxwellian), while aerosols and cloud particles largely return radiation near the frequency of the instrument's laser transmitter, allowing for the signal of particulate matter to be separated from that of molecules in random thermal motion (Eloranta 2005). The instrument has a narrow, angular field of view ($45 \mu\text{rad}$), reducing multiple scattering effects (Goldsmith 2016). Received light is separated by a spectrometer into two spectral channels; one detecting photons scattered by aerosols and the other from molecules (Shipley et al. 1983). The 532 nm laser allowing for continuous profiles from approximately 50 m to 30 km (Goldsmith 2016). The vertical resolution is 7.5 m with a typical time resolution of 0.5 s, yielding high-resolution data (Goldsmith 2016). Figure 14 shows an example of observations from the HSRL. A discontinuity in backscatter coefficient related to partial beam overlap can be seen in Figure 14a near 200 m. The HSRL was deployed at McMurdo Station from 29 November 2015 to 3 January 2017 with no reported periods of missing data reported by ARM. Several periods of missing or questionable data were found through manual inspection and are listed in Table 2.

Additionally, periods where data were missing for periods of several minutes to half of an hour were common throughout the campaign around 09 and 21 UTC.

The HSRL holds several advantages over the ceilometer when studying BLSN. Firstly, depolarization measurements can be useful in separating BLSN particles from falling snow during precipitation events, since BLSN particles are more spheroidal (Sassen 1977, 1991). Also, since the HSRL uses a more powerful laser, it likely experiences fewer issues with attenuation through BLSN layers. This would allow for the true depth of the layer to be found with higher confidence. While these advantages can help provide insight into BLSN characteristics, the instrument can only be used if the BLSN plume is deep enough that it is visible to the HSRL ($> 200\text{-}300$ m). Because of this, the HSRL is most useful during intense BLSN events and those occurring with precipitation.

2.2.5. Sky Radiometers for Downwelling Radiation

The ARM sky radiometers on stand for downwelling radiation (SKYRAD) instrumentation provide continuous observation of downwelling and upwelling longwave and shortwave irradiances (Andreas et al. 2018). The total radiative flux is divided into six components; direct normal shortwave, diffuse horizontal shortwave, global horizontal shortwave, reflected shortwave, downwelling longwave, upwelling longwave (Andreas et al. 2018). SKYRAD were deployed at McMurdo Station from 16 November 2015 to 29 December 2016, but data are only available for 1 January to 29 December 2016. Data were not available on 31 August 2016 during radiometer replacement. It is also noted that SKYRAD can experience intermittent shadowing at low sun angles, but this is not expected to impact this study, as SKYRAD was only used to determine which lidar calibration

constant was used in the calculation of attenuated backscatter coefficient for the micropulse lidar (described in the following section).

2.2.6. Micropulse Lidar

The micropulse lidar (MPL) is a ground-based lidar with a relatively low pulse energy (10 μJ) and high pulse repetition frequency (2500 Hz) (Flynn et al. 2007). Backscatter coefficient is measured up to altitudes of approximately 20 km (Muradyan and Coulter 2020). Some derived parameters include cloud/layer boundaries, cloud ice/water content, backscatter coefficient profiles and aerosol extinction (Muradyan and Coulter 2020). The vertical resolution is 15 m, and profiles are averaged over 10 s (Muradyan and Coulter 2020). The uncertainty associated with the measurements are $\pm 2\%$ for reported distances and ± 7 m for retrieved distances (Muradyan and Coulter 2020). An example of observations from the MPL at McMurdo Station can be seen in Figure 15. Data used in this study are reprocessed as described in Silber et al. (2018b), with range corrections and cloud masking. The normalized relative backscatter coefficient is provided and can be converted to attenuated backscatter coefficient by dividing the normalized relative backscatter coefficient by the MPL calibration constant. The calibration constant is a system-specific value derived for each deployment. For AWARE, a daytime and nighttime calibration constant were derived. Day and night were distinguished based on measurement of direct incoming shortwave radiation of at least 20 W m^{-2} from SKYRAD.

The solid-state laser pulses energy with a wavelength of 523 to 532 nm (Flynn et al. 2007). Before transmission, the energy passes through a polarizing beam splitter that widens the beam, followed by a depolarizer that randomly rotates the light passing through, resulting in a net polarization of approximately zero. The light transmitted back to the MPL

by atmospheric scatterers passes through the depolarizer where approximately half of the received light may be reflected towards the laser and lost (Flynn et al. 2007). The remaining light passes through and converges onto the focal point of the transceiver telescope (Flynn et al. 2007). Polarization measurements can be made for environments that are not changing quickly by alternating between measurements with the depolarizer and without, thereby measuring depolarized signal versus non-depolarized signal (Flynn et al. 2007).

Observations began on 6 December 2015 and ended on 2 January 2017 from the MPL at McMurdo Station. No periods of missing data were reported but it should be noted that the MPL deployed during AWARE experienced problems with high levels of noise, particularly during daytime, so some data may be problematic (I. Silber, personal communication, 29 July 2020). That said, this noise is more problematic at heights above the boundary layer, and thus, is less of an issue for this study. Periods of missing data based on manual inspection are noted in Table 3.

2.2.7. Ka-band ARM Zenith Radar

The Ka-band ARM zenith radar (KAZR) is a vertically-pointing Doppler cloud radar with both dual- and single-polarization versions available (Widener et al. 2012). The former was deployed on the AMF2 during AWARE. An image of the KAZR at the DOE's SGP site can be seen in Figure 16. The first three Doppler moments are measured: equivalent radar reflectivity factor, radial Doppler velocity, and spectral width yielding vertical profiles of the atmosphere (Widener et al. 2012). Usable data begins approximately 200 m above the instrument and continues up to 20 km (Widener et al. 2012). The center frequency is 35 GHz with a 8.6 mm wavelength and maximum pulse repetition frequency of 20 kHz (Widener et al. 2012). The dual-channel digital receiver has a dynamic range of greater than

80 dB (Widener et al. 2012). Uncertainty associated with reflectivity observations is ± 3 dBZ while the accuracy of the Doppler velocity is $\pm 0.1 \text{ m s}^{-1}$ (Widener et al. 2012). An example of radar reflectivity factor and Doppler velocity from the KAZR is shown in Figure 17. The KAZR was deployed from 17 November 2015 to 2 January 2017, with no noted periods of missing data. Periods of missing data are noted in Table 4.

2.2.8. Summary of Remote Sensing Instrumentation

A summary of remote sensing instrument properties can be found in Table 5. Each instrument has unique advantages and has been used in previous studies of snow and BLSN, but they have never been used together. The ceilometer produces usable data at the lowest altitude, which is useful for studying a ground-based process, but issues with attenuation are possible due to its low power. The MPL and HSRL provide polarization measurements and a more powerful laser, but the laser is not fully in focus until higher above the instrument. The HSRL begins retrieving data 50 m above the instrument, but can have laser overlap issues up to 200-300 m. Similarly, the KAZR does not retrieve usable data until a high altitude but is more powerful and can help to distinguish falling and BLSN during mixed events.

McMurdo Station Daily Observation Worksheet																				Date: 12			
Time	Winds	Dew Pt	6 hr Temp	Visibility (hrs)	WX and Duration (Note 2)	Pcpn Amt	Max Wind (Note 3)	Max Gust (Note 3)	Low-est CIG	Station Press (mb)	SLP (mb)	24-hour Pressure	Low-est CIG	Ceiling (hrs)	Alt (m)	Press (mb)	Press Tend	SLP (mb)	24-hour Pressure				
Time	Dir Spd Temp	Temp	Max Min	<1600 <4800 <9999	sn/glc hrs f/hr bs	hrs	Spd Dir Time	Spd Dir Time	<500 <1000 <3000	Press (mb)	Press (mb)	Press (mb)	<500 <1000 <3000	<500 <1000 <3000	Alt (m)	Press (mb)	Press Tend	SLP (mb)	24-hour Pressure				
12-15Z	90	-32.5	-37.8	-29.8	-33.6		9	90	1255						28.97	977.2	3015	981.7					
15-18Z	90	-32.5	-37.8	-29.8	-33.6		10	90	1736						28.97	977.2	3015	981.7					
18-21Z	70	-30.2	-35.0	-29.4	-32.5		15	100	1828						29.07	980.7	1017	985.2	8.0				
21-24Z	12 hr Max/Min						17	80	32						29.17	984.1	1018	988.6	12.5				
00-03Z	50	-37.5	-43.6	-30.0	-37.6		23	50	537	28	50	536	8	70	29.17	984.1	1018	988.6					
03-06Z	20	-34.2	-39.6	-34.2	-37.7		22	50	743						29.17	984.1	1018	988.6					
06-09Z	40	-34.2	-39.6	-34.2	-37.7		22	50	1148	27	50	800	8	10	29.27	987.3	1010	991.9					
09-12Z	12 hr Max/Min						22	50	1148	27	50	800	8	10	29.27	987.3	1010	991.9					
12-15Z	12 hr Max/Min						22	50	1148	27	50	800	8	10	29.27	987.3	1010	991.9					
15-18Z	12 hr Max/Min						22	50	1148	27	50	800	8	10	29.27	987.3	1010	991.9					
18-21Z	12 hr Max/Min						22	50	1148	27	50	800	8	10	29.27	987.3	1010	991.9					
21-24Z	12 hr Max/Min						22	50	1148	27	50	800	8	10	29.27	987.3	1010	991.9					
00-03Z	12 hr Max/Min						22	50	1148	27	50	800	8	10	29.27	987.3	1010	991.9					
03-06Z	12 hr Max/Min						22	50	1148	27	50	800	8	10	29.27	987.3	1010	991.9					
06-09Z	12 hr Max/Min						22	50	1148	27	50	800	8	10	29.27	987.3	1010	991.9					
09-12Z	12 hr Max/Min						22	50	1148	27	50	800	8	10	29.27	987.3	1010	991.9					
12-15Z	12 hr Max/Min						22	50	1148	27	50	800	8	10	29.27	987.3	1010	991.9					
15-18Z	12 hr Max/Min						22	50	1148	27	50	800	8	10	29.27	987.3	1010	991.9					
18-21Z	12 hr Max/Min						22	50	1148	27	50	800	8	10	29.27	987.3	1010	991.9					
21-24Z	12 hr Max/Min						22	50	1148	27	50	800	8	10	29.27	987.3	1010	991.9					
00-03Z	12 hr Max/Min						22	50	1148	27	50	800	8	10	29.27	987.3	1010	991.9					
03-06Z	12 hr Max/Min						22	50	1148	27	50	800	8	10	29.27	987.3	1010	991.9					
06-09Z	12 hr Max/Min						22	50	1148	27	50	800	8	10	29.27	987.3	1010	991.9					
09-12Z	12 hr Max/Min						22	50	1148	27	50	800	8	10	29.27	987.3	1010	991.9					
12-15Z	12 hr Max/Min						22	50	1148	27	50	800	8	10	29.27	987.3	1010	991.9					
15-18Z	12 hr Max/Min						22	50	1148	27	50	800	8	10	29.27	987.3	1010	991.9					
18-21Z	12 hr Max/Min						22	50	1148	27	50	800	8	10	29.27	987.3	1010	991.9					
21-24Z	12 hr Max/Min						22	50	1148	27	50	800	8	10	29.27	987.3	1010	991.9					
00-03Z	12 hr Max/Min						22	50	1148	27	50	800	8	10	29.27	987.3	1010	991.9					
03-06Z	12 hr Max/Min						22	50	1148	27	50	800	8	10	29.27	987.3	1010	991.9					
06-09Z	12 hr Max/Min						22	50	1148	27	50	800	8	10	29.27	987.3	1010	991.9					
09-12Z	12 hr Max/Min						22	50	1148	27	50	800	8	10	29.27	987.3	1010	991.9					
12-15Z	12 hr Max/Min						22	50	1148	27	50	800	8	10	29.27	987.3	1010	991.9					
15-18Z	12 hr Max/Min						22	50	1148	27	50	800	8	10	29.27	987.3	1010	991.9					
18-21Z	12 hr Max/Min						22	50	1148	27	50	800	8	10	29.27	987.3	1010	991.9					
21-24Z	12 hr Max/Min						22	50	1148	27	50	800	8	10	29.27	987.3	1010	991.9					
00-03Z	12 hr Max/Min						22	50	1148	27	50	800	8	10	29.27	987.3	1010	991.9					
03-06Z	12 hr Max/Min						22	50	1148	27	50	800	8	10	29.27	987.3	1010	991.9					
06-09Z	12 hr Max/Min						22	50	1148	27	50	800	8	10	29.27	987.3	1010	991.9					
09-12Z	12 hr Max/Min						22	50	1148	27	50	800	8	10	29.27	987.3	1010	991.9					
12-15Z	12 hr Max/Min						22	50	1148	27	50	800	8	10	29.27	987.3	1010	991.9					
15-18Z	12 hr Max/Min						22	50	1148	27	50	800	8	10	29.27	987.3	1010	991.9					
18-21Z	12 hr Max/Min						22	50	1148	27	50	800	8	10	29.27	987.3	1010	991.9					
21-24Z	12 hr Max/Min						22	50	1148	27	50	800	8	10	29.27	987.3	1010	991.9					

Note 1: Color coding. Green headings indicate blocks the Weather Observer must complete. The remainder are calculated/ completed by MS Excel.

Note 2: Duration should be fractions of an hour.

Note 3: To facilitate MS Excel, the order of entry for Max Wind and Max Gust is changed from conventional. The order is: Spd, Dir, and Time.

Figure 6. Daily Observation Worksheet from McMurdo Station, Antarctica for 12 June 2016.



Figure 7. MET instrumentation at the DOE ARM Southern Great Plains site (Ritsche and Prell 2011).

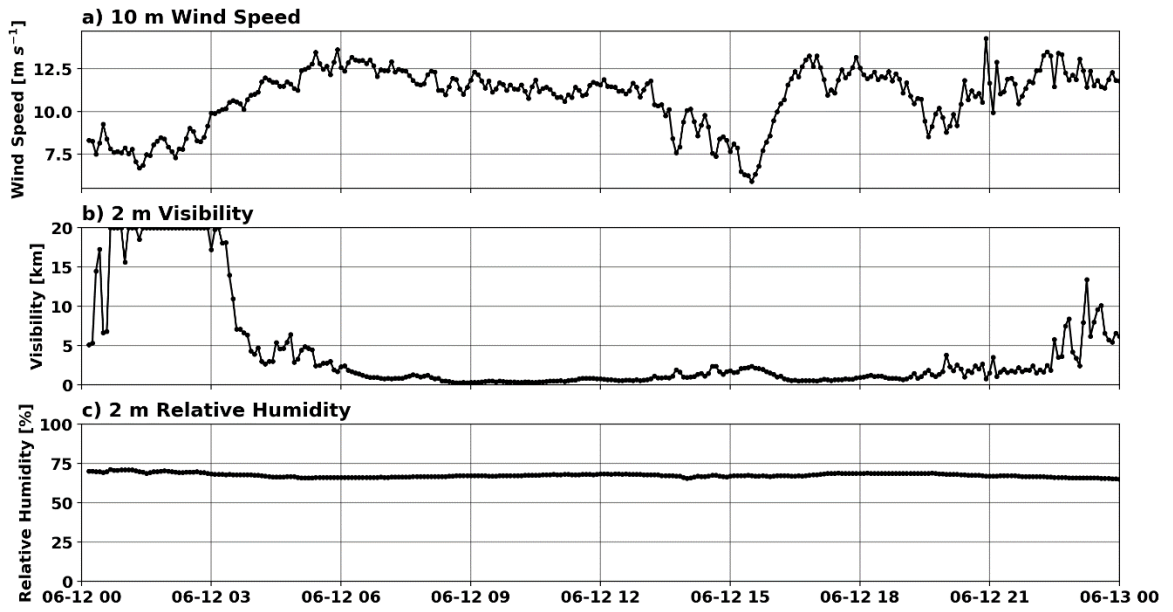


Figure 8. 5-minute mean a) 10 m wind speed, b) 2 m visibility, and c) 2 m RH at McMurdo Station on 12 June 2016 from the MET datastream.



Figure 9. Image of a Parisvel² optical disdrometer at the University of North Dakota Oakville
Prairie Observatory taken by Aaron Kennedy.

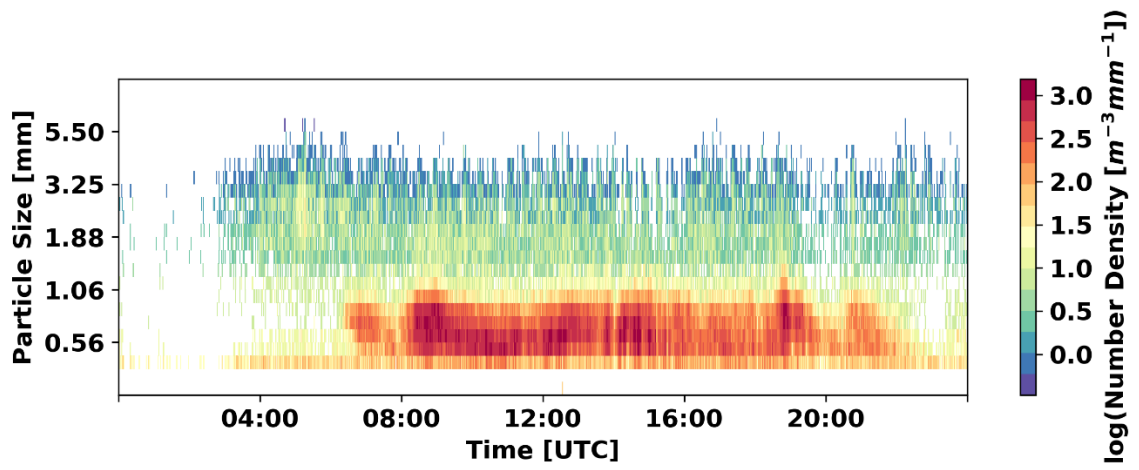


Figure 10. Logarithmic 1-min particle size densities at McMurdo Station on 12 June 2016 measured by the Parisvel2.

Table 1. Periods of missing data for the ceilometer during 2016 determined through manual inspection and ARM data quality reports. The likelihood of BLSN during each period is based on human reporting of BLSN and other available observations.

<i>Date</i>	<i>Hours [UTC]</i>	<i>Issue</i>	<i>BLSN Occurrence</i>
14 April 2016	00-24	Missing data	Unlikely
21 April 2016	13-20	Missing data	~ 3 hours
23 May 2016	00-24	Missing data	Unlikely



Figure 11. Image of the Vaisala CL31 ceilometer at Princess Elisabeth station in Eastern Antarctica. Figure adapted from Gossart et al. (2017).

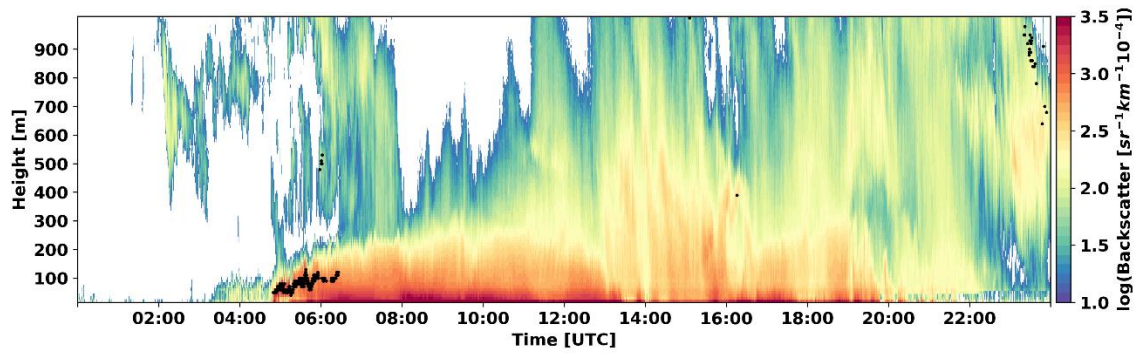


Figure 12. Logarithmic backscatter coefficient and lowest detected cloud base height (shown in black) detected by a Vaisala CL31 ceilometer at McMurdo Station on 12 June 2016.

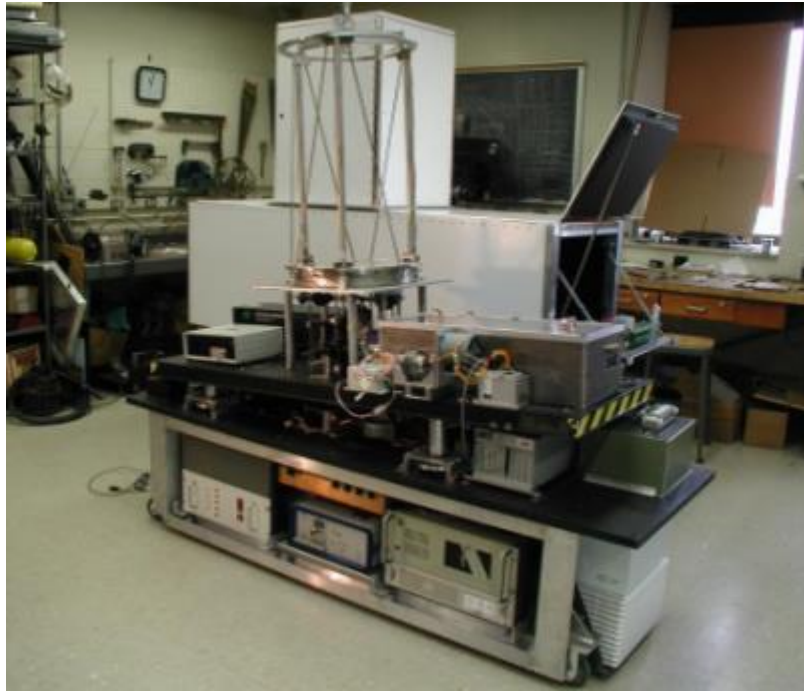


Figure 13. Image of a HSRL with its protective cover removed (Goldsmith 2016). The protective covering is shown behind the HSRL.

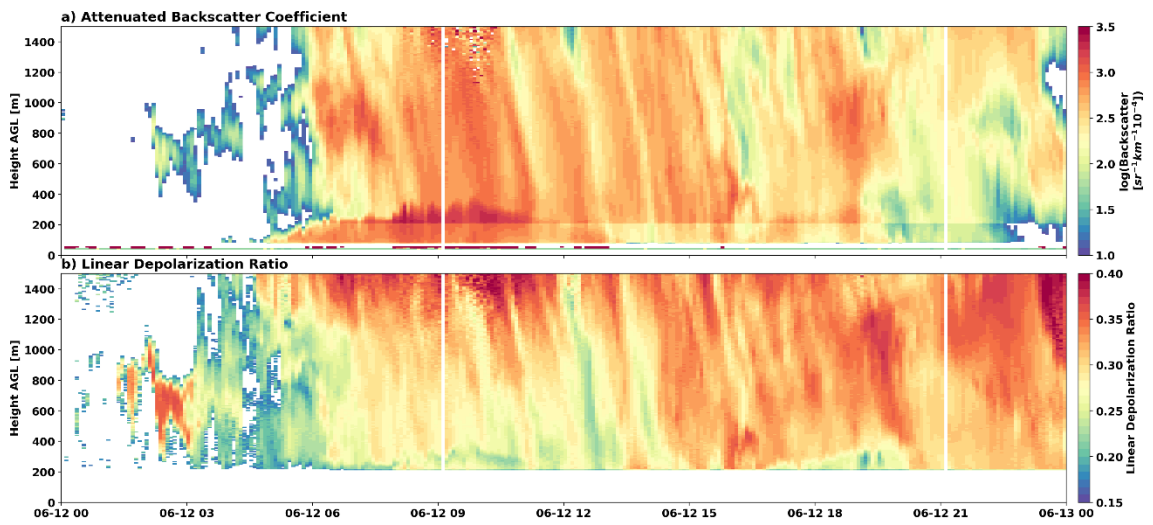


Figure 14. 5-minute average a) attenuated backscatter coefficient and b) linear depolarization ratio from the HSRL for 12 June 2016 at McMurdo Station.

Table 2. As in Table 1 but for the HSRL.

<i>Date</i>	<i>Hours [UTC]</i>	<i>Issue</i>	<i>BLSN Occurrence</i>
14 January 2016	02-13	Questionable data	Unlikely
17-20 January 2016	00-24	Strong laser overlap artifact at ~ 500 m	~ 1-3 hours
19 January 2016	15-18	Questionable data	Unlikely
22 January 2016	08-17	Questionable	Unlikely
26 February 2016	15-24	Missing data	~ 4.5 hours
2 March 2016	00-15	Questionable data	Unlikely
3 March 2016	00-24	Missing data	~ 3 hours
1 April 2016	17-22	Missing data	Unlikely
11 April 2016	05-10	Questionable data	Unlikely
4 June 2016	09-24	Missing data	~ 2 hours
5 June 2016	10-24	Missing data	~ 1 hour
6 June 2016	00-11	Questionable data	Unlikely
30 June 2016	00-09	Questionable data	~ 2.5 hours
2 September 2016	12-17	Missing data	Unlikely
3 November 2016	04-08	Missing data	Unlikely
26 November 2016	05-08	Missing data	Unlikely

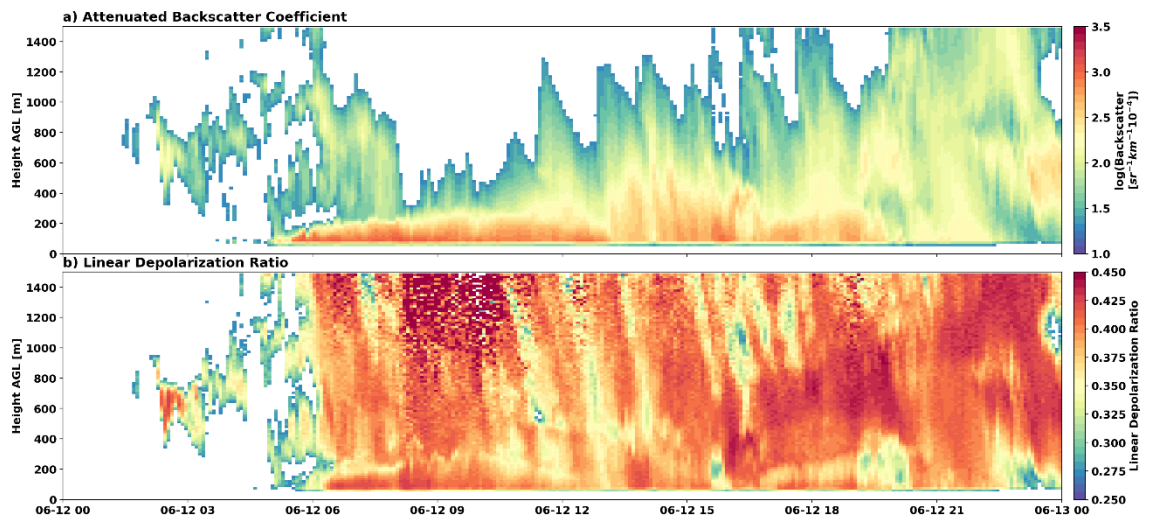


Figure 15. 5-minute mean a) attenuated backscatter coefficient and b) linear depolarization ratio from the MPL for 12 June 2016 at McMurdo Station.

Table 3. As in Table 1, but for the MPL.

<i>Date</i>	<i>Hours [UTC]</i>	<i>Issue</i>	<i>BLSN Occurrence</i>
8 October 2016	00-24	Missing data	~ 5 hours
9 October 2016	00-24	Missing data	~ 4 hours
10 October 2016	00-24	Missing data	Unlikely
11 October 2016	00-24	Missing data	~ 6 hours
12 October 2016	00-16	Missing data	~ 10 hours
6 December 2016	01-14	Missing data	~ 2.5 hours
30 December 2016	00-24	Missing data	Unlikely



Figure 16. Image of the KAZR deployed at DOE ARM Southern Great Plains site (Widener et al. 2012).

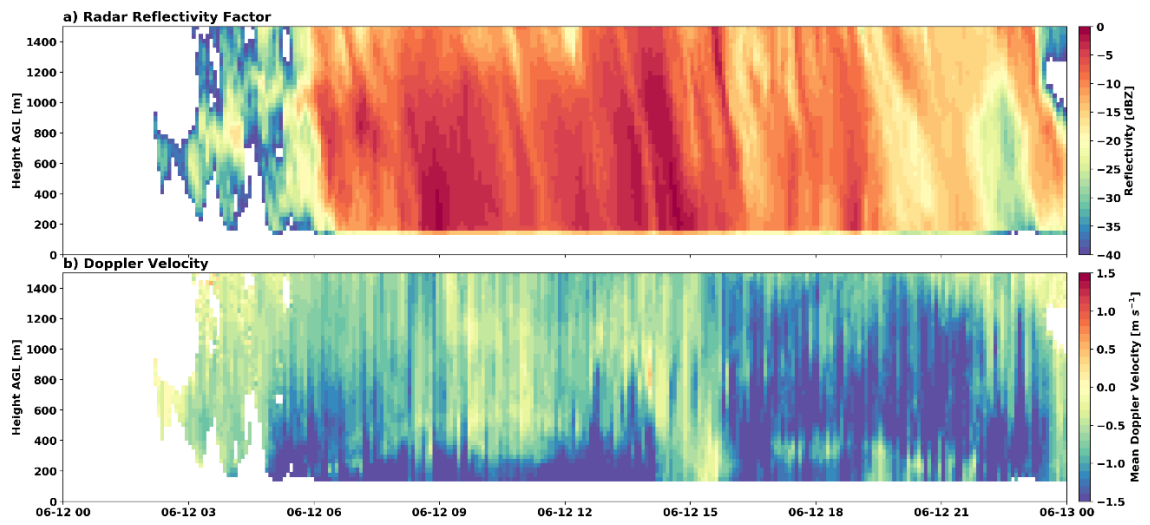


Figure 17. 5-minute mean a) radar reflectivity and b) mean Doppler velocity at McMurdo Station on 12 June 2016 measured by KAZR.

Table 4. As in Table 1, but for the KAZR.

<i>Date</i>	<i>Hours [UTC]</i>	<i>Issue</i>	<i>BLSN Occurrence</i>
18 April 2016	00-24	Missing data	~ 3 hours
27 April 2016	00-24	Missing data	~ 11 hours
28 April 2016	12-24	Missing data	~ 0.5 hours
3 May 2016	13-24	Missing data	~ 15 min
8 May 2016	17-24	Missing data	Unlikely
17 May 2016	00-24	Missing data	~ 15 min
28 May 2016	00-24	Missing data	Unlikely
6 June 2016	00-24	Missing data	Unlikely
19 June 2016	00-24	Missing data	~ 19 hours
6 September 2016	00-24	Missing data	~ 5 hours

Table 5. Summary of properties of the remote sensing instrumentation discussed in Sections 2.2.3-2.2.7.

<i>Instrument</i>	<i>Valid Heights [m]</i>	<i>Temporal Resolution [s]</i>	<i>Vertical Resolution [m]</i>	<i>DOI</i>
<i>Ceilometer</i>	10-7700	16	10	10.5439/1181954
<i>HSRL</i>	50-30000	0.5	7.5	10.5439/1025200*
<i>MPL</i>	100-20000	10	15	10.5439/1468777
<i>KAZR</i>	200-20000	2	30	10.5439/1025214

* Unaveraged HSRL observations retrieved from the University of Wisconsin-Madison Lidar Group Archive (<http://hsrl.ssec.wisc.edu/>)

CHAPTER 3

METHODOLOGY

3.1. Climatology of Human Observations of Blowing Snow at McMurdo Station

Seventeen years (2002-2018) of human observations of BLSN at McMurdo Station are used to provide insight into the climatological properties of BLSN, putting the detailed observations during the AWARE campaign into proper context. These observations also provide a means of verification of BLSN periods identified by the instrumentation, but due to the limitations discussed in Section 2.1, were used as a general assessment tool rather than ground truth.

To determine the climatology of BLSN at McMurdo Station, the total amount of BLSN reported by human observers in each year of the record was calculated. The amount of BLSN was then broken down into times including occurrence with other phenomena such as snow, snow grains, and ice crystals (SN/SG/IC) and/or fog and mist (FG/BR). The distribution of BLSN occurrence was then analyzed on an annual and monthly basis, including assessing the proportion that occurred concurrently with other observed phenomena.

3.2. Ceilometer-Based Blowing Snow Detection Algorithm

Gossart et al. (2017) developed an algorithm to detect BLSN based on ceilometer attenuated backscatter coefficient profiles. This algorithm was applied to Neumayer III and Princess Elisabeth stations in Eastern Antarctica to investigate the frequency of BLSN in the region. Hourly running means were applied to the original 16 s profiles to smooth noise in the data, including artifacts due to partial laser overlap that periodically appear in the 4th

to 6th range bin. A flowchart describing the process of the algorithm is shown in Figure 18. This algorithm will be referred to as the Gossart algorithm herein.

The algorithm is now described. The first step checks that the backscatter coefficient in the instrument's lowest usable bin (bin 2, 10-20 m above the ceilometer) is higher than the clear sky threshold. The clear sky threshold was set by subjectively selecting periods of clear sky observed by the ceilometer and using the 95th percentile of the backscatter coefficient in the lowest usable bin. Next, the algorithm looks for a decreasing profile by checking if the backscatter coefficient in the lowest usable bin is higher than the average of the third to seventh bin (30-80 m). If these two criteria are met, BLSN is detected and the algorithm ascends the profile, bin-by-bin, until the backscatter coefficient begins to increase with height or falls below the clear sky threshold. The algorithm sorts profiles into four categories; non-BLSN, clear sky with BLSN, cloud/precipitation with BLSN, and intense mixed event (shown in Figure 18). The non-BLSN profiles are those that show no ground-based maximum in backscatter coefficient. Schematics showing the three BLSN categories are shown in Figure 19. The BLSN with cloud/precipitation and clear-sky BLSN appear as profiles with high backscatter coefficient in the low levels with and without secondary peaks at higher altitudes, respectively. Intense mixed events are those with very high backscatter coefficient (over $1000 \text{ sr}^{-1} \text{ km}^{-1} 10^{-4}$) in the low levels but may have no clear pattern with height.

As in Gossart et al. (2017), the clear sky signal at McMurdo Station was determined by subjectively selecting profiles that were cloudless with no BLSN. In this study, continuous clear sky periods of at least three hours were selected and the 95th percentile for each bin was found, yielding the clear sky signal used in the algorithm for McMurdo Station

(Figure 20). The only threshold used in the algorithm derived by Gossart et al. (2017) was the clear sky signal in the lowest usable bin. The clear sky thresholds found in Gossart et al. (2017) were 32.5 and 21.0 $\text{sr}^{-1} \text{km}^{-1} 10^{-4}$ in the lowest usable bin for the Neumayer III and Princess Elisabeth stations, respectively. The value found for McMurdo Station was 21.0 $\text{sr}^{-1} \text{km}^{-1} 10^{-4}$ based on approximately 117.5 days of clear sky data. As part of the implemented improvements to the algorithm, the threshold used for each bin was the 95th percentile of the clear sky signal for said bin, rather than only using a single value applied to the entire column.

3.3. A Revised Blowing Snow Detection Algorithm

3.3.1. Temporal Averaging

The hourly running means (225 profiles) of the 16 s raw data used in the Gossart algorithm helped to reduce noise but manual inspection showed that the signal of BLSN events became elongated. This is particularly the case during cyclic events that had breaks in which BLSN did not occur throughout their duration. In this study, the observations were averaged to a common temporal grid spacing so they can be used in concert with a variety of data available from the AMF2. To do this, the 16 s ceilometer profiles were grouped into five-minute periods (18 profiles) and the average profile for each grouping was found. The algorithm then checks for BLSN as in the Gossart algorithm. This is a common interval used with other profiling instruments at ARM sites (e.g. Clothiaux et al. 2000; Mace et al. 2006; Kennedy et al. 2014), meaning that it will be easier to implement the algorithm at other ARM sites and use in concert with a variety of instrumentation. To assess the impact of temporal averaging alone, the Gossart algorithm with adjusted temporal averaging was

applied to the AWARE Campaign data and is referred to herein as the five-minute no thresholds (5-min NT) algorithm.

3.3.2. Meteorological Thresholds

Multiple meteorological thresholds were applied to increase confidence in BLSN occurring at the surface. These included conservative thresholds of 10 km for visibility to ensure backscatter coefficient signal was not decoupled from the surface layer, and a wind threshold of 3 m s^{-1} (Mellor 1965) to remove cases of ice fog with calm winds. Despite these thresholds, advection fog was still falsely detected during the summer months due to profiles with backscatter coefficient maximized at the surface associated with moderate wind speeds. In an effort to remedy this issue, an additional 90% RH threshold was included to separate fog from BLSN. While imperfect (see Section 5.2.3), this value offered the best balance of retaining nearly all of the BLSN signal throughout the year while reducing false positives during the summer months. The algorithm with five-minute averaging and meteorological thresholds applied is referred to as the five-minute algorithm (5-min).

3.4. Assessment of Algorithm Performance

The three versions of the BLSN detection algorithm were compared to human observations to grossly assess performance. Although this is not quite a direct comparison, it can provide insight into the potential skill of the algorithm (or human observers for that matter). To do this, output of the algorithms was grouped into three-hour periods to match the human observations. The output was then converted to binary to show whether BLSN has occurred within the period, rather than show specific categories. BLSN was determined to occur based on the algorithm in each period if at least 20 minutes of BLSN was detected (as in Gossart et al. 2017). The percent correct was calculated for each algorithm based on

two-by-two contingency analysis based on the NOAA Forecast Verification Glossary. The percent correct (*PC*) describes the amount of agreement between the algorithm and the human observers and is calculated as

$$PC = \frac{A + D}{A + B + C + D} \times 100\% \quad (2)$$

where the variables are as defined in Table 6.

3.5. Multi-Instrument Blowing Snow Depth Estimation

To increase confidence in the estimated depth of the detected BLSN plumes, observations from the MPL, HSRL, and KAZR were incorporated into a combined depth estimation algorithm. These instruments do not produce usable data until much higher above the instrument (~100-400 m), so they are most useful during intense mixed events (Category 3). A subset of dates was selected that saw at least two hours of detected Category 3 BLSN or that had a depth of at least 150 m based on the five-minute algorithm and no missing data. This resulted in 41 days to be analyzed with the additional instrumentation.

First, all observations were averaged to a common grid with five-minute temporal and 30 m vertical grid spacing. The vertical grid spacing of 30 m was selected because it is the resolution of the coarsest dataset (KAZR). The following variables were assessed to characterize BLSN depth: ceilometer, MPL and HSRL backscatter coefficient; MPL and HSRL linear depolarization ratio (LDR); and color ratio. Observations from the KAZR were only used in the color ratio calculations; manual inspection of observations on BLSN days showed that KAZR direct observations were not useful in determining plume depth. All variables were combined with the results of the five-minute algorithm to yield a probabilistic view of the BLSN plume to gain further insight into the likely depth of the

layer. The following sections describe how each variable is treated in the combined algorithm and the methods used to determine the top of the layer using a probabilistic approach.

3.5.1. Attenuated Backscatter Coefficient

An adapted version of the five-minute algorithm was applied to attenuated backscatter coefficients from the MPL and HSRL. It was also applied to 30 m averaged ceilometer profiles. The clear sky threshold was calculated for backscatter coefficient for each instrument using the same methodology as for the ceilometer, shown in Figure 21. The threshold values of clear sky backscatter coefficient in the lowest usable bin are given in Table 7. The HSRL clear sky signal has a similar magnitude to that of the ceilometer in the lowest kilometer, while the MPL sees higher noise. The HSRL laser overlap signal is visible as an increase in backscatter coefficient at around 200 m.

The algorithm then was applied as in Gossart et al. (2017), shown in the flowchart in Figure 22. It begins by checking that backscatter coefficient is above the clear sky threshold in the lowest usable bin and shows a decreasing profile with height, then ascends the profile until the backscatter coefficient decreases below the clear sky threshold or begins increasing again with height. Analysis of the 30 m averaged profiles begins at bin 2 (30-60 m) for the ceilometer, bin 5 (120-150 m) for the MPL, and bin 8 (210-240 m) for the HSRL. These levels were selected as the first bin in which laser overlap does not produce erroneous backscatter coefficient measurements. These algorithms are referred to herein as 30 m CEIL, MPL BS, and HSRL BS.

3.5.2. Linear Depolarization Ratio

Because BLSN particles tend to be more spherical than falling ice crystals, LDR can be used to help distinguish between the two habits (Sassen 1991, 1977). Walden et al. (2003) collected microscope images of ice crystals at the South Pole Station and found that falling snow tends to be composed of sector-plate clusters, bullet clusters, and snow-grain columns, while BLSN particles are small and spheroidal, meaning the LDR should be lower for BLSN than for falling snow. The analysis of LDR profiles is based on the assumption that its value within the BLSN plume will differ from that above it. This helps to distinguish the BLSN depth during precipitation events.

A flowchart describing the LDR algorithm is shown in Figure 23. Analysis begins by checking that the instrument's backscatter coefficient is above the clear sky threshold for the lowest usable bin to ensure particles are present, and if the LDR in said bin is less than the upper level average. The upper level used for this analysis is 1200-1440 m. If both criteria are met, the algorithm ascends the profile and checks that the LDR in each bin remains lower from the mean of the layer above it by at least 0.01. Appropriate averaging layer depth for each instrument was determined through manual inspection of the data. A layer of 210 m and 390 m was used for the HSRL and MPL, respectively. Next, it checks that the instrument's backscatter coefficient remains above the clear sky threshold. A 210 m layer was used to assess whether the profile is decreasing or increasing with height, rather than using a single bin, because the LDR tends to yield noisy profiles. The top of the layer was denoted as the bin in which either the backscatter falls below the clear sky threshold, or where the difference between the bin's LDR and that of the layer above falls below 0.01. These algorithms are referred to going forward as MPL LDR and HSRL LDR.

3.5.3. Color Ratio

The color ratio (CR) is a derived quantity that acts as a proxy for particle size, and is calculated as

$$CR = \frac{\beta_{radar}}{\beta_{lidar}} \quad (3)$$

where β_{radar} and β_{lidar} represent the attenuated backscatter coefficients derived from a radar and lidar, respectively (Bourdages et al. 2009). As BLSN particles tend to be smaller than that of falling snow (Gordon and Taylor 2009), CR may be able to help distinguish the two populations of particles. Smaller particles yield a lower CR, typically in the range of 10^{-8} to 10^{-5} for boundary layer ice crystals (Bourdages et al. 2009). In this study, CR was calculated using KAZR reflectivity factor and HSRL backscatter coefficient. Radar attenuated backscatter coefficient is derived from the linear equivalent radar reflectivity factor, Z_e , based on the analysis presented in Intrieri et al. (1993);

$$\beta_{radar} = Z_e K^2 \frac{\pi^4}{4\lambda^4} \quad (4)$$

where λ represents the radar wavelength (8.6 mm), and K^2 is the dielectric constant. The value of K^2 used for ice is 0.176 (Rauber and Nesbitt 2018). As with the LDR, the CR is expected to aid only when precipitation is occurring and there are different populations of particles to distinguish between.

The CR BLSN depth detection algorithm is outlined in Figure 24. Profile analysis begins by checking if the color ratio in the lowest usable bin (bin 10, 300-330 m) is greater than 10^{-8} to suggest the presence of low-level particles, the lower end of the CR range given for ice in the boundary layer by Bourdages et al. (2009). It also verifies that the CR in the lowest usable bin is less than the average of the 300 m above it, as a generally increasing

trend would be expected with height. If these two criteria are met, the algorithm ascends the profile, checking that the CR in each bin is less than the average of the two bins directly above, and that it does not exceed 10^{-5} , suggesting the majority of the particles in the bin are larger than expected for BLSN (Bourdages et al. 2009). This algorithm is referred to as the CR algorithm going forward.

3.5.4. Probabilistic Blowing Snow Depth Estimation

The BLSN depth estimation methods described in Sections 3.5.1-3.5.3 were combined with the results of the five-minute algorithm (outlined in Section 3.3) to produce the best approximation of the depth of the BLSN layer based on the available observations. To do this, the results of each algorithm were converted to binary; each bin received a value of one if it met the criteria for BLSN based on that algorithm and a zero if it did not. The total number of algorithms that designated the bin as BLSN was then divided by the number of algorithms that were valid to assess in said bin. The number of valid algorithms was determined based on the criteria outlined in Table 8. For example, if the five-minute and 30 m ceilometer algorithms both estimate a BLSN depth of less than 100 m for a time that is Category 1 or 2, then the algorithms applied to MPL and HSRL data are not valid, therefore there are only 2 valid algorithms at that time. The result is an array in which each bin's value is a fraction representing the agreement of the valid algorithms. This can be interpreted as relative certainty as to whether BLSN is occurring within the cell.

To estimate the BLSN depth, the altitude at which the fraction falls below 0.5 for each period of BLSN was determined. To reduce unrealistic increases or decreases in BLSN depth, a running mean was applied using a window of five profiles (25 minutes). This reduces abrupt changes in BLSN depth that are physically unlikely; for example, the

estimated depth of BLSN being 100 m in one five-minute period and 800 m in the next. This window length was selected to be a period long enough to reduce the effects of noise and inconsistencies in the profile while still maintaining the temporally unsteady nature of the phenomenon. Sensitivity testing for the probabilistic algorithm is conducted through varying the threshold used and the length of the smoothing window to assess their impacts on the height of the layer.

3.5.5. Blowing Snow Depth Assessment Methods

Since there is no way of identifying the true depth of the BLSN at any given time, algorithm performance was assessed based on the degree of agreement between the different methods and consistency of the results when different thresholds were selected. All thresholds used were varied to assess the change in detected BLSN depth depending on the selected threshold. Clear sky thresholds were varied as described in Section 3.4.3 to assess their impact on the backscatter algorithms. The layers used in profile analysis for the color ratio and LDR algorithms were also varied.

The results of the probabilistic depth algorithm were compared to the depth results from the five-minute algorithm to assess the impact of incorporating additional observations and changing to a probabilistic depth detection approach. The resulting BLSN plume depths were investigated based on meteorological variables to determine if any patterns emerge. Finally, case studies were performed to illustrate the performance of the algorithm and highlight its performance.

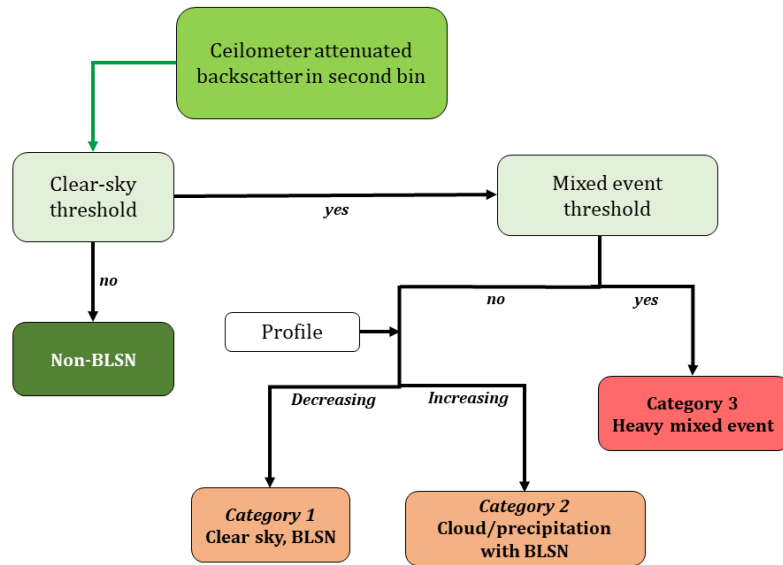


Figure 18. Flowchart describing the BLSN detection algorithm (adapted from Gossart et al. 2017).

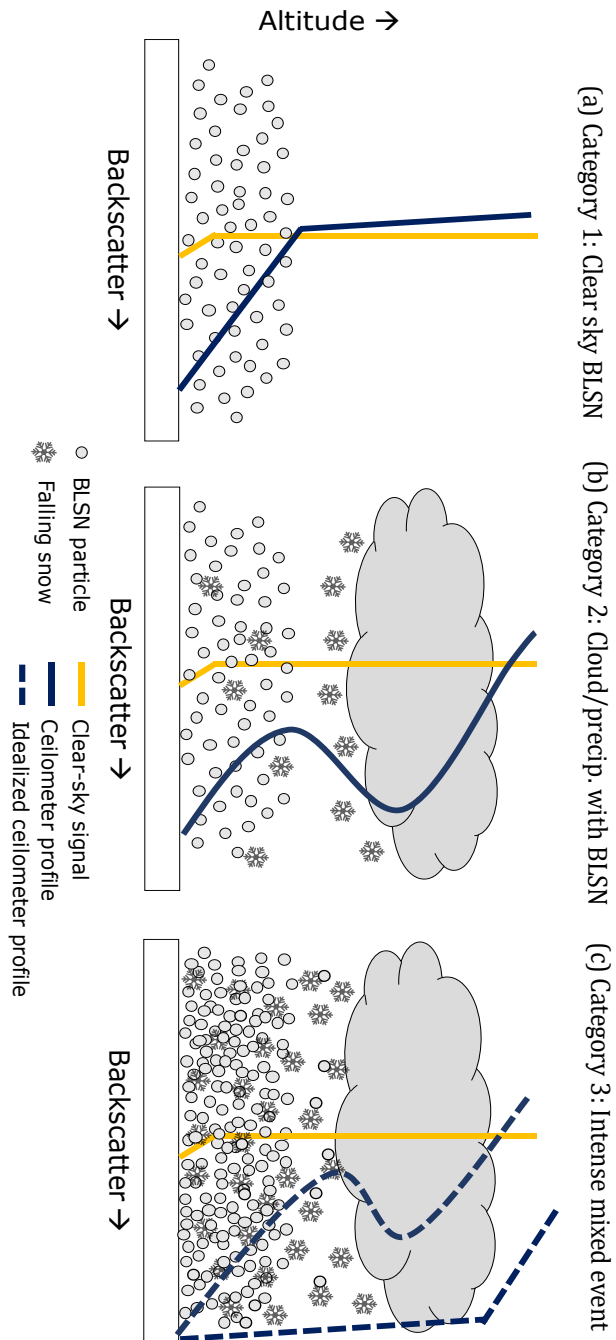


Figure 19. Diagrams of (a) clear-sky BLSN, (b) clouds/precipitation with BLSN, and (c) heavy mixed events. Orange and dark blue lines represent the clear-sky signal and idealized backscatter coefficient profile from the ceilometer, respectively.

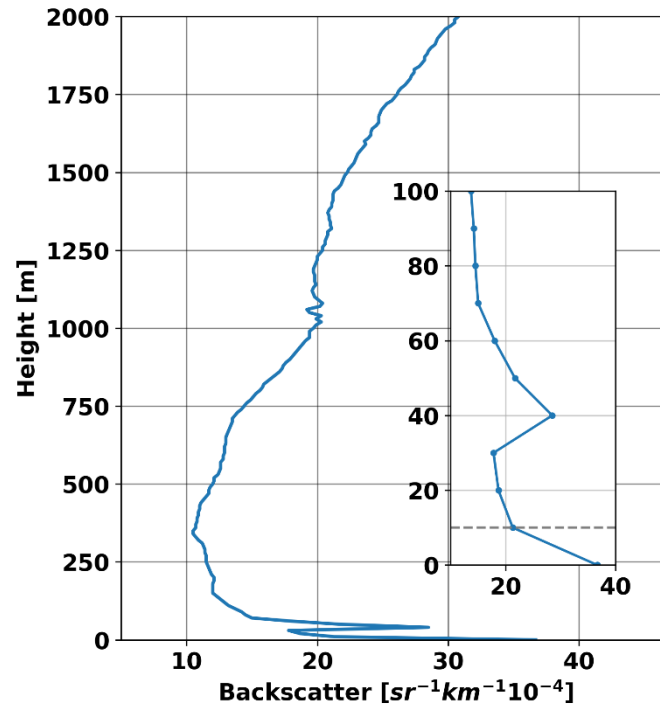


Figure 20. 95th percentile clear sky backscatter profile for McMurdo Station during the AWARE Campaign. The lowest 100 m of the profile is highlighted in the inset.

Table 6. 2x2 Contingency table for comparisons between human observations and algorithm results. BLSN refers to periods in which BLSN was detected, and non-BLSN means it was not observed. Human and algorithm refer to the human observations and algorithm results, respectively.

		Human	
		<i>BLSN</i>	<i>Non-BLSN</i>
Algorithm	<i>BLSN</i>	A	B
	<i>Non-BLSN</i>	C	D

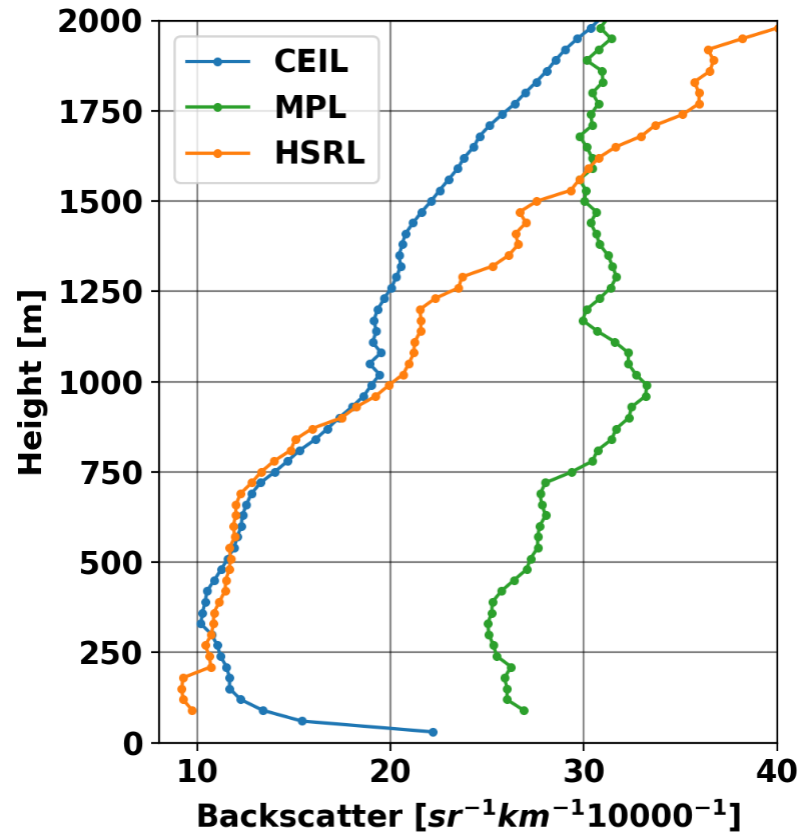


Figure 21. Clear sky 30 m averaged attenuated backscatter coefficient profiles for the ceilometer (CEIL), MPL, and HSRL.

Table 7. Altitude and clear sky threshold backscatter coefficient for the lowest usable bin for the 30 m and five-minute averaged ceilometer, MPL, and HSRL observations.

<i>Instrument</i>	<i>Height of lowest usable bin [m]</i>	<i>Clear sky threshold in lowest usable bin [$sr^{-1} km^{-1} 10^{-4}$]</i>
Ceilometer	30-60	22.17
MPL	120-150	26.01
HSRL	210-240	10.70

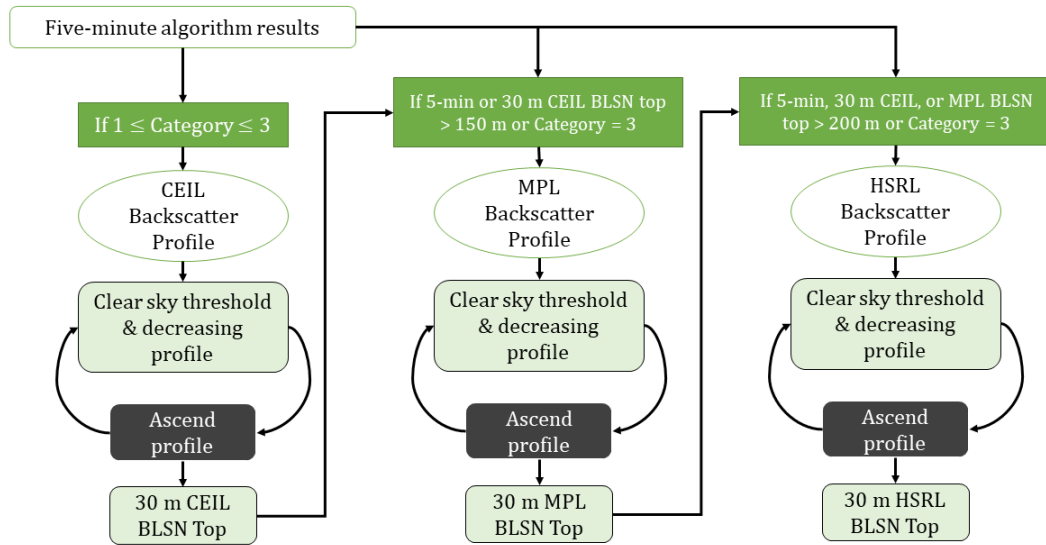


Figure 22. Flowchart describing the BLSN depth detection algorithm applied to backscatter coefficient profiles from the ceilometer (CEIL), MPL, and HSRL.

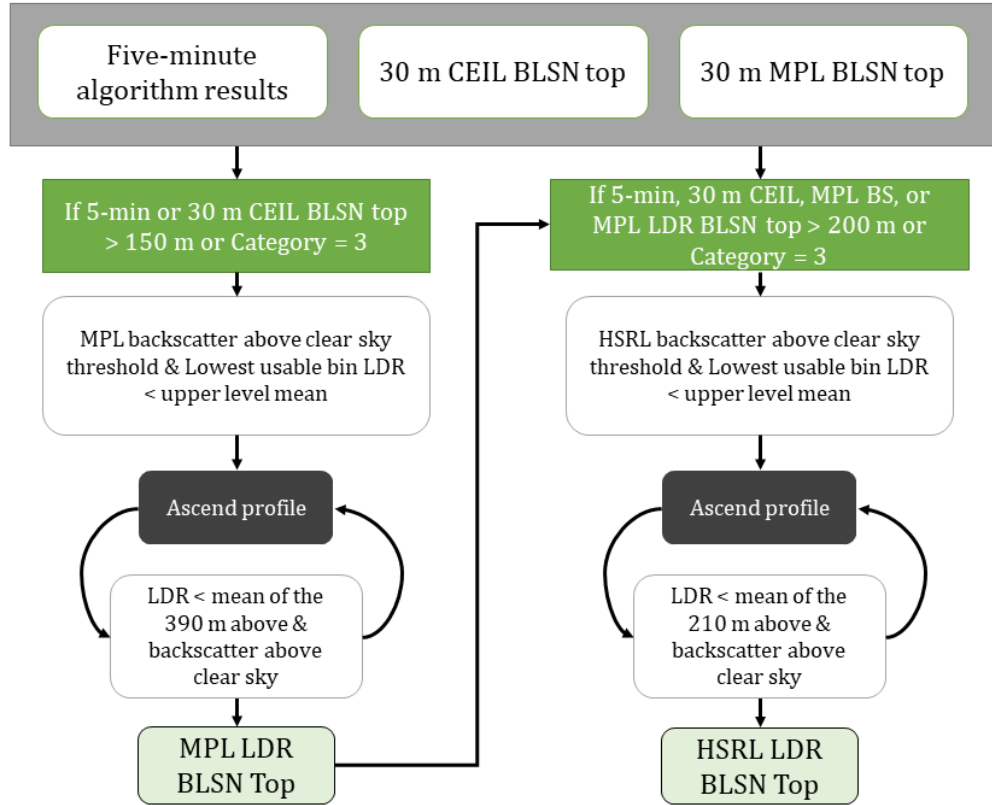


Figure 23. Flowchart describing the BLSN depth detection algorithm applied to LDR profiles from the MPL and HSRL.

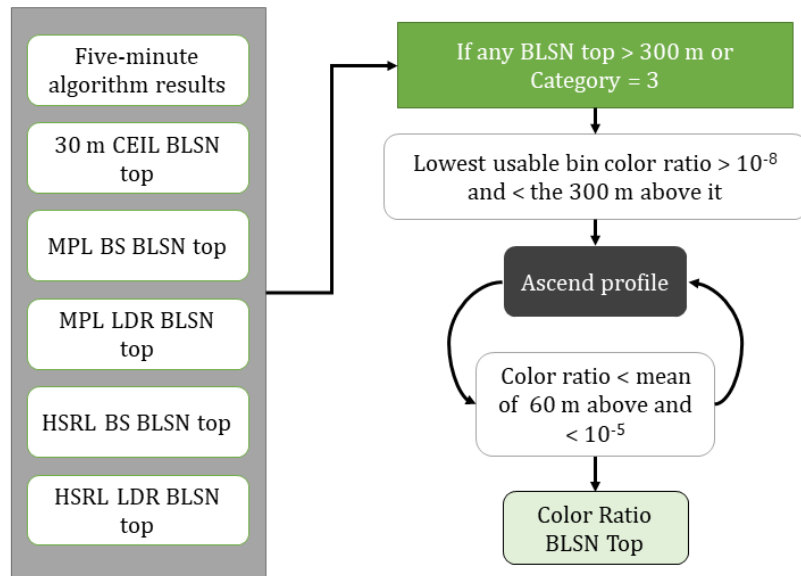


Figure 24. Flowchart describing the BLSN depth detection algorithm applied to color ratio profiles.

Table 8. Criteria for validity of each algorithm.

<i>Algorithm</i>	<i>Criteria for Validity</i>
5-min Algorithm	5-min Algorithm Category 1-3
30 m CEIL	5-min Algorithm Category 1-3
MPL BS	(Depth of 5-min or 30 m CEIL algorithms at least 100 m) or (5-min Category 3)
MPL LDR	(Depth of 5-min or 30 m CEIL algorithms at least 100 m) or (5-min Category 3)
HSRL BS	(Depth of 5-min, 30 m CEIL, MPL BS, or MPL LDR algorithm at least 200 m) or (5-min Category 3)
HSRL LDR	(Depth of 5-min or 30 m CEIL, MPL BS or MPL LDR algorithms at least 200 m) or (5-min Category 3)
Color Ratio	(Depth of 5-min or 30 m CEIL, MPL BS, MPL LDR, HSRL BS, or HSRL LDR algorithms at least 300 m) or (5-min Category 3)

CHAPTER 4

CASE STUDIES

To demonstrate properties of the algorithms, three case studies are presented that represent the variety of BLSN events McMurdo station receives.

4.1. 4-5 July 2016

From 2200 UTC 4 July 2016 to 0600 UTC 5 July 2016, a BLSN event was observed by both human observers and the ceilometer-based algorithms (Figure 25). Human observers noted snow during the event (Figure 25a), but this is not supported by the backscatter coefficient profiles at the AMF2 (Figure 25b). Analysis of vertically pointing radar data revealed surface-based backscatter coefficient < 500 m AGL decoupled from cirrus clouds at heights above 4 km AGL (not shown). In other words, this BLSN event was independent of falling precipitation. Initial detection of BLSN by the AMF2 around 2200-2300 UTC was tied to rapid fluctuations in wind speed and direction suggesting the influence of topography. The high Parsivel² particle counts around 2300 UTC for example (Figure 25c), were associated with northeasterly winds shifting to northwesterly before shifting back by 2345 UTC. Backscatter coefficient profiles after this time led to straightforward detection of the BLSN layer which had heights that reached up to ~ 200 m (Figure 25b). Modulation of the BLSN layer can be attributed to a change in wind intensity. During the most prolonged portion of the event (0000-0230 UTC), increasing BLSN depths can be seen as the wind speed increased up to 17 m s^{-1} (Figure 25d). Eventually, backscatter coefficient became intense enough to classify the BLSN as an intense mixed case (Category 3), although this is clearly not the case. As the winds began to subside by 0200 UTC plume

heights dropped below the top of the backscatter coefficient column. This is caused by the backscatter coefficient decoupling from the surface layer, suggesting that as the event waned, BLSN became suspended above the surface layer. At around 0300 UTC, the BLSN becomes more variable, shown through the oscillating visibility observations and periodic ground-based peaks in backscatter coefficient. It is possible that the BLSN organized into horizontal convective rolls at this time (e.g. Kennedy and Jones 2020), but without satellite imagery, this is purely speculative.

This case demonstrates peculiar behavior of the Parsivel² in high wind environments as noted by Friedrich et al. (2013) and discussed further in Section 5.2.5. Particle number density peaks in the smallest particle size bins with a moderate number of larger particles with diameters of 2-5 mm (Figure 25c). The periods of highest wind speeds are associated with broad increases in large particles detected. Provided that this case is purely BLSN, these particle size distributions do not appear to be realistic as the majority of BLSN particles are < 500 μ m (Budd et al. 1966; Pomeroy and Male 1988; Gordon and Taylor 2009).

The results of the probabilistic depth estimation and its contributing algorithms are shown in Figure 26. The mean depth during the event was 87.1 m, with a maximum depth of 216.0 m. For most of this case, the five-minute algorithm appears to appropriately designate the top of the plume. The results of the 30 m CEIL and MPL BS algorithms agree with that of the five-minute algorithm. The HSRL BS algorithm is only valid for approximately 35 minutes due to shallow BLSN during most of the event and the algorithm's criteria not being met. The shallow nature of the event also limited analysis for the LDR and CR algorithms. The CR algorithm was valid for approximately 20 minutes

(during periods designated as Category 3). Despite the short duration, there were peaks of low CR at the bottom of the profile indicative of BLSN.

Generally, the probabilistic depth estimation remained within ~50 m of the results of the five-minute algorithm during this event, with a mean absolute difference of 38.1 m. These results suggest that the use of ceilometer backscatter coefficient adequately estimated BLSN depth during clear sky events, though supplementing it with backscatter observations from other instrumentation may help to increase confidence. Additionally, it is possible that the 25-minute running means applied to smooth the BLSN top may reduce precision in detection of the plume, particularly around 2300 4 July to 0000 5 July, when the BLSN depth may be rapidly fluctuating.

4.2. 2 July 2016

A BLSN event occurred at McMurdo Station on 2 July 2016 from approximately 1430 to 1930 UTC. This event was detected as a Category 2 and 3 event by the five-minute algorithm (though several time periods are indicated as Category 1 as the cloud layer was decoupled from the BLSN) and was associated with some falling snow according to human observations. Figure 27 shows human observations, ceilometer backscatter coefficient, Parsivel² observations, and environmental conditions during the event. BLSN initiation was associated with northeasterly winds increasing from approximately 3 to 10 m s⁻¹ and a sharp drop in temperature from -33 to -40°C over ~15 minutes. The highest particle number densities occurred in the smallest size bins (< 1 μm), with few larger particles being measured. While some larger size particles are detected by the instrument, a clear bimodal distribution was not seen as in the previous case. This is a realistic particle size distribution

that would be expected for a BLSN event (Pomeroy and Male 1988). It can also be noted that the wind speed was lower than the previous event throughout its duration.

Figure 28 shows the results of all contributing algorithms (a-f) and the probabilistic BLSN depth estimation (g). Early in the event (1430-1530 UTC), the ceilometer observations (Figure 28a-b) showed some separation of high backscatter coefficient values above and below ~ 100 m, but the MPL BS and MPL LDR algorithms did not see this separation, and the top of the probabilistic BLSN layer was denoted near 200 m. The five-minute, 30 m CEIL, MPL BS algorithms agreed well on detected depths from ~ 1530 to 1615 UTC, then the five-minute algorithm began to deviate, falling to depths of less than 100 m. At this time, the probabilistic algorithm most closely followed the 30 m CEIL and MPL BS algorithms, with the HSRL BS algorithm becoming useful later on in the event (after 1700 UTC).

The average absolute difference between the five-minute and probabilistic algorithms during this event was 41.9 m. The largest differences occurred when the five-minute algorithm detected BLSN less than 100 m thick while the other backscatter coefficient-based algorithms yielded heights closer to 200 m. This case was relatively simple, and likely did not have substantial precipitation occurring as the backscatter coefficient profiles were fairly straightforward. The LDR and CR algorithms were not valid for the majority of the event as the height of the BLSN likely below the detection level most of the time.

4.3. 12 June 2016

An intense mixed event occurred at McMurdo Station on 12 June 2016, from approximately 0400 to 2300 UTC. This event saw falling snow and BLSN throughout its duration (Figure 29). The onset of the event can be seen clearly in the visibility observations

and was associated with increasing wind speed and low-level backscatter coefficient around 0300 UTC. Further investigation of other radar and lidars demonstrated that ceilometer observations did not penetrate through the entire column of hydrometeors (Figure 30). From 0800 UTC onward, reflectivity was noted up to 5km AGL from KAZR observations (not shown).

Parsivel² number densities showed little evidence of artifacts due to high wind speeds. The only hint of this artificial distribution occurred around 0600 UTC which also happened to be a local maximum for wind speed at 13 m s^{-1} . While values increase in the smallest size bins first, time periods of falling and BLSN were associated with a higher density of particles from 0.5 to 1 mm. Particle counts are also notably higher than those seen in the previous cases.

The algorithm appropriately detects the presence of BLSN, but there are periods when the detected BLSN plume height is inconsistent. For example, heights from 1300 UTC onward fluctuate depending on the presence and intensity of fall streaks modifying the column of ceilometer backscatter coefficient based on observations from the other available remote sensing instrumentation, demonstrating the need of incorporating further observations. The results of the multi-instrument depth estimation approach are shown in Figure 30. The average depth of BLSN during this event was 226.2 m. The maximum depth was found to be 552.0 m, which occurred at 1040-1050 UTC. The four backscatter coefficient-based algorithms (Figure 30a-d) agreed well with each other early in the event (until approximately 1200 UTC), though the HSRL backscatter coefficient profiles appeared to be noisier. The CR and HSRL LDR algorithms designate the top of the layer to be around the same height for much of this period as well. After 1200 UTC, fall streaks

overpowered the BLSN signal, shown clearest in the LDR and color ratio profiles between 1300-1500 UTC. After this period, the ceilometer and MPL backscatter coefficient profiles became more unclear, yielding little continuity in the heights detected by the individual algorithms throughout much of the rest of the event (Figure 30a-c). Regardless of lidar instrument, this is a good indication of the limitations of backscatter observations; at some point it becomes difficult to distinguish fall streaks from the BLSN layer.

At this point, the LDR algorithms display the clearest signal of a BLSN layer; a region of lower LDR is present in the lowest 400-500 m. The HSRL BS algorithm also designated the top of the layer to be near the top of the region of low LDR, increasing confidence that this may be the true BLSN depth.

The differences between the five-minute and probabilistic algorithms was much greater during this case than the previous cases. While the average absolute height difference between the two algorithms was 115.6 m, the difference was found to be at least 300 m for almost two hours of the event. The maximum difference occurred at 1855 UTC, when the five-minute algorithm detected a depth of 975.0 m, compared to the more realistic depth of 354.0 m given by the probabilistic algorithm. This case helps to illustrate how all of the variables aid in characterizing the BLSN plume during intense mixed events. Additionally, it shows how any one algorithm may err, but the probabilistic approach helps to give a more accurate overall view of the plume regardless of artifacts.

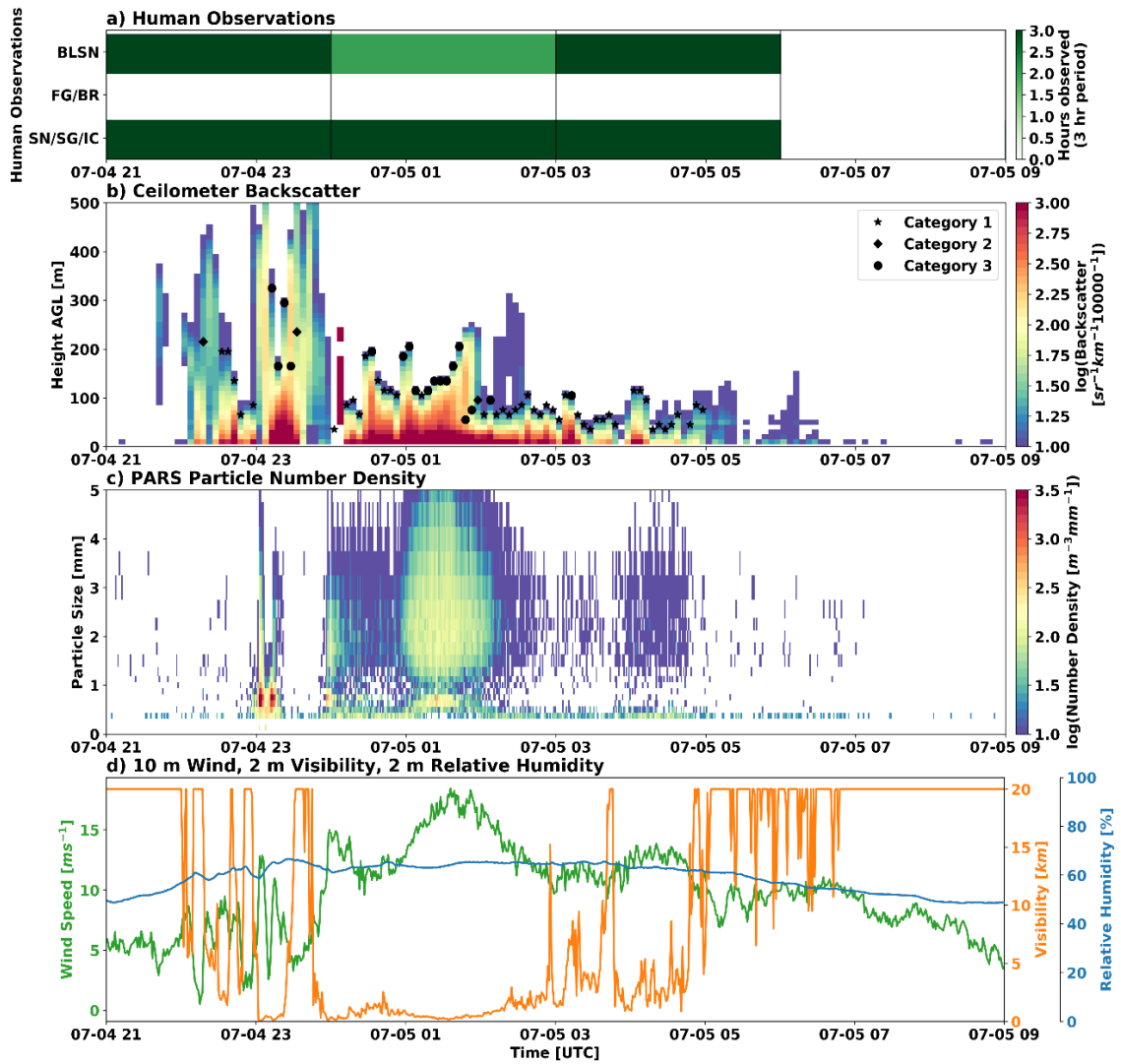


Figure 25. a) Human observations, b) five-minute average ceilometer attenuated backscatter coefficient, c) five-minute average Parsivel² particle number density, and d) five-minute average wind speed (green), visibility (orange), and RH (blue) from MET instrumentation on 4-5 July 2016 at McMurdo Station. BLSN tops derived from the five-minute algorithm are denoted by black stars, diamonds, and dots corresponding to Categories 1, 2, and 3, respectively.

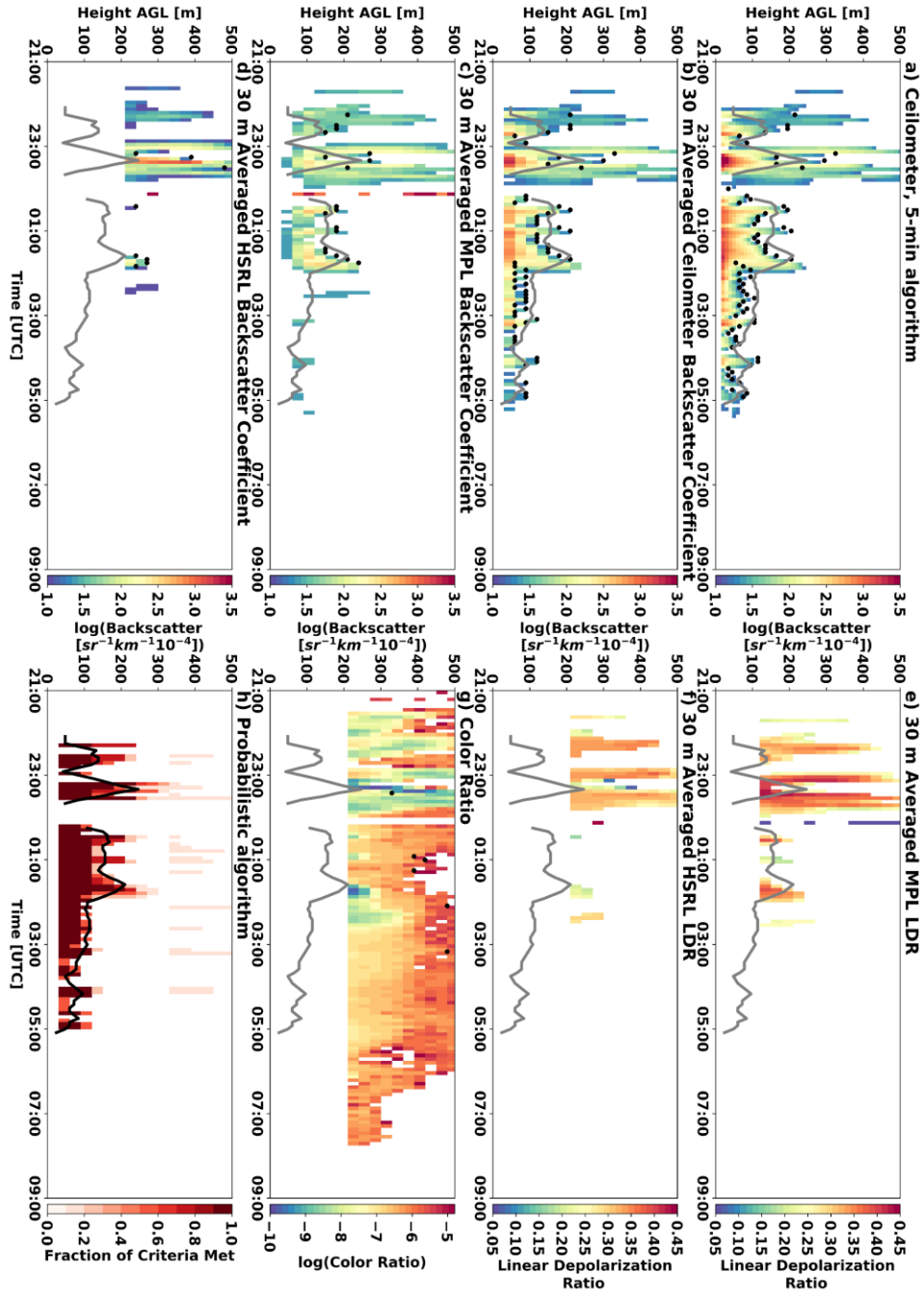


Figure 26. a) 5-minute averaged ceilometer backscatter coefficient (as used in the 5-min algorithm), b) 30 m averaged ceilometer backscatter coefficient, c) MPL backscatter coefficient, d) MPL LDR, e) HSRL backscatter coefficient, f) color ratio, and g) probabilistic algorithm results for 4-5 July 2016. Black dots indicate the top of the BLSN plume as indicated by the single algorithm. The gray line shows the BLSN depth indicated by the probabilistic algorithm.

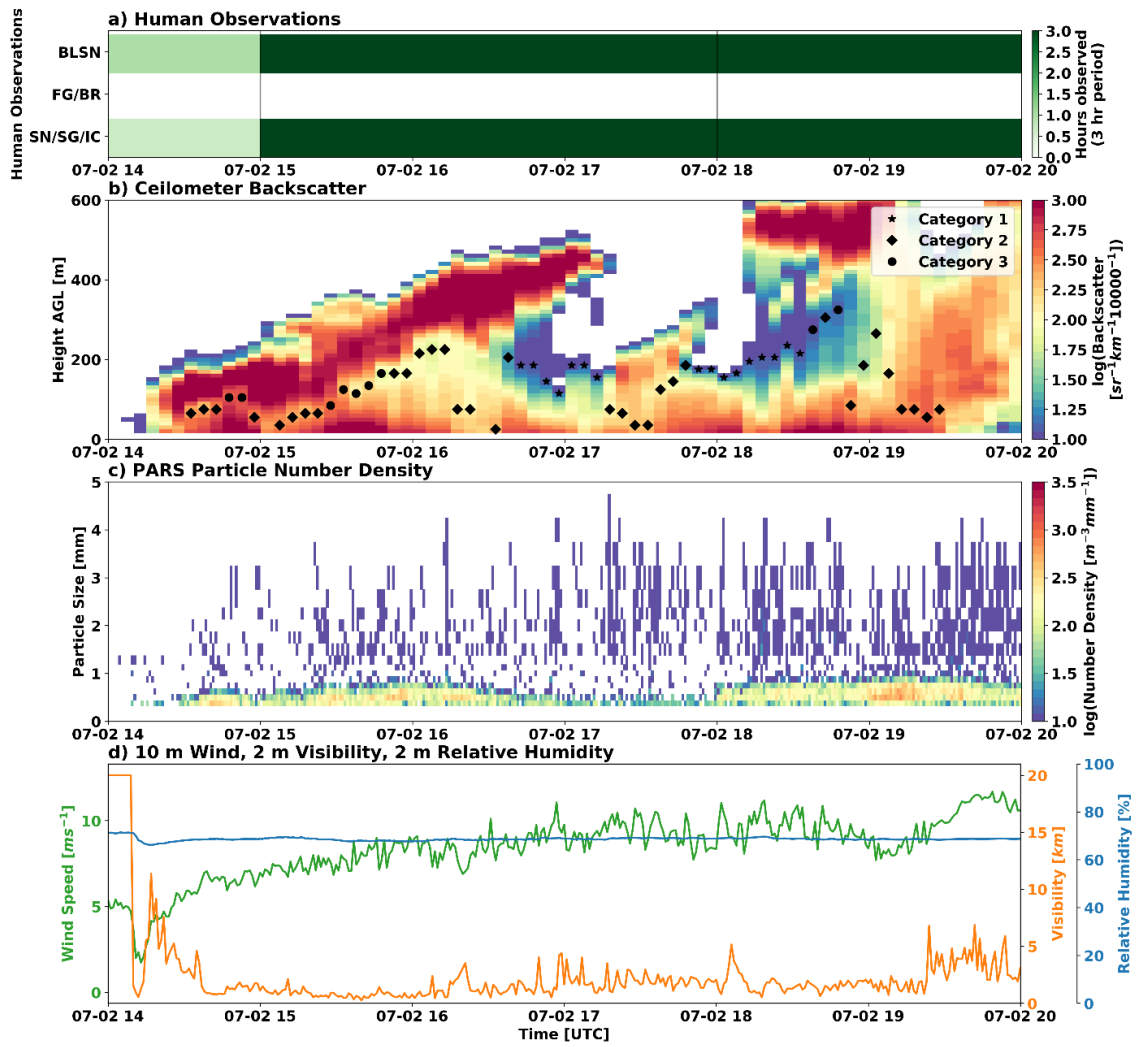


Figure 27. As in Figure 25, but for 2 July 2016.

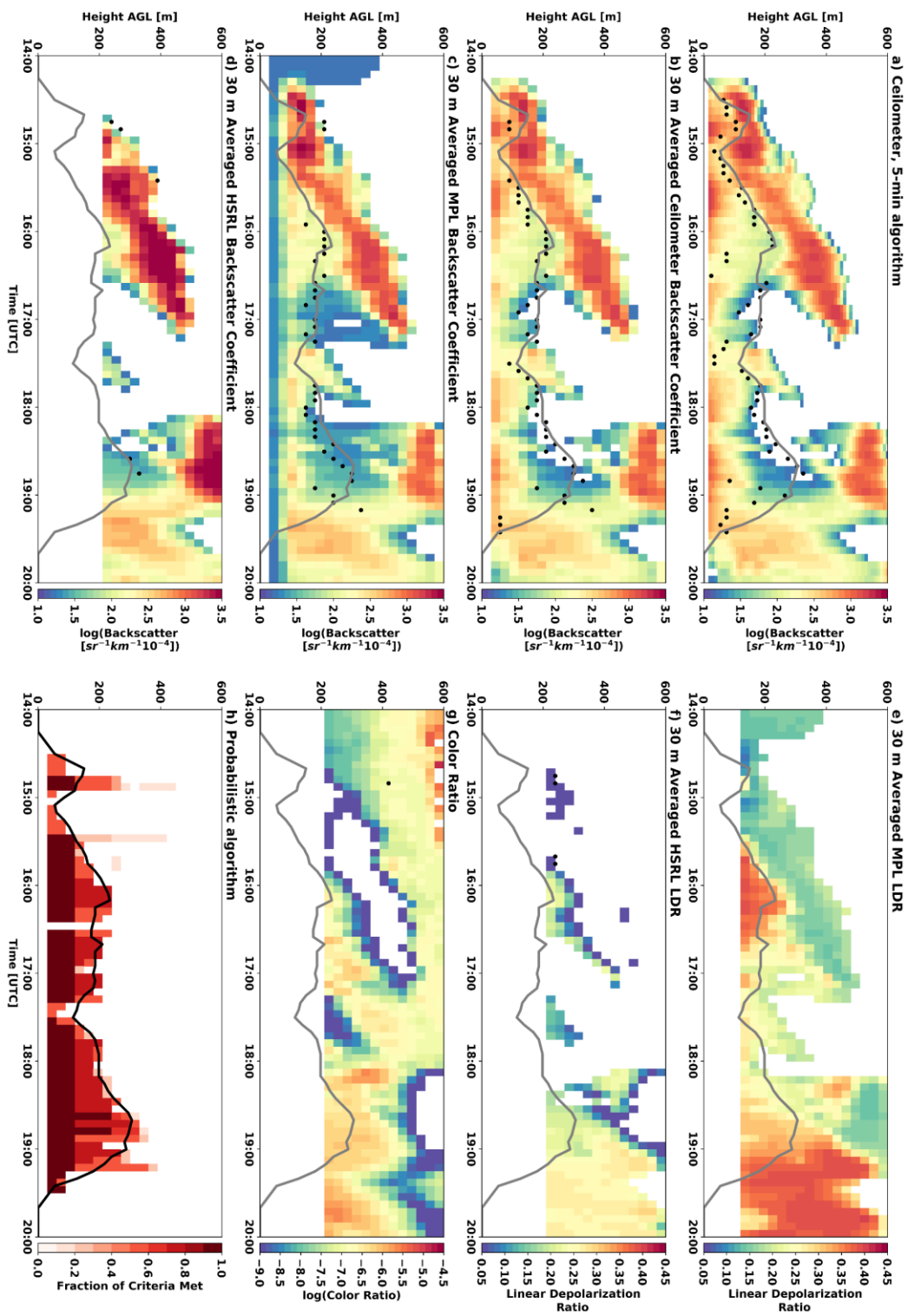


Figure 28. As in Figure 26, but for 2 July 2016.

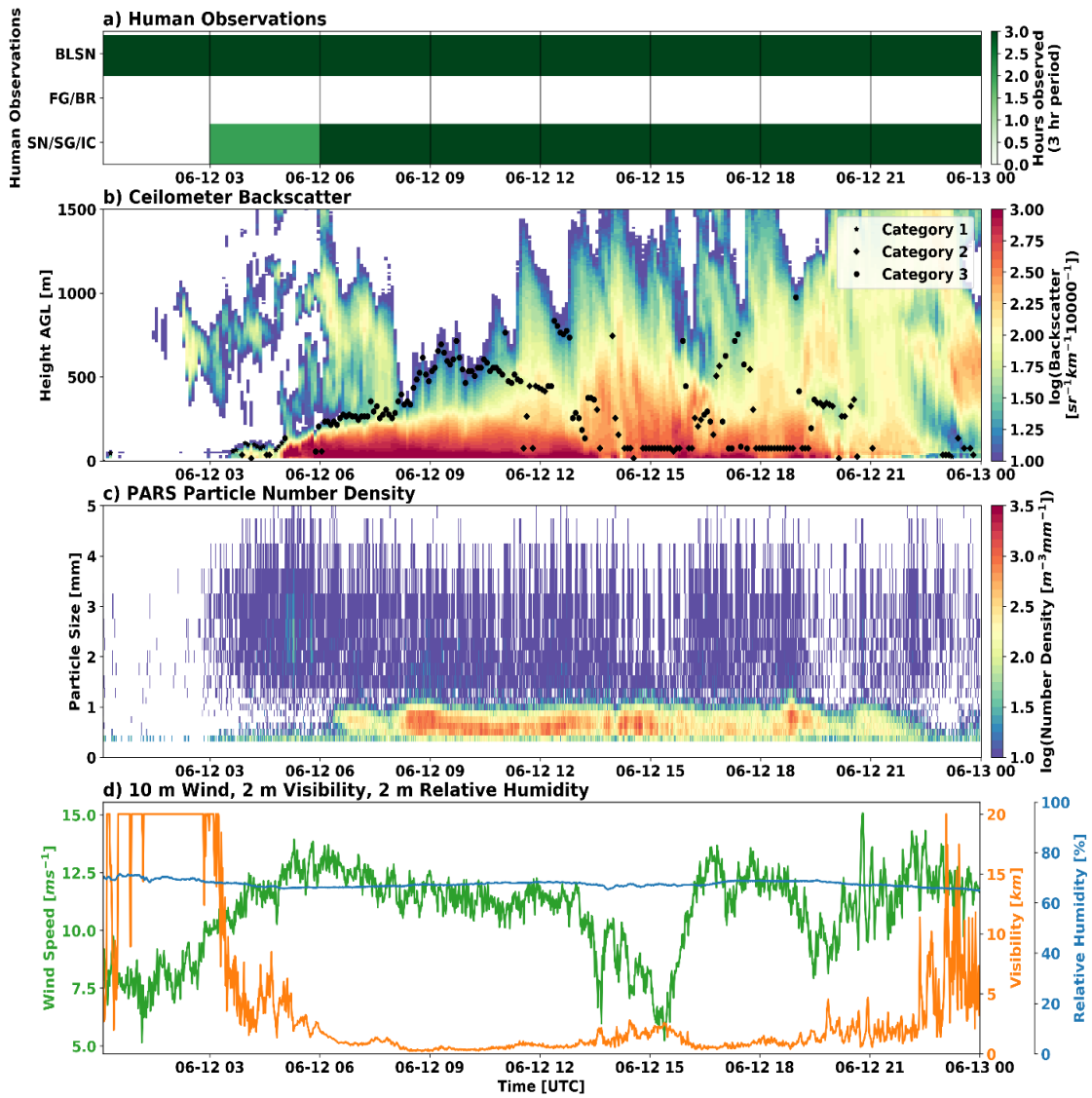


Figure 29. As in Figure 25, but for 12 June 2016.

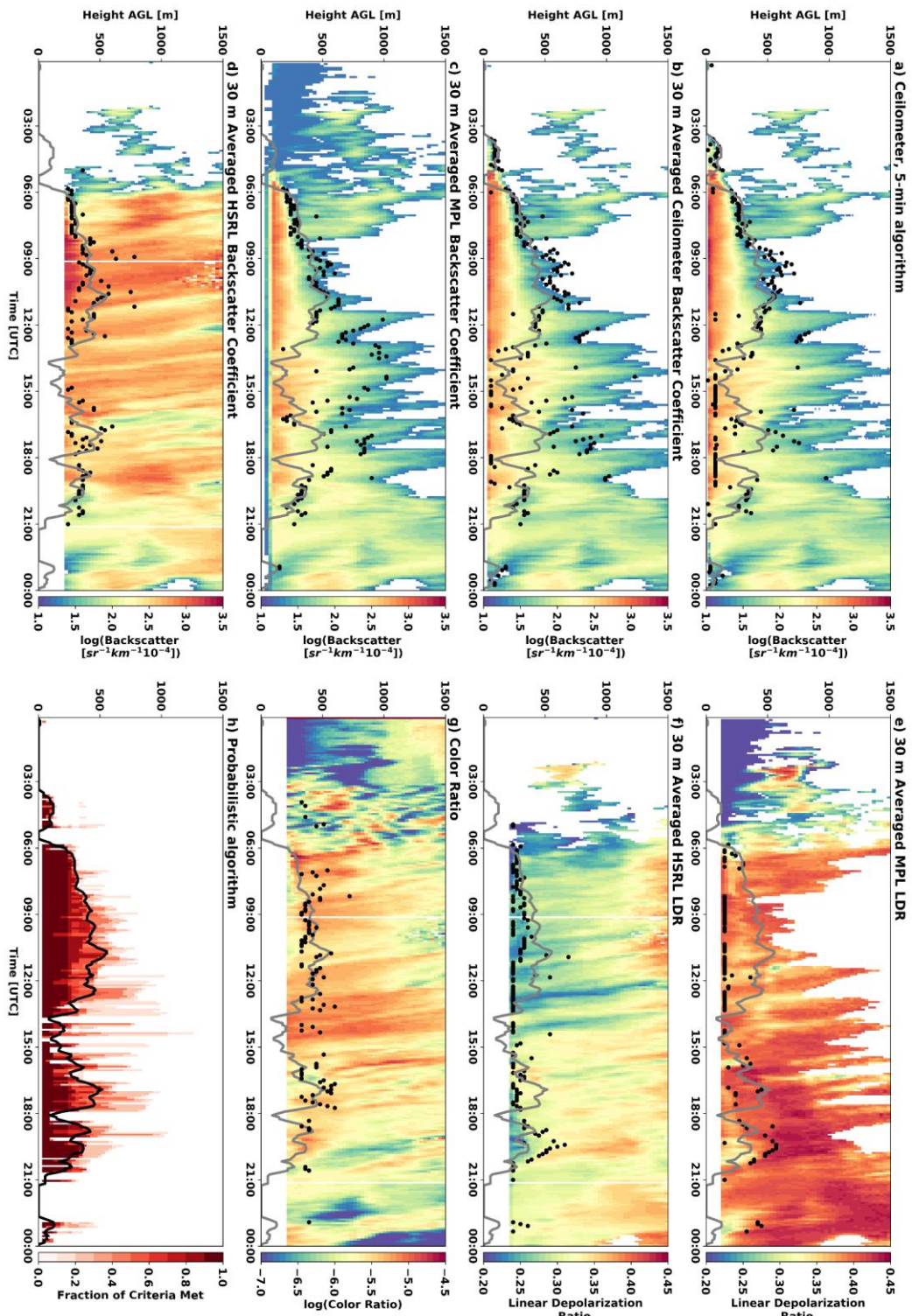


Figure 30. As in Figure 26, but for 12 June 2016.

CHAPTER 5

RESULTS AND DISCUSSION

5.1. Human-Observed Climatology of Blowing Snow

From 2002 to 2018, McMurdo Station had an annual average of 806.9 hours of BLSN, yielding a frequency of 9.2% (Figure 31a). The frequency of BLSN has significant annual variability at this location with annual totals ranging from 371.0 to 1214.2 hours (4-14%). BLSN also has a defined seasonal cycle with maximum frequencies occurring during the Antarctic winter (April-October, Figure 31b). Overall, June is the climatological maximum for BLSN with an average of 118.6 hours (16.4%). Conversely, very little BLSN occurs during the summer months of December to February. For example, the December average for BLSN is only 11.3 hours (1.6%). Between these seasons, transitional periods are observed, but the greatest variability occurs at the end of the cold season (September and October).

Observations of BLSN were also examined by its occurrence with other conditions (Figure 32). The majority of all BLSN observations occurred concurrently with falling solid precipitation in all seasons, accounting for 44.5-82.2% of annual BLSN observations. This is particularly the case during summer, accounting for an average of 78% of BLSN observations. This proportion falls to 56-63% during the rest of the year, as more BLSN is observed independently of other hydrometeors.

BLSN during the AWARE Campaign was slightly below average, with an annual total of 723.5 hours (Figure 31a). Month-to-month variability was seen during the first half of the year with April and June being the most prolific months for the process; each month had ~150 hours of BLSN, easily falling outside the third quartile of the distributions.

Observations of BLSN were above average for most of the first half of the year, followed by below-normal occurrence in the late winter and spring, with only 2.7 BLSN hours reported in November (Figure 31b).

5.2. Blowing Snow Detection Algorithm Results

5.2.1. Comparison to Human Observations

Monthly BLSN frequencies from the algorithms are shown in Figure 33 while seasonal and total values are listed in Table 9. For comparative purposes, human observations are also provided along with the frequencies of visibility measurements < 5 km. Broadly speaking, the algorithms had similar seasonal cycles of BLSN with local maxima and minima during similar months. Of the methods analyzed, the Gossart algorithm had the highest positive bias compared to human observations with 1234.9 vs. 723.2 hours detected. In a relative sense, this difference was notably larger for the summer (DJF), with a ~500% increase over human observations. The five-minute algorithms with and without thresholds detected 679.0 and 1044.8 hours of BLSN, respectively. Overall, the five-minute algorithm most closely matched the human observations throughout the year. The only month in which human observers reported a higher occurrence of BLSN than the algorithms was in April, which was also the peak month for these observations during the AWARE campaign.

Separation of BLSN events by category shed additional light on the process at McMurdo Station (Figure 34). All algorithms detected a higher frequency of intense mixed events (Category 3) than other categories. This means BLSN is closely tied to ongoing precipitation events at this location. Seasonally, this is most common during the autumn and early winter (March to June). Once snow accumulates, clear sky BLSN becomes more

likely until peaking in August. At this point, warming conditions reduce the likelihood of BLSN, and frequencies drop for all categories into the summer.

The impacts of time averaging can be identified by comparing results between the Gossart and the no thresholds algorithms. Over the course of the year, the alteration of temporal averaging alone led to a decrease of BLSN detection from 1234.9 to 1044.8 hours (a 2.2% absolute reduction in frequency). The difference between these two methods varied month-to-month shedding more light on temporal variability in the ceilometer backscatter coefficient. These differences were largest during April, July, and August suggesting BLSN occurrence had spatial heterogeneity, such as what has been seen at other locations (Scarchilli et al. 2010; Kennedy and Jones 2020). Manual inspection of ceilometer data supports this conclusion, but unfortunately, this time of year did not allow for the analysis of passively-sensed satellite data as there was insufficient solar radiation to support the detection of BLSN with near-infrared bands (Palm et al. 2011; Kennedy and Jones 2020).

The final point of discussion is the impact of wind speed, visibility, and RH thresholds. As this can be considered a quality-control process that helps confirm BLSN is occurring, detected BLSN frequency is decreased year-round (Figure 33). In total, 679.0 hours were detected by the five-minute algorithm (absolute frequency of 7.8%), slightly below the results for human observations. While there is good agreement for the entire campaign, inspection of individual months revealed some differences. During the month of April, the 5-min algorithm had ~30% less hours of BLSN than the original Gossart algorithm and human observations. Half of this difference can be explained by the lack of temporal averaging. In this case, five-minute averages appeared to better handle artifacts in the lower

bins of the ceilometer profiles. The remainder was removed due to the wind speed threshold not being met. Finally, it is worth mentioning April had the highest number of hours of observed falling snow, so complicated backscatter coefficient profiles were commonplace. This led to cases where BLSN was observed but not detected by any algorithm. As a result, it is probable even the original Gossart algorithm is biased low (compared to other months).

The other major difference caused by the inclusion of thresholds occurred during the summer months. The five-minute algorithm performed notably better during this season due to the removal of fog cases. The most important contributor to this reduction was the inclusion of the RH threshold. While imperfect (manual inspection of data noted missed cases in November), the chosen value (90%) prevented wintertime BLSN cases from being removed. Overall, it is concluded that the other algorithms are biased high by at least 5% from November to January (Figure 34).

Agreement between the algorithms and human observations varied seasonally (Figure 35). The average monthly PC for the Gossart algorithm was 76.5%, agreeing with the results of Gossart et al. (2017), but was only 62% during July. The five-minute algorithm has the highest PC in all months, while the Gossart algorithm has the lowest, meaning that the included wind speed, visibility, and RH thresholds are essential to remove cases that cannot be associated with BLSN. The PC is highest for all algorithms during the summer months (DJF). This is expected due to the lower frequency of BLSN allowing for correct null detections to dominate the statistic. Although various shortcomings in the human observations have been identified, the high agreement between the five-minute algorithm, along with meteorological variables suggesting the presence of BLSN rather than backscatter coefficient alone, help to increase confidence in algorithm results.

Another factor affecting the seasonality of the agreement is shortcomings of the human observations, rather than failings of the algorithm. Human observations are inherently subjective; what one observer may denote as BLSN, another may not. The record is expected to be biased towards longer periods of BLSN, as the observer only records the number of hours of occurrence of a phenomena within a three-hour period. It is likely that short-lived BLSN plumes may be missed, leading to discrepancies between the algorithm and the human.

Based on the algorithm results and human observations, it is estimated that the frequency of BLSN during AWARE was 7.7-12.0% including the analysis from the algorithms and the human observations. Extrapolating these values to the range of frequencies based on human observations, the annual range of BLSN frequency is estimated to be 3.5-21.3% at McMurdo Station. Overall, the detection of BLSN by the algorithm is considered to perform quite well, but considerable uncertainty is associated with the detected depth of the BLSN layer, particularly during intense mixed events.

5.2.2. Sensitivity Testing

The five-minute algorithm results can be impacted by the selected clear sky backscatter coefficient and wind speed, visibility, and RH thresholds. The values selected to assess the impact of the clear sky threshold profile were the 90th, 98th, and 99th percentile compared to the value used in the algorithm (95th percentile). The resulting frequencies are shown in Table 10, along with the value of the backscatter coefficient in the lowest usable bin for each tested percentile. The backscatter coefficient varied from 8.6 to 205.8 sr⁻¹km⁻¹ 10⁻⁴, but the frequency of detected BLSN did not vary as drastically. When the 90th percentile clear sky profile was used, BLSN detection increased slightly to 102.1% of the

amount detected when the 95th percentile was used. On the other hand, the value of the 99th percentile backscatter coefficient was approximately 10 times as high as that of the 95th percentile, but only reduced the amount of BLSN detected by 17%. The range of absolute frequencies detected was only 1.5%, showing that the clear sky threshold used did not have a substantial impact on the detection of BLSN using this methodology.

The selected meteorological thresholds were also varied to identify their impact on BLSN detection. For this sensitivity study, individual values were altered as other thresholds were held constant. The results of varying the wind speed threshold are shown in Table 11. This threshold was tested in 2 ms⁻¹ increments. The temperature-dependent BLSN initiation wind speed threshold relationship derived in Li and Pomeroy (1997b) was also tested. This relationship is given by the following equation:

$$U_t = a + bT + cT^2 \quad (5)$$

where U_t represents the threshold wind speed at 10 m elevation, T represents temperature, and a, b, and c, are empirical parameters; $a = 9.43 \text{ m s}^{-1}$, $b = 0.18 \text{ m s}^{-1} \text{ }^\circ\text{C}^{-1}$, and $c = 0.0033 \text{ m s}^{-1} \text{ }^\circ\text{C}^{-2}$. Like the clear sky threshold, the tested wind speed thresholds do not impact BLSN substantially. The lowest wind speed tested, 1 m s⁻¹, yielded a 9.5% increase in detection over the five-minute algorithm, while tripling the threshold (9 m s⁻¹) reduced the amount of BLSN detected by 21.4%. The absolute frequency of BLSN using the empirical relationship derived by Li and Pomeroy (1997b) only differed from the five-minute algorithm by 1%. Since the Li and Pomeroy (1997b) relationship was derived in the Canadian Arctic, it may not accurately represent the relationship between BLSN occurrence and wind speed in Antarctica. It is anticipated that BLSN can occur at lower wind speeds in the Antarctic, therefore a lower wind speed threshold of 3 m s⁻¹ is deemed appropriate for this study. The visibility threshold was varied in increments of 2 km (

Table 12). The results of these tests are similar to that of the wind speed threshold, with the overall detected BLSN remaining largely unchanged. Absolute frequencies of detected BLSN ranged from 6.8-8.0% using thresholds of 4-14 km.

Rather than impacting the total number of hours detected as potential BLSN by the algorithm, varying the RH threshold impacted the amount of the detected hours that were designated as fog. Figure 36 shows the proportion of each category detected when the RH threshold is varied from 70-95%. It is apparent that a 95% RH threshold did not sufficiently remove cases of fog during the summer months, and that 70-85% thresholds denoted profiles as fog during the winter months, causing the difference between the algorithm's BLSN detection and hours of occurrence from human observations to increase. Based on these results and manual inspection of daily observations, a RH threshold of 90% was deemed the most appropriate for separation of BLSN and fog cases.

5.2.3. Fog

Previous BLSN detection algorithms did not account for fog, leading to a positive bias in the occurrence of BLSN when compared with human observations. Lazzara (2008) presented a climatology of fog at McMurdo Station and found that fog occurrence peaks in January and September. It was noted that the majority of fog observed at McMurdo Station in the austral summer is advected from the Ross Ice Shelf or the northern Scott Coast of McMurdo Sound. Advective fog would not be removed with a wind speed threshold alone; agreement between the algorithm BLSN detection and human observations increases when a RH threshold is used to separate fog from BLSN. The five-minute algorithm (Figure 36b) does not detect any fog during austral spring associated with the climatological fog peak in September, but the methodology used here aims to distinguish periods of BLSN from fog,

rather than to detect all fog periods. Based on the presented analysis, the RH threshold is a simple, effective way to distinguish periods of advective fog from BLSN. The selected RH threshold performs appropriately for this dataset, but it should be investigated before applying the presented BLSN detection algorithm to different locations.

5.2.4. Parsivel² Particle Observations

Although the Parsivel² is only sensitive to particles 250 μm and greater, it was hypothesized the instrument could provide enough information about the large tail of the BLSN particle size distribution (e.g. Mellor 1965; Nishimura and Nemoto 2005; Gordon and Taylor 2009), to distinguish between the categories of BLSN, falling snow, and fog. Distributions and mean particle counts were computed for the various categories (Figure 37).

Mean particle counts are lowest (highest) for Category 1 (3) events while fog has significant overlap with all categories. The mean particle size distributions for each category are shown in Figure 37b. For all categories, the peak occurred at particle sizes of 0.3-0.5 mm. Fog events have the highest peak particle number density, along with considerable variation in mean particle counts. Category 3 events had a greater quantity of larger diameter particles which would be expected with intense mixed events including falling snow. Overall, Parsivel² particle counts and number densities alone do not appear to aid in separating scenes of hydrometeors.

Since characteristics and limitations of the Parsivel² have been documented for falling snow (Battaglia et al. 2010) but minimally for BLSN, further investigation was warranted. Given the importance of wind for the process, Parsivel² observations during time periods of detected BLSN were segregated into 2 m s^{-1} wind speed increments, shown in Figure

38a. It is evident that at approximately 10 m s^{-1} , the particle concentrations become significantly higher at sizes above 1 mm and lower in the smallest size bins. This pattern continues to particle sizes much larger than expected in BLSN or falling snow. This effect is expected to be due to sampling issues with the instrument at high wind speeds, as suggested by Friedrich et al. (2013). As wind speed increases particles may overlap, leading to incorrectly large particles being detected.

Data from other locations in which a Parsivel² was deployed during BLSN were analyzed to assess whether this effect was present in other observations from the instrument, shown in Figure 38b-c. The Phoenix Airfield Antarctica Precipitation Site (APS) refers to an observation site located near the Phoenix Airfield in McMurdo Station. Observations were available for BLSN event days in 2018 and 2019. It should be noted that the Parsivel² deployed at the Phoenix Airfield was deployed at a 45° angle to the surface, therefore results are expected to be different than those from the AMF2. The final dataset was retrieved from a Parsivel² deployed near Grand Forks, North Dakota during the 2020 Blowing Snow Observations at the University of North Dakota: Education through Research (BLOWN-UNDER) Field Campaign. While data from these periods cannot be verified to be associated with BLSN through the presented ceilometer-based algorithms, it provides a gross comparison to other observations at the same wind speeds. The Phoenix APS distributions showed the same drop in small particles ($< 0.5 \text{ mm}$) as seen in the observations from the AWARE Campaign, though the differences at the largest particle sizes were less clear. The BLOWN-UNDER observations showed evidence of the same effect of wind speeds on the concentration of large particles ($> 3 \text{ mm}$). This artifact was present to a varying extent in all datasets analyzed, suggesting that the issue is most likely

a fundamental limitation of the Parsivel². It is currently hypothesized that high number concentrations of BLSN may contribute to separate particles creating voltage signals indicative of singular particles with a greater diameter than reality. As a result, it is concluded Parsivel² observations should be used with caution during periods of wind greater than 10 m s⁻¹.

5.3. Probabilistic Blowing Snow Algorithm Results

5.3.1. Criteria Analysis

The amount of time that the criteria for each algorithm, as described in Section 3.5, are met for all of 2016 is shown in Figure 39a. Since the MPL, HSRL, and color CR algorithms were only valid when BLSN was deep or an intense mixed event occurred, the monthly frequency of validity for each algorithm is also provided for periods designated as Category 3 (Figure 39b). Table 13 shows the seasonal and total number of hours each criterion is met during BLSN periods and the proportion of five-minute algorithm detections that meet the criteria for each algorithm. The requirements for the backscatter algorithms was met more commonly than the others, particularly the 30 m CEIL and MPL BS algorithms. Backscatter is the fundamental variable to use to observe BLSN in simple Category 1 and 2 cases, while CR and LDR are typically most useful during more complex events. The criteria for the MPL LDR and CR algorithms were met the most infrequently, being met during only 17.9 and 30.8% of five-minute algorithm BLSN detection periods, respectively. While these values are relatively low, it is not expected to negatively impact the probabilistic BLSN detection since each of these algorithms only act to supplement one another, rather than requiring all algorithms to be valid to detect BLSN.

5.3.2. Probabilistic Blowing Snow Depth

The average depth of the detected BLSN during the 41 days analyzed was 218.3 m. Figure 40 shows the mean depth during each month of 2016, along with the number of cases investigated. June and October saw the highest mean detected BLSN depths, though October had only one case day. The deepest detected plume reached 678 m, recorded on 25 June 2016, associated with Category 3 BLSN. The monthly average depth ranged from 185.2 to 253.3 m and was generally higher during the winter and autumn months. Boxplots of the distribution of heights detected by the probabilistic and five-minute algorithms are shown in Figure 41. The distribution of depths detected by the probabilistic algorithms approximates a normal distribution with slight positive skewness, while the five-minute algorithm depths were more variable. The selected cases represent higher end events; therefore, the overall depth of BLSN at McMurdo Station likely contains more shallow plumes.

To investigate the impact of using the probabilistic approach, the distribution of depths detected by the probabilistic algorithm was compared to that of the five-minute algorithm (Figure 41-Figure 42). The distribution of BLSN depths from the five-minute algorithm, shown in Figure 42a, shows that approximately 41% of all detected plumes were <100 m deep. Mahesh et al. (2003) noted that approximately 50% of sampled BLSN layers were less than 200 m deep, and similar results were found by Gossart et al. (2017), although both studies hypothesized that the depth of mixed events were underestimated due to attenuation issues. While some of these shallow estimations are likely accurate, it also may suggest that 50-100 m is a height where the algorithm commonly failed due to noise in the profiles. This bin includes the region where the ceilometer is noted to have common laser

overlap issues leading to increased artifacts in backscatter coefficient retrievals (Gossart et al. 2017).

The distribution of differences between the two algorithms in individual detections is shown in Figure 43. It is evident that during the majority of observation periods, the two depths are within ~100 m, but periods exist when there are larger differences. Figure 44 shows two-dimensional histograms of probabilistic versus five-minute algorithm depth estimations by category to help highlight the relationship between the two algorithms. Category 1 events approximate a one-to-one relationship, suggesting that the five-minute algorithm performed adequately during clear sky events. The depths of Category 2 events tended to be underestimated by the five-minute algorithm, with the majority of these periods seeing higher BLSN depths estimated by the probabilistic algorithm. Finally, intense mixed events (Category 3) saw the most substantial differences. Based on Figure 44c, the probabilistic algorithm acted to regulate the depths suggested by the five-minute algorithm; generally, deep plumes (> 400 m) were made shallower and shallow depths (< 300 m) were increased.

The mean depth of BLSN detected for each category by both the probabilistic and five-minute algorithms, along with the average absolute difference between the two, are shown in Table 14. The average depth for Category 1 and 2 events was highest for the probabilistic algorithm, with the largest difference between means for the Category 2 events. However, the largest absolute difference in depth estimations was in intense mixed events (Category 3), which was found to be 97.6 m. The differences in heights during intense mixed events ranged from -801.0 m, where the five-minute algorithm detected a depth of 1005.0 m while the probabilistic algorithm estimated only 204.0 m, to +465.0 m,

when the probabilistic algorithm estimated a depth of 498.0 m compared to 75.0 m given by the five-minute algorithm. Category 1 saw the shallowest BLSN layers which, on average, were approximately 147.1 m shallower than that of Category 3 based on the probabilistic algorithm.

To evaluate the impact that each of the additional contributing algorithms had on the probabilistic BLSN depth, two-dimensional histograms comparing the top of the BLSN layer designated by each algorithm to the final probabilistic BLSN depth are shown in Figure 45. The probabilistic depth is most closely related to the results of the 30 m CEIL and MPL BS algorithms, based on their histograms (Figure 45a-b) approximating a one-to-one relationship more so than that of the other algorithms. It follows logic that the 30 m CEIL algorithm was important in overall results of the probabilistic algorithm, as it was the only one that was performed during all BLSN periods detected by the five-minute algorithm (the others have depth/category requirements, as explained in Table 8). The results of the LDR and CR algorithms appear to be less closely tied to the probabilistic BLSN depth than those that are based on backscatter coefficient. These algorithms appear to have a bin with very high variance in the histogram, where a variety of probabilistic BLSN depths are detected when the individual algorithm only reached the lowest usable bin for said instrument (e.g. Figure 45d-f). This suggests that these individual algorithms may have failed in the first bin of analysis due to artifacts/noise in the observations. This effect was seen to a lesser extent in the 30 m CEIL results. Additionally, the LDR and CR algorithms are more experimental than those based on backscatter coefficient, so it is expected that they provide guidance to distinguish falling and BLSN for the final depth estimation and may not be valid for many cases. In summary, a benefit of using the probabilistic approach

to estimate the layer's depth is that it better defined the overall patterns associated with BLSN and the noise that can cause any one algorithm to err may be overcome by the others.

5.3.3. Sensitivity Testing

The 23 sensitivity tests applied in the analysis of the probabilistic algorithm are listed in

Table 15. These tests were selected such that any assigned thresholds or subjectively selected values in all of the algorithms, including the final probabilistic depth detection algorithm, were examined to determine the impact they had on the final results.

The results of the sensitivity testing applied to the CEIL 30 m, MPL BS, and HSRL BS algorithms are presented in Figure 46-Figure 48, respectively. It is evident that varying the clear sky percentile used did not substantially change the distribution of detected depths of the algorithms. The use of the 98th percentile shifted the distribution of depths detected by both the CEIL 30 m and MPL BS algorithms towards slightly lower values, but the median values remained comparable to that of the 95th percentile threshold.

Seven tests were applied to the two LDR algorithms, shown in Figure 49 and Figure 50. The median value for all tests performed on both algorithms was the lowest usable bin (150 m for MPL LDR and 240 m for HSRL LDR). This suggests that the algorithms may be detecting the presence of BLSN but are unable to continue profile analysis past the first usable bin. These algorithms are only developed with the goal of aiding BLSN characterization when the plume is sufficiently deep, particularly during precipitation events. Because of this, they are not expected to be adequate to provide useful information for all BLSN plumes. Further study is necessary to develop more in-depth profile analysis routines to provide more insight into a higher proportion of the detected BLSN. The MPL LDR algorithm saw the most dramatic reduction in spread when the 98th percentile MPL

clear sky threshold profile was used rather than the 95th but did not see marked changes with the rest of the performed sensitivity tests. On the other hand, the HSRL LDR algorithm saw larger changes than the MPL LDR algorithm for some of the tests with the most notable differences arising when the averaging layer for LDR profile analysis was changed to 90 or 300 m. Additionally, the median value for both of the LDR algorithms was the lowest usable bin. This may suggest that the LDR algorithms need finer tuning in the future, though the analysis presented here does help to prove the usefulness in incorporating these observations in future work.

The CR algorithm was impacted by eight of the sensitivity tests listed in

Table 15. The resulting distributions are shown in Figure 51. The tests that altered the distribution of heights detected by the CR algorithm the most incorporated all categories of detected BLSN, using three bin vertical averaging in profile analysis (rather than two) and increasing the minimum threshold from 10^{-8} to 10^{-7} . Most of the tests shifted the distributions towards shallower depths, though the most substantial changes were associated with incorporating all BLSN categories. This test reduced the interquartile range of the distribution noticeably, likely due to the fact that the algorithm was run even if the detected plume was much shallower than the required depth to be seen by the HSRL and KAZR. This led to a higher number of detections in the lowest usable bin for the CR algorithm.

Finally, the distributions of probabilistic BLSN depths that resulted from each of the 23 sensitivity tests are shown in Figure 52. Changing the proportion of criteria to be met for a bin to be designated as BLSN led to the most substantial impacts on final detected BLSN depths. Increasing the required percentage from 50% to 60% or 70% reduced the

spread of detected BLSN depths, shifting towards shallower depths. This effect was reversed when the proportion was decreased to 30% or 40%. Increasing the ceilometer or MPL clear sky percentile to 98 also acted to shift the distribution towards shallower plumes, but not as noticeably as when the percentage of criteria required was increased. Additionally, the use of no smoothing led to the widest interquartile range. This is because, without smoothing, the heights detected can change drastically between consecutive five-minute periods which allows for depth variations that are very physically unlikely. Overall, the probabilistic BLSN depth distribution remained relatively consistent during the sensitivity testing; the median and mean of the distribution remained within 20 m of the value found for the final probabilistic algorithm during all of the performed tests.

5.4. Environmental Properties of Blowing Snow

Surface weather conditions are often the deciding factor in the occurrence of BLSN, since sufficient wind is required to initiate the process. Previous studies have attempted to quantify relationships between BLSN occurrence and environmental properties (e.g. Li and Pomeroy 1997) but these associations are still poorly constrained and vary by location.

5.4.1. Blowing Snow Occurrence by Meteorological Variables

To investigate the relationship between meteorological properties and BLSN occurrence, two-dimensional histograms were produced (Figure 53). First, the relationship between detections and visibility and wind speed is investigated (Figure 53a). The majority of detections of BLSN occurred with 10 m wind speeds of 7.5-12.5 ms^{-1} and 2 m visibility of less than 2 km. Observations of very high wind speeds were uncommon, therefore there were few BLSN detections above $\sim 17.5 \text{ ms}^{-1}$. Overall, it appears that low to moderate wind speeds (3-12.5 ms^{-1}) were associated with variable visibility observations (0-10 km), while

BLSN with higher wind speeds tended to occur with visibility < 4 km. Figure 53b shows the connection observed between wind speed and temperature, to compare to the threshold wind speed relationship defined by Li and Pomeroy (1997b). As discussed in Section 4.2.2, this relationship (given by Equation 5) is likely higher than would be expected in the Antarctic but can be used for general comparison purposes. Most of the detected BLSN occurred at wind speeds exceeding the expected threshold wind speed, but 27% occurred associated with lower wind speeds. In addition to the differences between the Arctic and Antarctic climate, some of these lower wind speed BLSN observations may have been associated with periods in which BLSN had already been initiated before the wind speed decreased. Figure 54 shows the likelihood of BLSN sorted by wind speed and temperature observations. All bins with that had detected BLSN over 40% of the time were found in bins that exceeded the Li and Pomeroy (1997b) threshold wind speed.

BLSN occurrence by wind direction must also be considered when evaluating the process in the region. The most frequent wind direction observed at McMurdo Station during AWARE was northeasterly, as shown in Figure 55a. This is likely due to topographic effects, as the Ross Sea is bounded by the Transantarctic Mountains to the west and south, with Mount Erebus to the north of McMurdo Station (Costanza et al. 2016). Over half of all wind observations during 2016 were from the northeasterly quadrant. This is also the most common wind direction for all BLSN categories due to its frequent occurrence, shown in Figure 55b-d. Fog detections were found at similar wind directions to that of category 1 (not shown).

Although southerly winds were relatively uncommon at McMurdo Station, they were associated with detected BLSN a higher proportion of the time. This is particularly true for

intense mixed events; over 10% of wind observations coming from 170-190° were associated with category 3 BLSN. This pattern is evident in the other BLSN categories to a lesser degree. Strong wind events ($> 15 \text{ ms}^{-1}$) observed at McMurdo Station most often are associated with southerly winds associated with a deep low pressure system approaching the region from the north (Seefeldt et al. 2003; Weber et al. 2016), meaning that it may be more likely to see more significant BLSN events during the occurrence of these southerly winds.

5.4.2. Connections Between Blowing Snow Depth and Meteorological Variables

To examine relationships between meteorological variables and the BLSN depth estimated by the probabilistic algorithm, two-dimensional histograms were produced (Figure 56). First, the relationship between BLSN depth and the observed 10 m wind speed is investigated. In this study, the deepest plumes occurred at wind speeds near 10.0 m s^{-1} , rather than with the highest observed speeds, suggesting no clear relationship between the two variables. While it has been hypothesized previously, no relationship between BLSN depth and wind speed was found in previous studies (Mahesh et al. 2003; Gossart et al. 2017). Further study with a larger number of cases is required to make a definitive statement on this relationship.

Figure 56b shows the probabilistic plume depth versus wind direction. The majority of BLSN assessed, including the deepest detected layers, were associated with winds from the northeast quadrant (particularly between 25-75°). This is not surprising, as Figure 55 showed that northeasterly winds were by far the most common at McMurdo Station (due to topographic effects). There was also some detected BLSN up to ~300 m in height

accompanying southerly winds (associated with strong windstorms, as discussed in Section 4.2.3).

The relationship between plume depth and 2 m visibility can be seen in Figure 56c. The deepest detected plumes were largely associated with near-zero visibility. The BLSN depth appears to fall as visibility increases. This suggests that the events that were the most intense near the surface (causing the largest reduction in visibility) were also associated with the highest BLSN depths.

Finally, no relationship appears to be present between temperature and BLSN depth, shown in Figure 56d. It can be noted that the majority of cases investigated occurred between -10 and -35°C, with the deepest plumes occurring between -20 and -30°C.

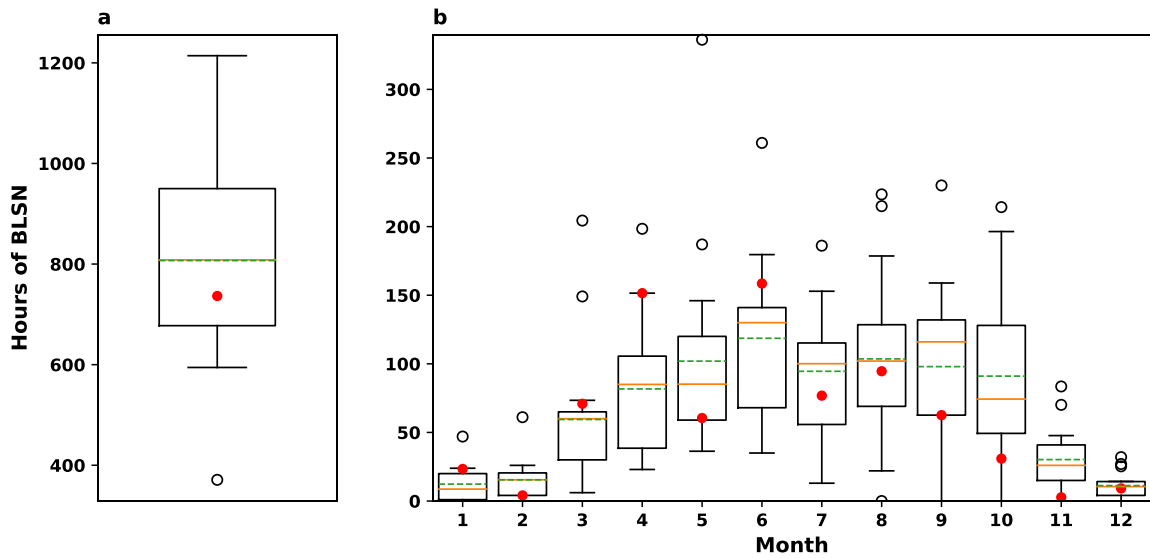


Figure 31. Boxplots of a) annual and b) monthly frequencies of BLSN from human observations at McMurdo Station, Antarctica. The box represents the interquartile range of the distribution, and the whiskers cover the minimum and maximum of the data within 1.5 times the interquartile range of the median. Observations falling outside of the whiskers (outliers) are shown as empty black circles. The orange solid and green dashed lines represent the median and mean of the distribution, respectively. Red dots show the observed frequency in 2016 during the AWARE Campaign.

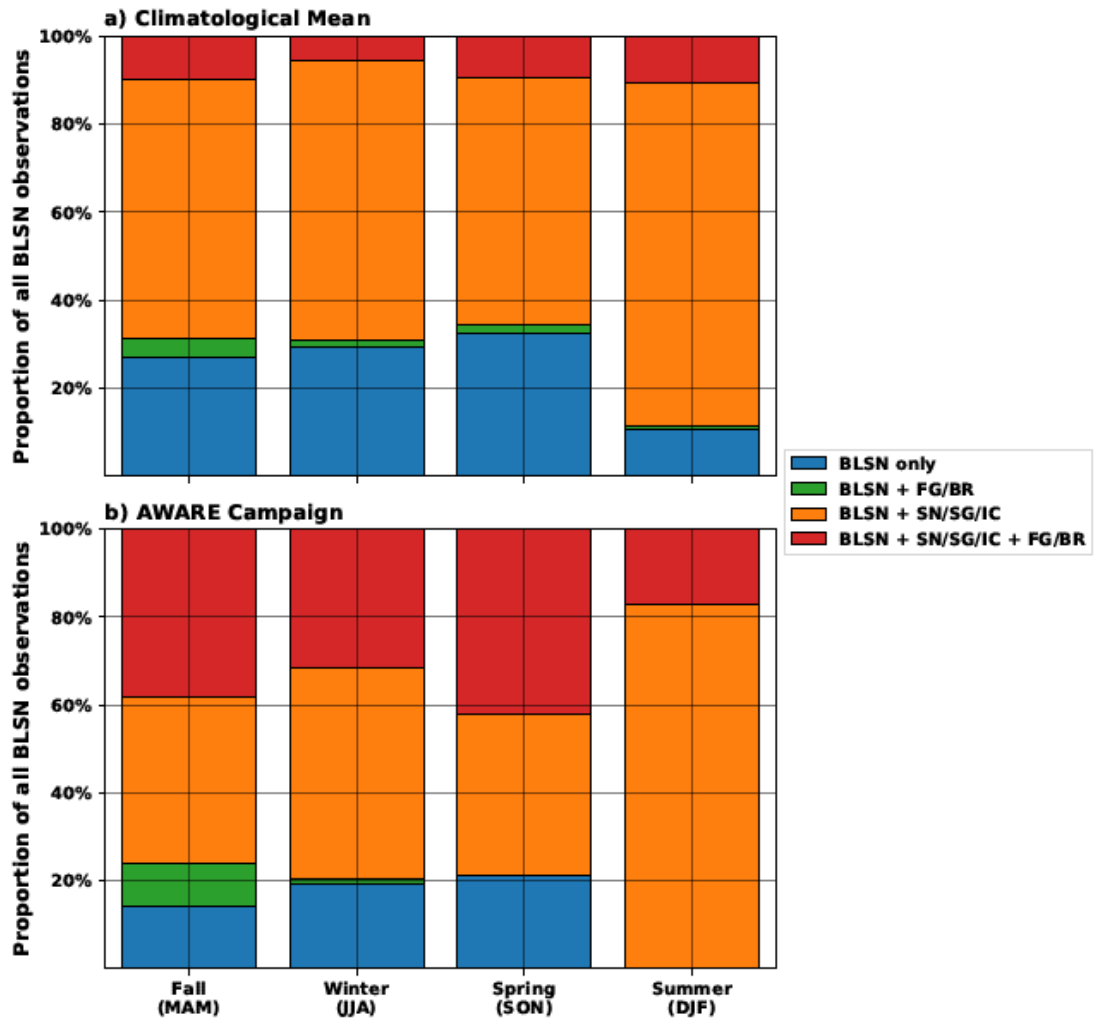


Figure 32. Seasonal proportion of human BLSN observations occurring with other phenomena at McMurdo Station. a) Climatological average for 2002 to 2018 and b) during the AWARE campaign.

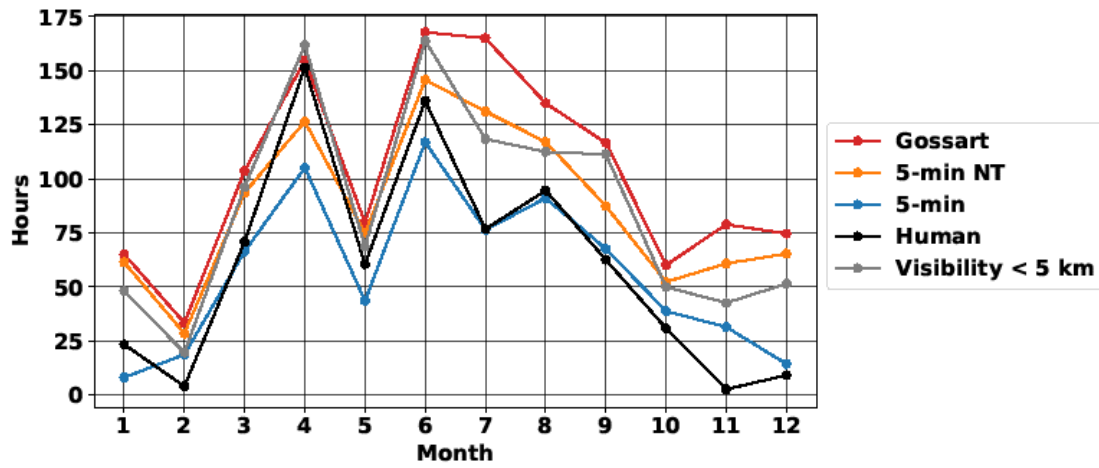


Figure 33. Monthly hours of BLSN detected by humans, ceilometer-based algorithms, and the visibility sensor during the 2016 AWARE campaign.

Table 9. Seasonal and total BLSN hours and frequencies for each algorithm shown in Figure 33.

The five-minute algorithm is further broken down into BLSN categories.

<i>Algorithm</i>	<i>BLSN Hours (Frequency)</i>				
	<i>Summer (DJF)</i>	<i>Fall (MAM)</i>	<i>Winter (JJA)</i>	<i>Spring (SON)</i>	<i>Total</i>
<i>Human</i>	36.7 (1.7%)	282.9 (12.8%)	307.4 (13.9%)	96.2 (4.4%)	723.2 (8.2%)
<i>< 5 km visibility</i>	119.3 (5.5%)	326.8 (14.8%)	394.8 (17.9%)	204.0 (9.3%)	1044.9 (11.9%)
<i>Gossart</i>	173.2 (7.9%)	338.2 (15.3%)	467.8 (21.2%)	255.7 (11.7%)	1234.9 (14.1%)
<i>5-min NT</i>	155.3 (7.1%)	294.8 (13.4%)	394.0 (17.8%)	200.6 (9.2%)	1044.8 (11.9%)
<i>5-min</i>	41.3 (1.8%)	215.3 (9.7%)	284.4 (12.9%)	138.0 (6.3%)	679.0 (7.7%)
<i>Category 1</i>	7.0 (0.3%)	24.3 (1.1%)	63.2 (2.9%)	23.2 (1.1%)	117.7 (1.3%)
<i>Category 2</i>	11.3 (0.5%)	81.8 (3.7%)	98.1 (4.4%)	43.2 (2.0%)	234.3 (2.7%)
<i>Category 3</i>	23.0 (1.1%)	109.2 (4.9%)	123.1 (5.6%)	71.7 (3.3%)	326.9 (3.7%)

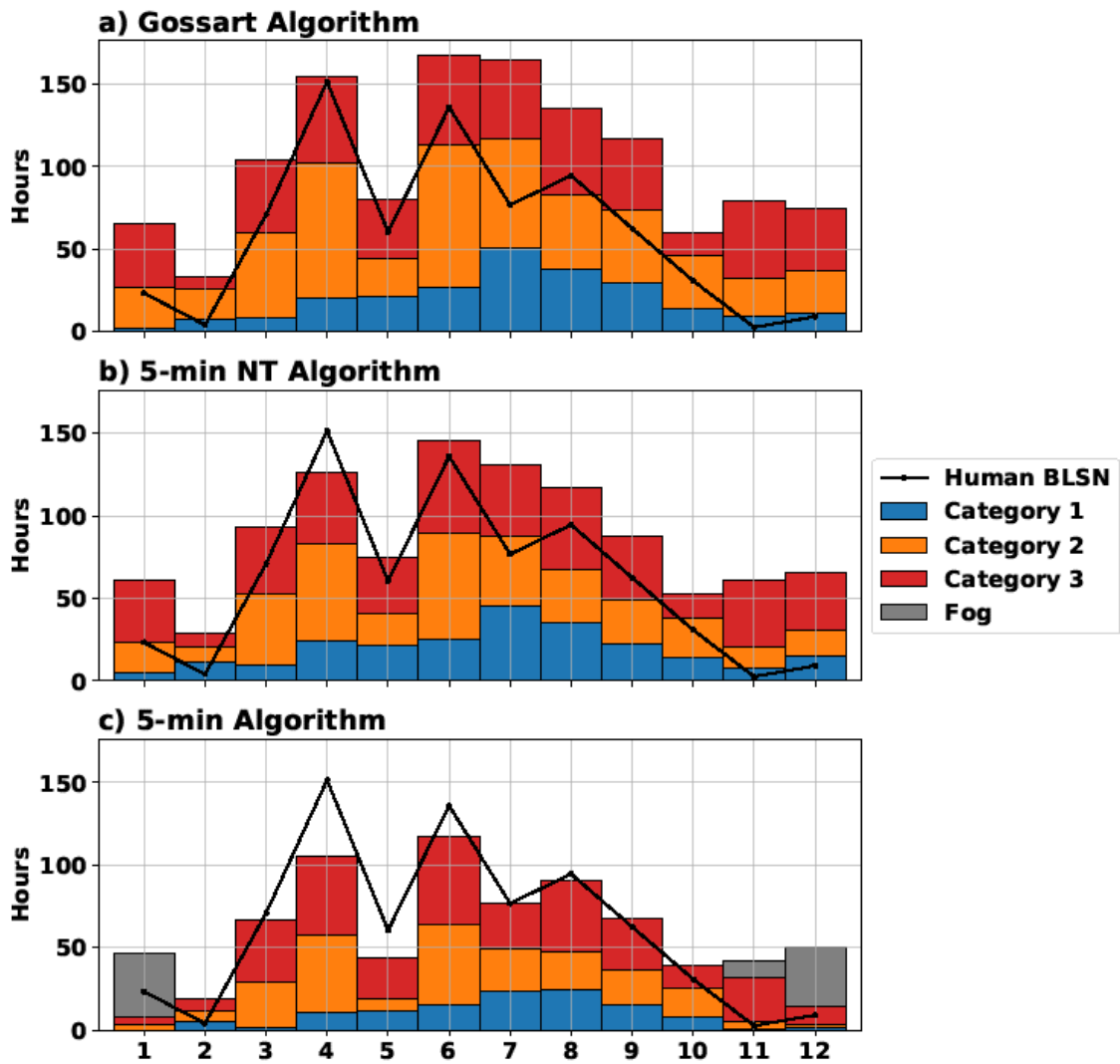


Figure 34. Monthly hours of BLSN detected by a) the Gossart algorithm, b) the 5-min NT algorithm, and c) the 5-min algorithm, divided into the category of BLSN detected. Monthly hours of human-observed BLSN are shown in black for comparison.

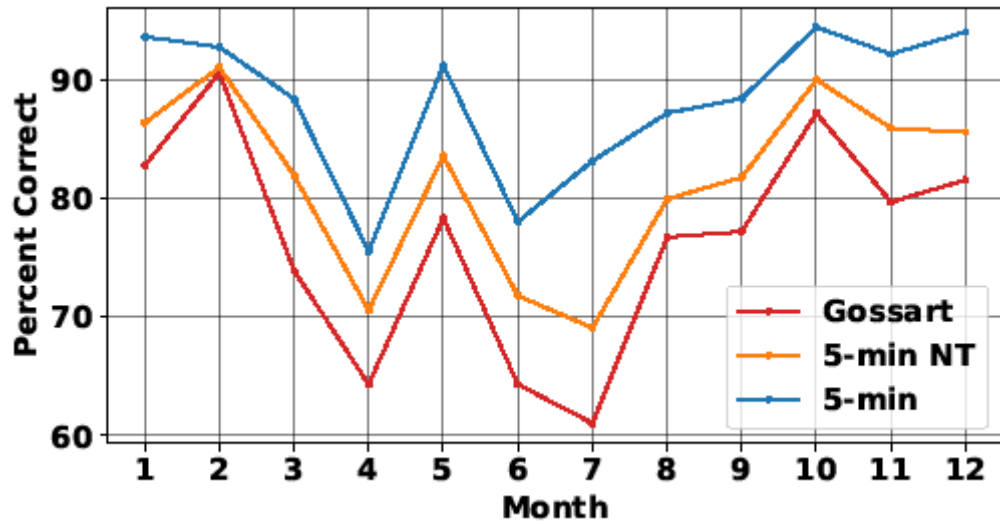


Figure 35. Percent correct by month for each algorithm during 2016.

Table 10. Impacts of clear-sky backscatter coefficient percentile on algorithm characteristics. The 95th percentile (used in the five-minute algorithm) results are included for comparison.

<i>Percentile</i>	<i>Lowest Usable Bin Backscatter Coefficient [sr⁻¹ km⁻¹ 10⁻⁴]</i>	<i>Total BLSN Hours</i>	<i>Absolute Frequency [%]</i>	<i>Percent of 5-min Detections [%]</i>
90th	8.6	693.4	7.9	102.1
95th	21.3	679.0	7.7	-
98th	79.6	607.3	6.9	89.4
99th	205.8	563.5	6.4	83.0

Table 11. As in Table 10, but for the wind speed threshold.

<i>Threshold Wind Speed [ms⁻¹]</i>	<i>Total BLSN Hours</i>	<i>Absolute Frequency [%]</i>	<i>Percent of 5-min Detections [%]</i>
5-min (3 ms ⁻¹)	679.0	7.7	
1	743.2	8.5	109.5
5	649.3	7.4	95.6
7	610.2	6.9	89.9
9	533.4	6.1	78.6
Li & Pomeroy (1997b)	585.6	6.7	86.2

Table 12. As in Table 10, but for the visibility threshold.

<i>Threshold Visibility [km]</i>	<i>Total BLSN Hours</i>	<i>Absolute Frequency [%]</i>	<i>Percent of 5-min Detections [%]</i>
5-min (10 km)	679.0	7.7	
4	600.6	6.8	88.5
6	642.5	7.3	94.6
8	663.2	7.6	97.7
12	691.5	7.9	101.8
14	703.8	8.0	103.6

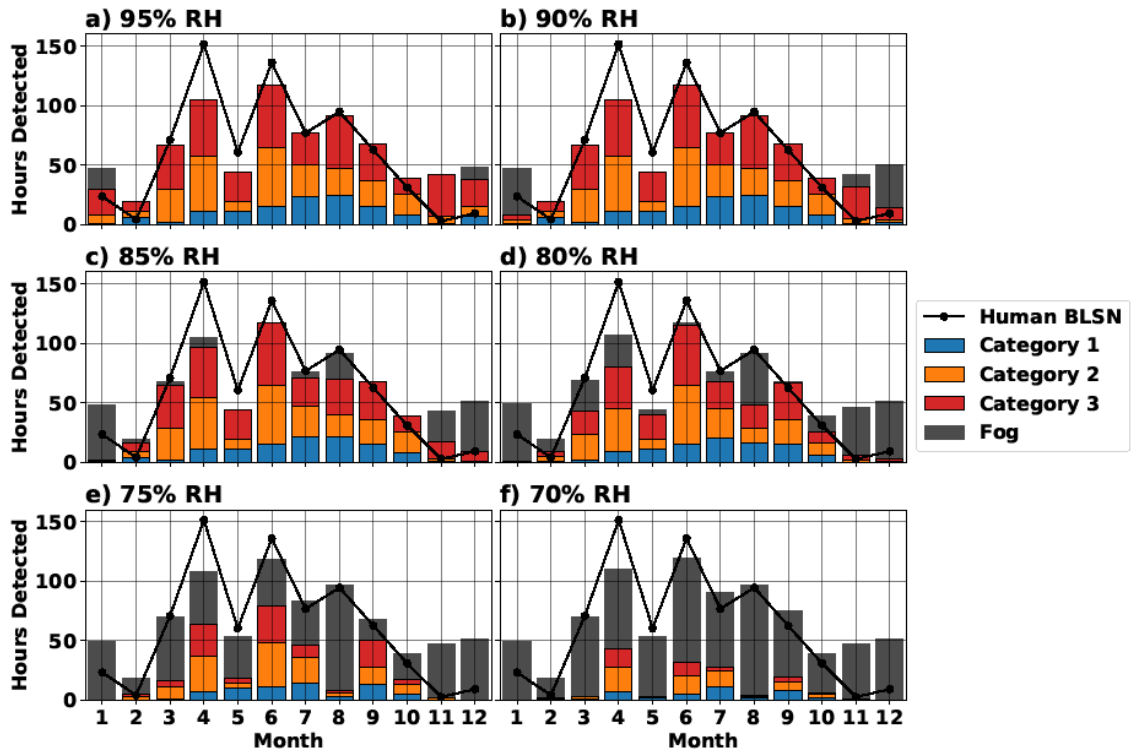


Figure 36. Monthly hours of fog and BLSN separated by category for the 5-min algorithm with varied RH thresholds. Human observations are shown in black dots.

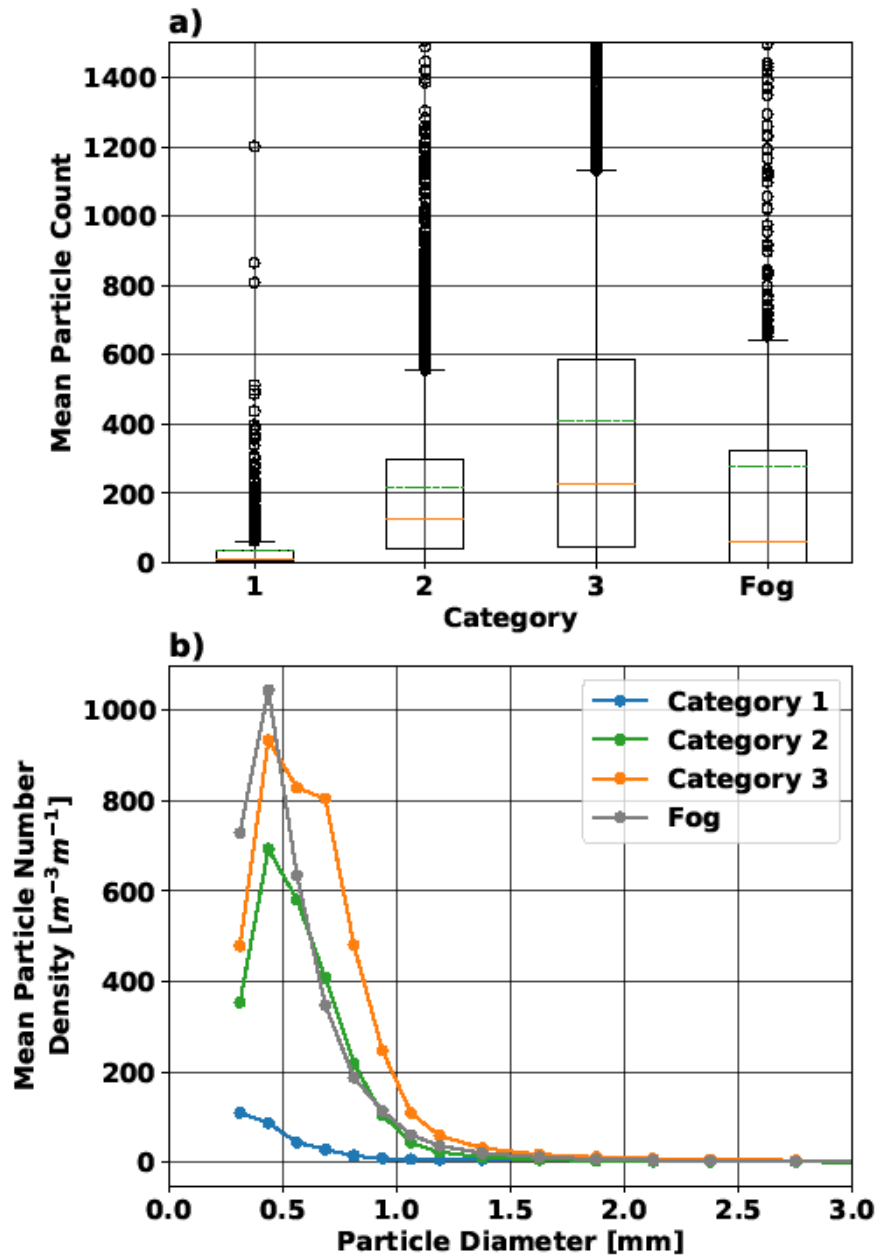


Figure 37. a) Boxplots showing the distribution of mean particle counts from the Parsivel² for each category based on the five-minute algorithm. The orange solid and green dashed lines represent the median and mean of the distribution, respectively. b) Mean particle number density distributions from Parsivel² for each category.

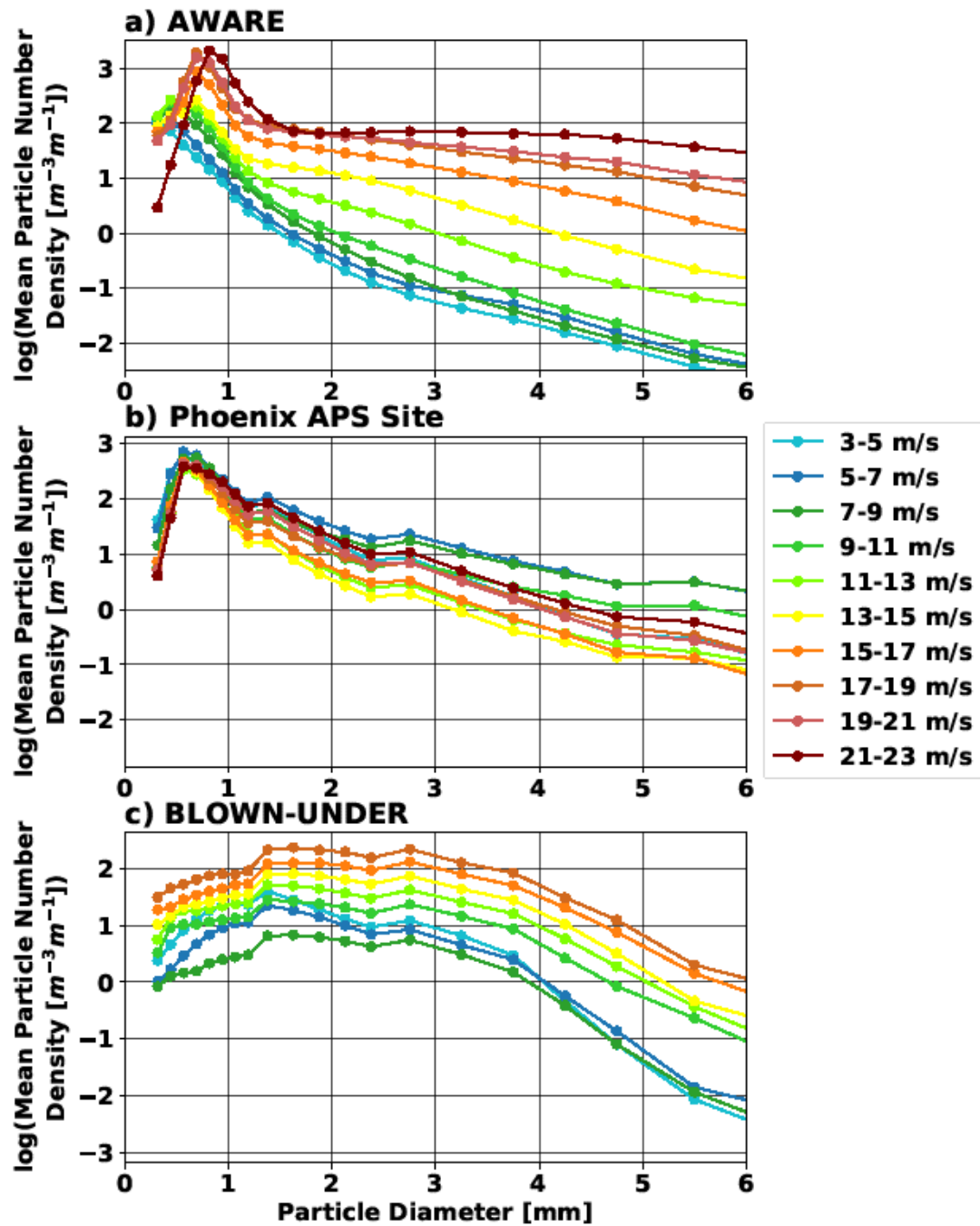


Figure 38. Logarithmic particle number density distributions from the Parsivel² for 2 m s⁻¹ wind speed increments for a) AWARE Campaign observations, b) observations from the Phoenix APS site, and c) BLOWN-UNDER.

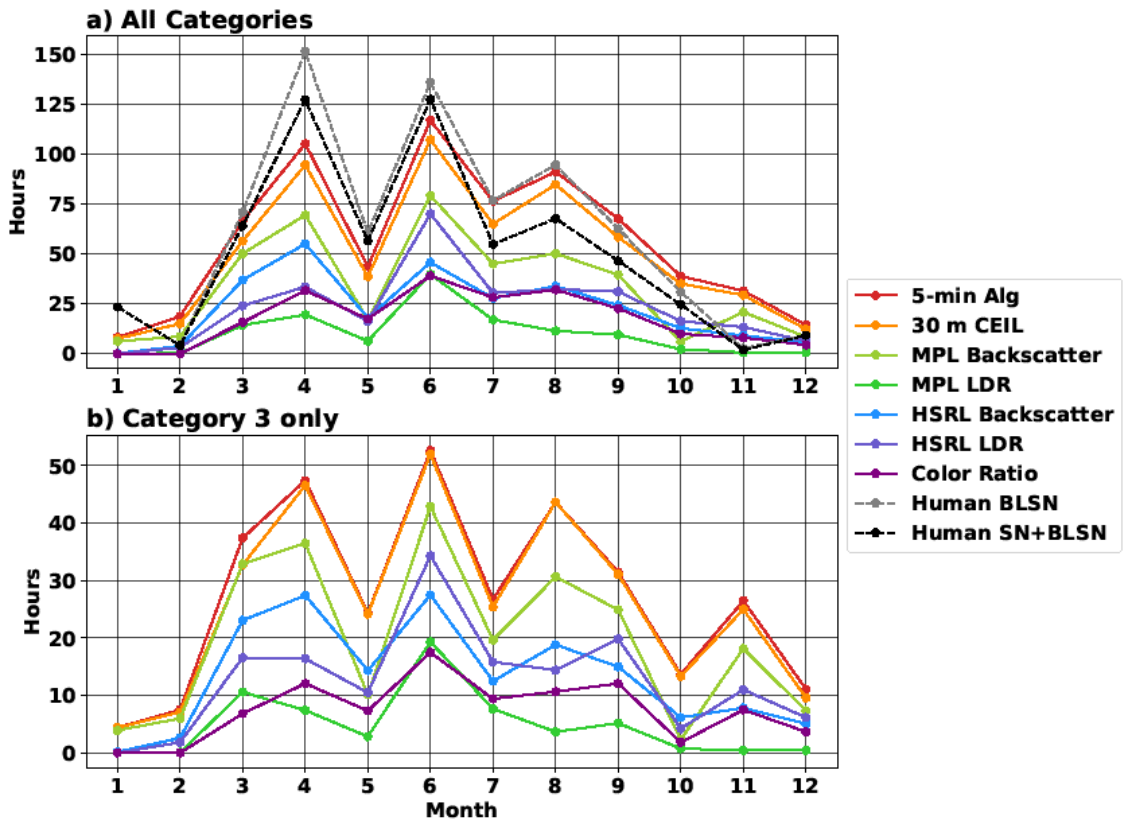


Figure 39. Monthly hours of BLSN for each algorithm and human observations of BLSN with and without falling snow during a) all BLSN detected by the five-minute algorithm, and b) only Category 3 BLSN.

Table 13. Annual and seasonal hours of BLSN for each algorithm during BLSN times detected by the five-minute algorithm. Percentages given are the proportion of five-minute algorithm detections that met said criteria.

<i>Algorithm</i>	<i>Autumn (MAM)</i>	<i>Winter (JJA)</i>	<i>Spring (SON)</i>	<i>Summer (DJF)</i>	<i>Total</i>
	<i>Hours (Proportion)</i>	<i>Hours (Proportion)</i>	<i>Hours (Proportion)</i>	<i>Hours (Proportion)</i>	<i>Hours (Proportion)</i>
<i>5-min</i>	<i>215.3</i>	<i>284.4</i>	<i>138.0</i>	<i>41.3</i>	<i>679.0</i>
<i>30 m CEIL</i>	183.2 (85.1%)	256.9 (90.3%)	122.8 (89.0%)	34.8 (84.2%)	604.1 (89.0%)
<i>MPL BS</i>	136.5 (63.4%)	174.3 (61.3%)	66.5 (48.2%)	23.3 (56.3%)	400.6 (59.0%)
<i>MPL LDR</i>	40.2 (18.7%)	68.2 (24.0%)	12.3 (8.9%)	0.8 (2.0%)	121.6 (17.9%)
<i>HSRL BS</i>	109.9 (51.1%)	107.4 (37.8%)	46.1 (33.4%)	9.8 (23.6%)	273.2 (40.2%)
<i>HSRL LDR</i>	73.8 (34.3%)	132.8 (46.7%)	60.8 (44.0%)	9.5 (23.0%)	276.8 (40.8%)
<i>CR</i>	64.8 (30.1%)	99.2 (34.9%)	40.6 (29.4%)	4.4 (10.7%)	209.0 (30.8%)

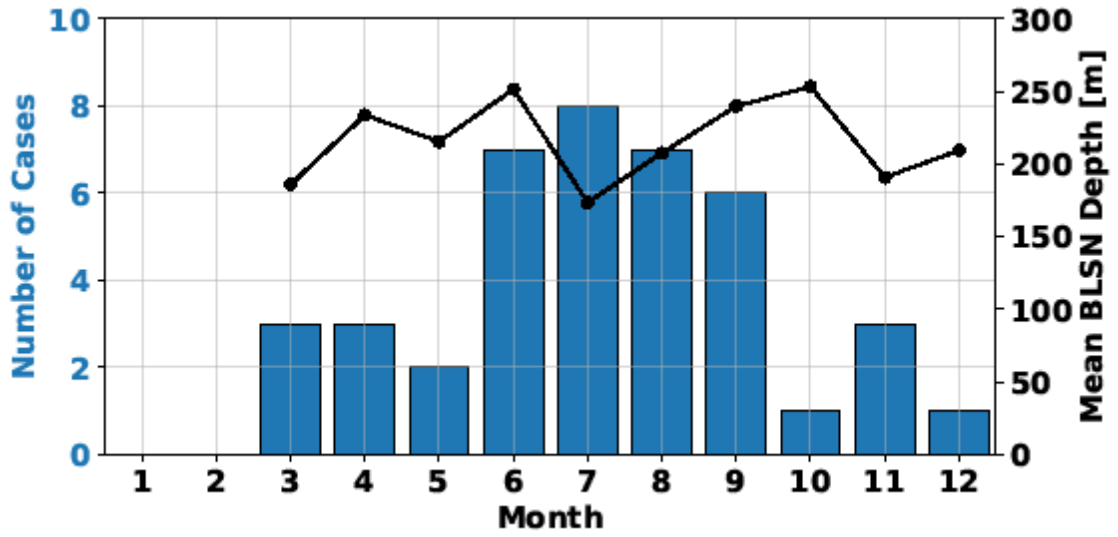


Figure 40. Monthly cases (blue bars) mean BLSN depth (black line) detected by the probabilistic algorithm.

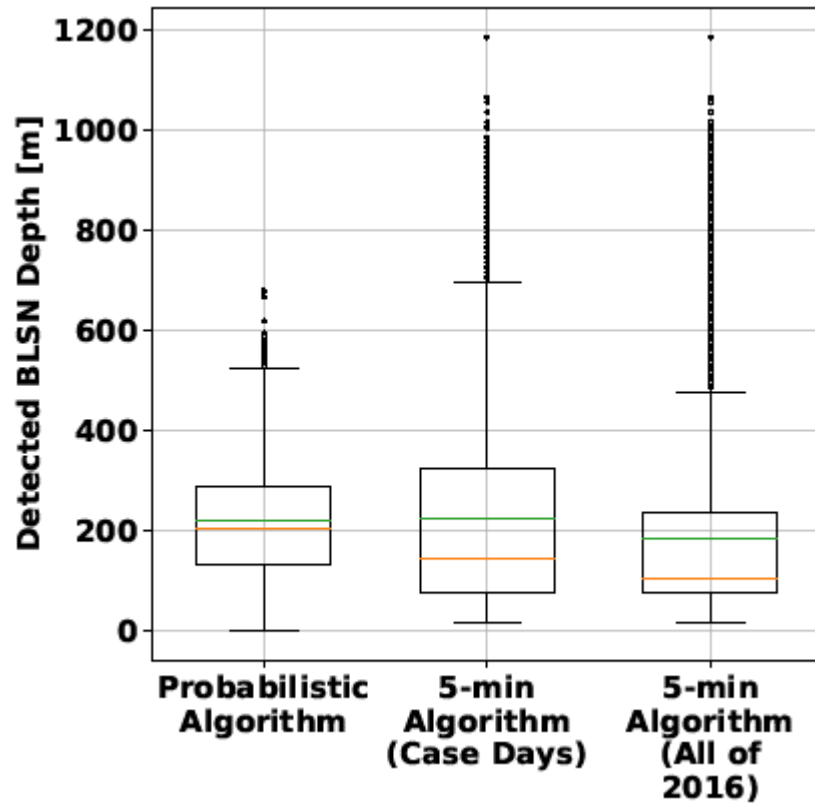


Figure 41. Boxplots of detected BLSN depth for the probabilistic algorithm and five-minute algorithm for the 41 case days, and the five-minute algorithm for all of 2016. The box represents the interquartile range of the distribution, and the whiskers cover the minimum and maximum of the data within 1.5 times the interquartile range of the median. Observations falling outside of the whiskers (outliers) are shown as black dots. Orange (green) lines show the median (mean) depth of the distribution.

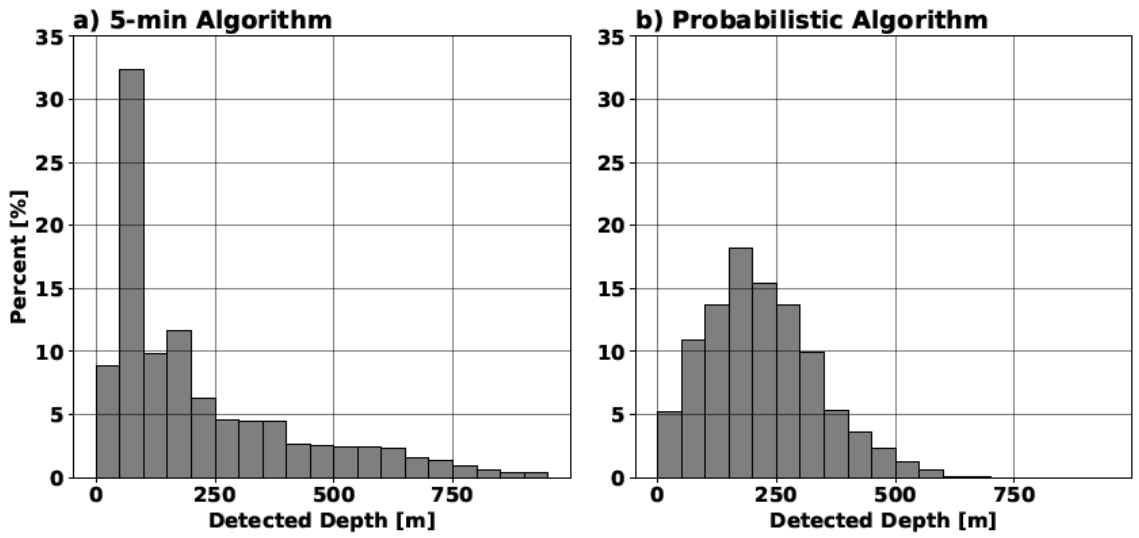


Figure 42. Histograms of BLSN depths detected by a) the five-minute algorithm and b) the probabilistic algorithm for the 41 case days.

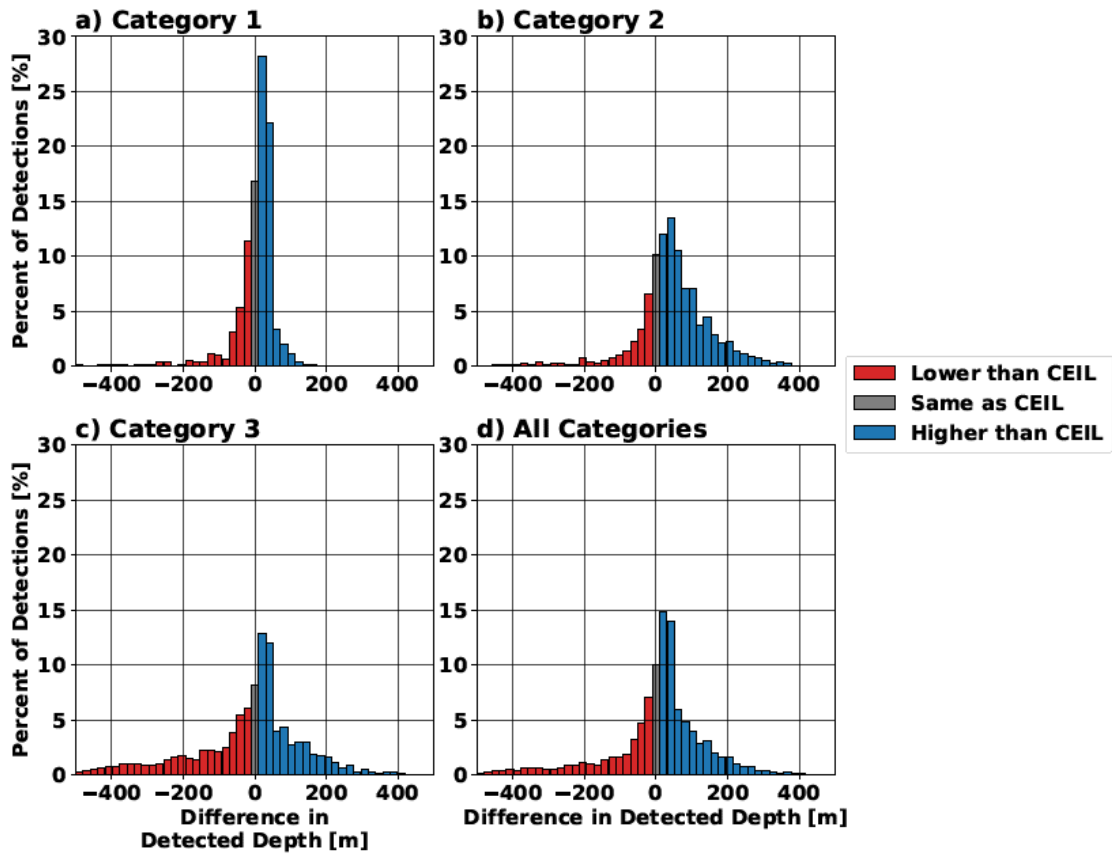


Figure 43. Histograms of the differences between the probabilistic and five-minute BLSN depths (probabilistic - 5 min) for each category.

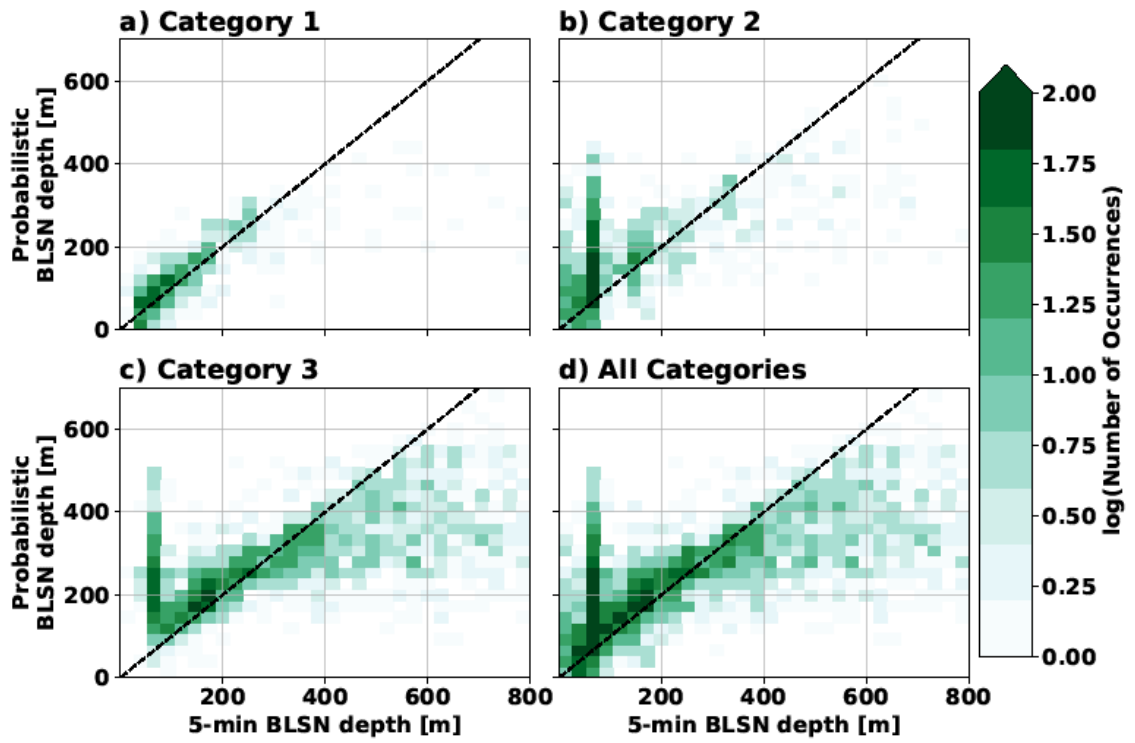


Figure 44. Two-dimensional histograms of probabilistic vs. five-minute algorithm BLSN depths.

The dashed lines represent the 1:1 relationship.

Table 14. Number of analyzed hours and detected BLSN depth for the probabilistic and 5-min BLSN algorithms for BLSN case days.

<i>Category</i>	<i>Hours Analyzed</i>	<i>Mean Depth [m]</i>	<i>5-min Mean Depth [m]</i>	<i>Mean absolute difference [m]</i>
1	52.8	128.9	128.1	41.5
2	116.6	169.8	123.9	86.9
3	202.8	276.0	306.3	119.2
Total	372.2	218.3	222.0	97.6

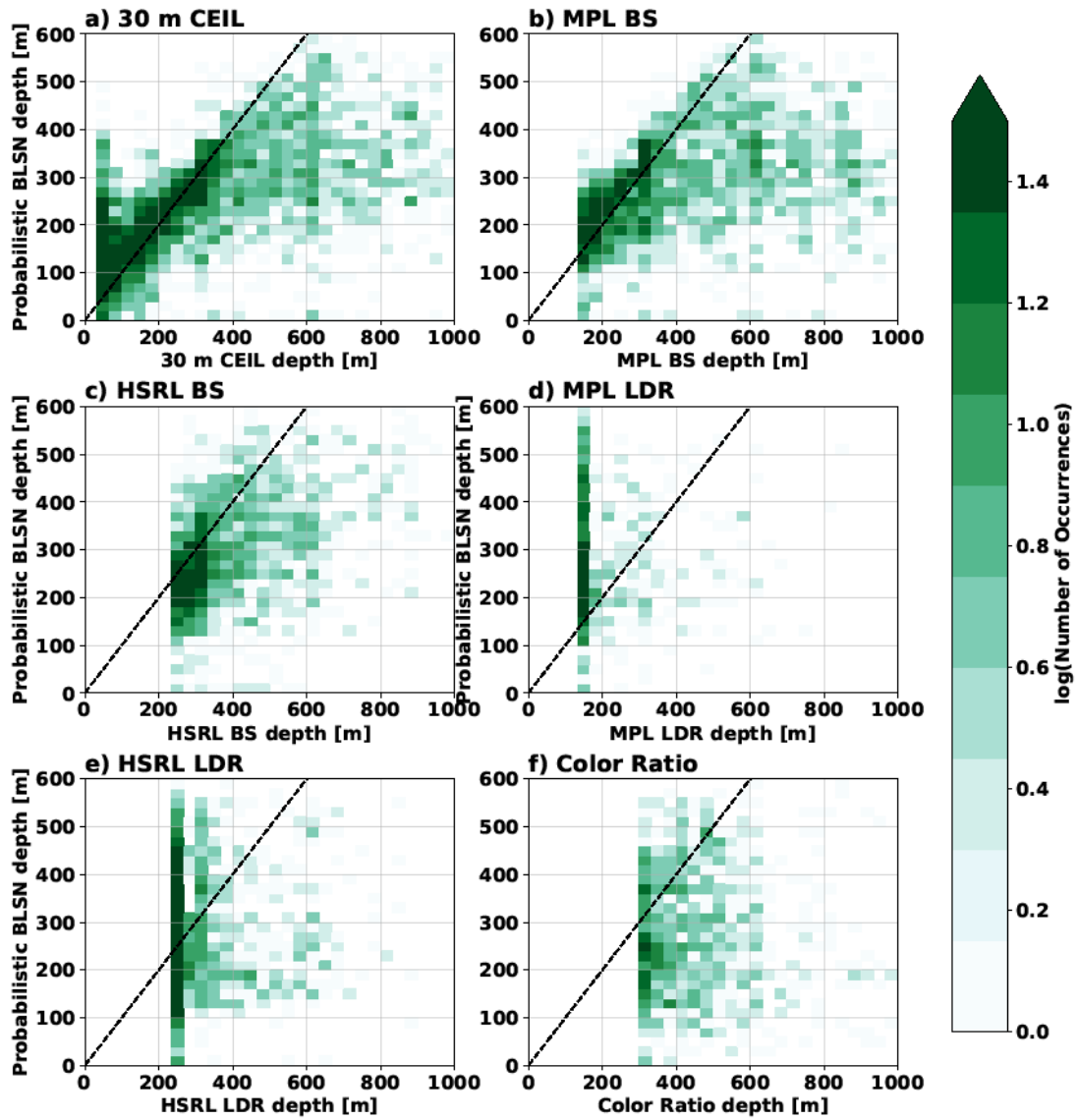


Figure 45. Two-dimensional histograms of BLSN depth vs. depth detected by the contributing algorithms. The dashed lines represent the 1:1 relationship.

Table 15. List of sensitivity tests applied to the probabilistic algorithm.

<i>Title</i>	<i>Definition</i>	<i>Algorithms Affected</i>
All Categories	Perform all algorithms for any period with any detected BLSN	All algorithms
LDR Decreased Averaging	Averaging used in LDR profile analysis reduced by 4 bins (120 m)	MPL LDR, HSRL LDR
LDR Increased Averaging	Averaging used in LDR profile analysis increased by 4 bins (120 m)	MPL LDR, HSRL LDR
Upper Level 1800-2040 m	Upper layer used in profile analysis is 1800-2040 m instead of 1200-1440 m	MPL LDR, HSRL LDR
Upper Level 1200-1500 m	Upper layer used in profile analysis is 1200-1500 m instead of 1200-1440 m	MPL LDR, HSRL LDR
CR 3 Bin Averaging	3 bin averaging used in CR profile analysis instead of 2	CR
CR 1 Bin Averaging	No averaging used in CR profile analysis instead of 2	CR
CR 10^{-9} Minimum Threshold	Minimum threshold used in CR analysis is 10^{-9} instead of 10^{-8}	CR
CR 10^{-7} Minimum Threshold	Minimum threshold used in CR analysis is 10^{-7} instead of 10^{-8}	CR
CR 10^{-3} Maximum Threshold	Maximum threshold used in CR analysis is 10^{-3} instead of 10^{-4}	CR
MPL 90 th Percentile Clear Sky	90 th percentile MPL clear sky profile used instead of 95 th	MPL BS, MPL LDR
MPL 98 th Percentile Clear Sky	98 th percentile MPL clear sky profile used instead of 95 th	MPL BS, MPL LDR
HSRL 90 th Percentile Clear Sky	90 th percentile HSRL clear sky profile used instead of 95 th	HSRL BS, HSRL LDR
HSRL 98 th Percentile Clear Sky	98 th percentile HSRL clear sky profile used instead of 95 th	HSRL BS, HSRL LDR
CEIL 90 th Percentile Clear Sky	90 th percentile CEIL clear sky profile used instead of 95 th	30 m CEIL
CEIL 98 th Percentile Clear Sky	98 th percentile CEIL clear sky profile used instead of 95 th	30 m CEIL
No Smoothing	No smoothing applied to final depth algorithm instead of 25 min (5 bins)	Probabilistic Depth Algorithm
3 Bin Smoothing	15 min (3 bins) smoothing applied to final depth algorithm instead of 25 min (5 bins)	Probabilistic Depth Algorithm

<i>Title</i>	<i>Definition</i>	<i>Algorithms Affected</i>
7 Bin Smoothing	35 min (7 bins) smoothing applied to final depth algorithm instead of 25 min (5 bins)	Probabilistic Depth Algorithm
30% of Criteria Met	30% of valid algorithms need to detect BLSN in the bin instead of 50%	Probabilistic Depth Algorithm
40% of Criteria Met	40% of valid algorithms need to detect BLSN in the bin instead of 50%	Probabilistic Depth Algorithm
60% of Criteria Met	60% of valid algorithms need to detect BLSN in the bin instead of 50%	Probabilistic Depth Algorithm
70% of Criteria Met	70% of valid algorithms need to detect BLSN in the bin instead of 50%	Probabilistic Depth Algorithm

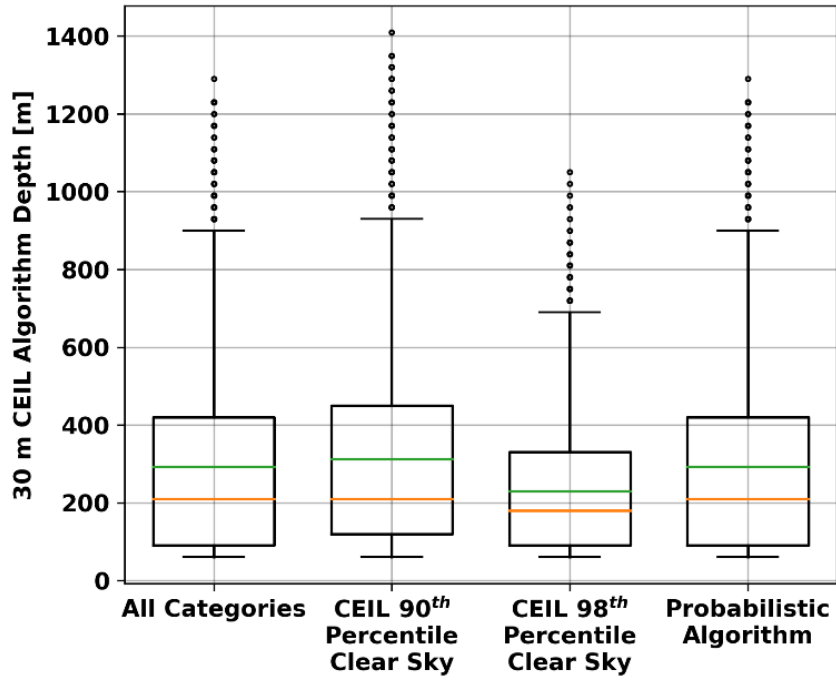


Figure 46. Boxplots of BLSN depths detected by the 30 m CEIL algorithm for the various sensitivity tests. Sensitivity tests are as defined in

Table 15. Orange (green) line shows the median (mean) depth of the distribution.

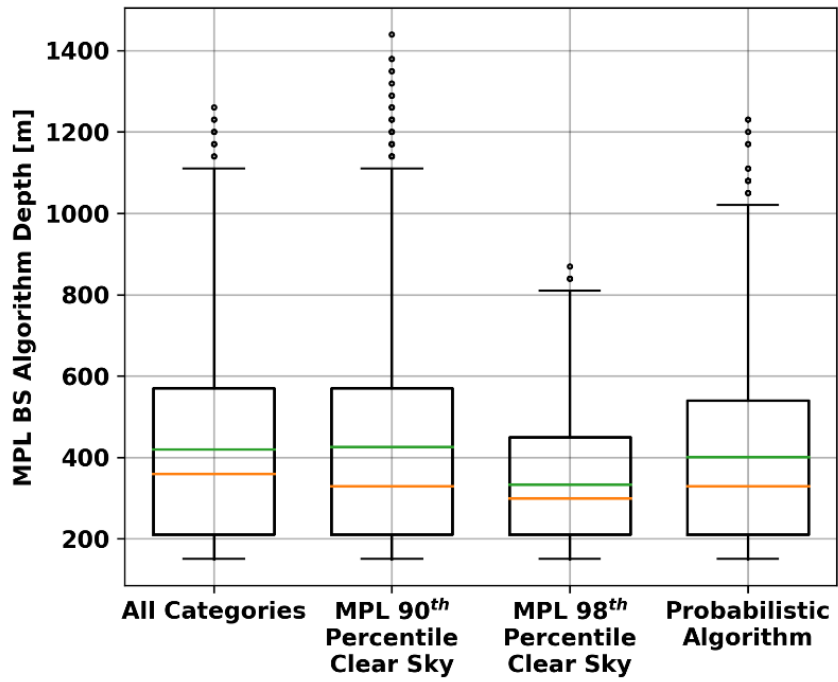


Figure 47. As in Figure 46, but for the MPL BS algorithm.

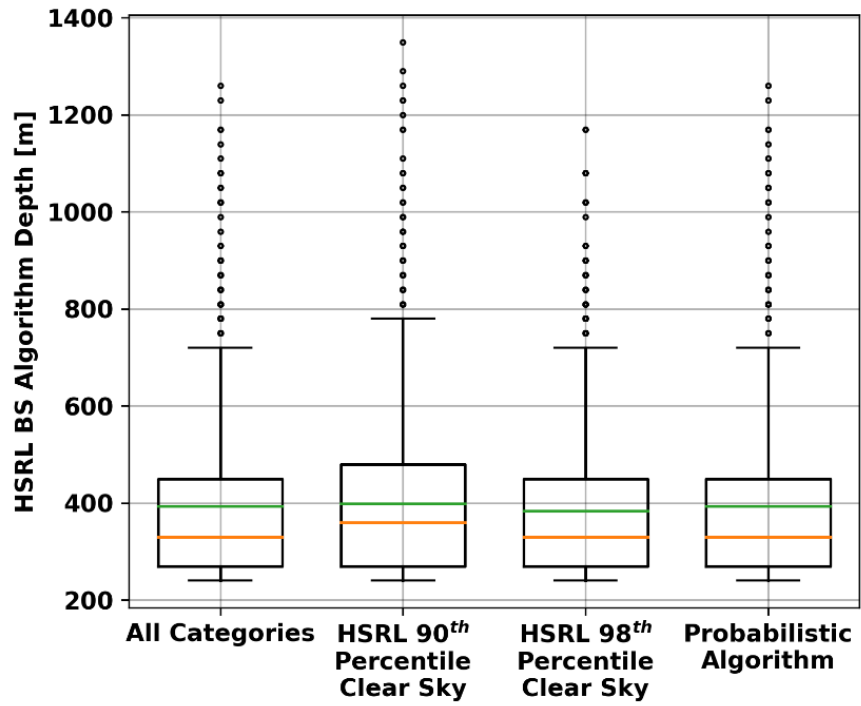


Figure 48. As in Figure 46, but for the HSRL BS algorithm.

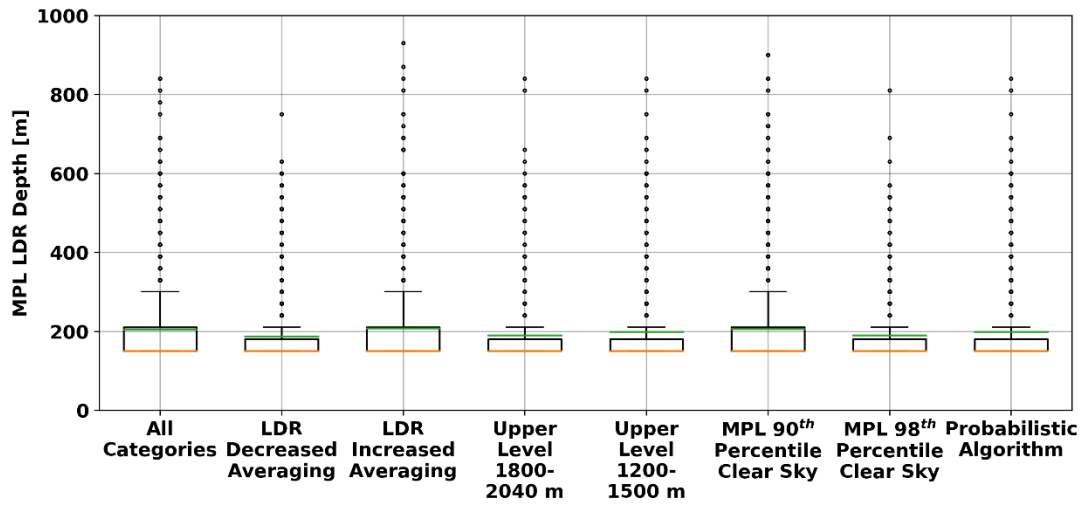


Figure 49. As in Figure 46, but for the MPL LDR algorithm.

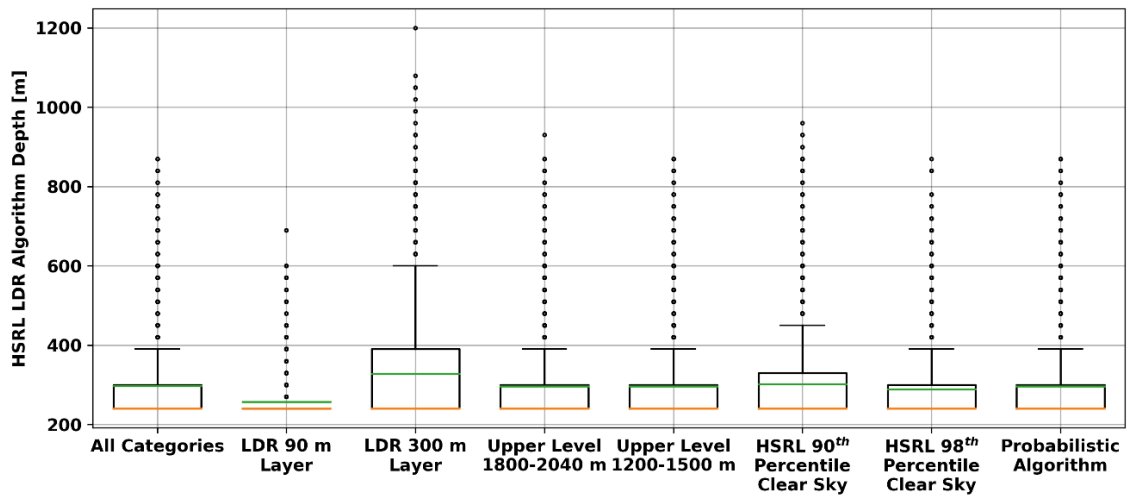


Figure 50. As in Figure 46, but for the HSRL LDR algorithm.

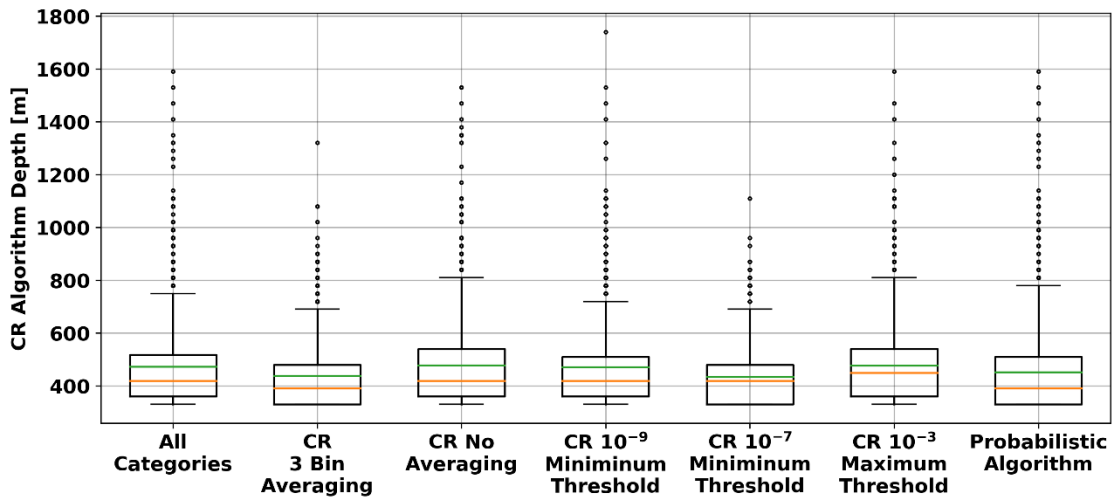


Figure 51. As in Figure 46, but for the CR algorithm.

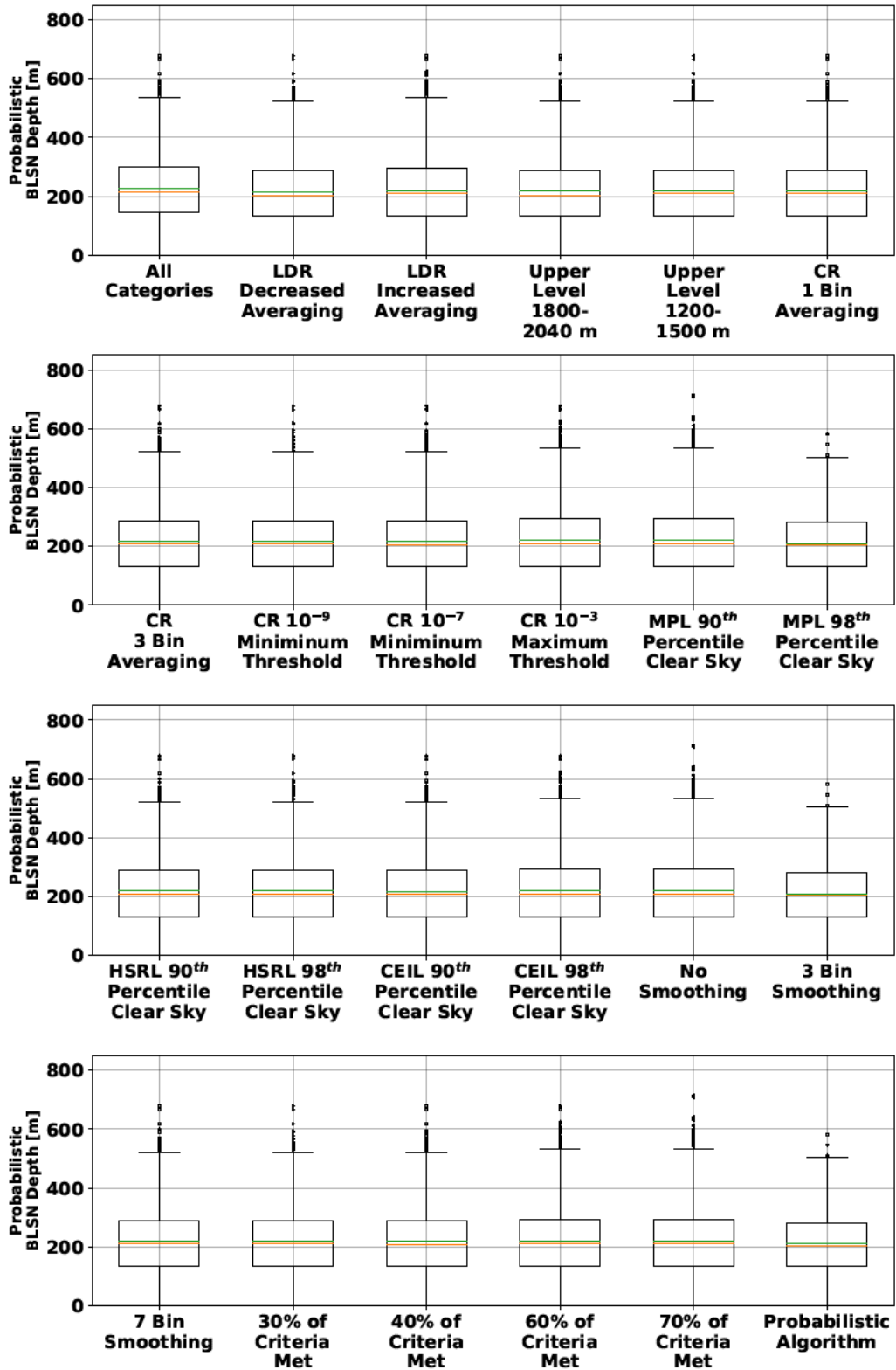


Figure 52. As in Figure 46, but for the probabilistic depth algorithm.

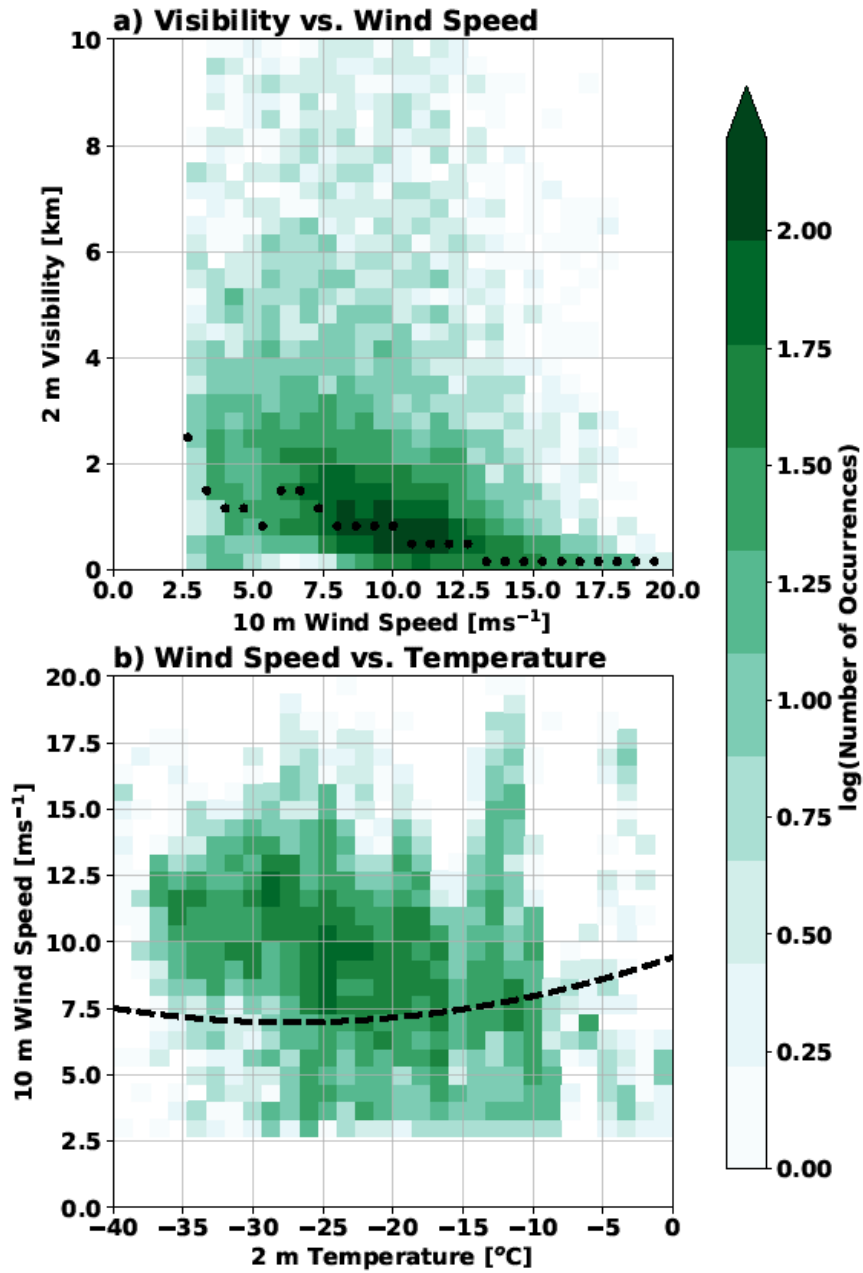


Figure 53. Two-dimensional histograms of a) 2 m visibility versus 10 m wind speed, and b) wind speed versus temperature for all BLSN detections by the five-minute algorithm. Dots in a) denoted the visibility bin with the highest occurrence for each wind speed bin. The dashed line in b) shows the relationship derived by Li and Pomeroy (1997b).

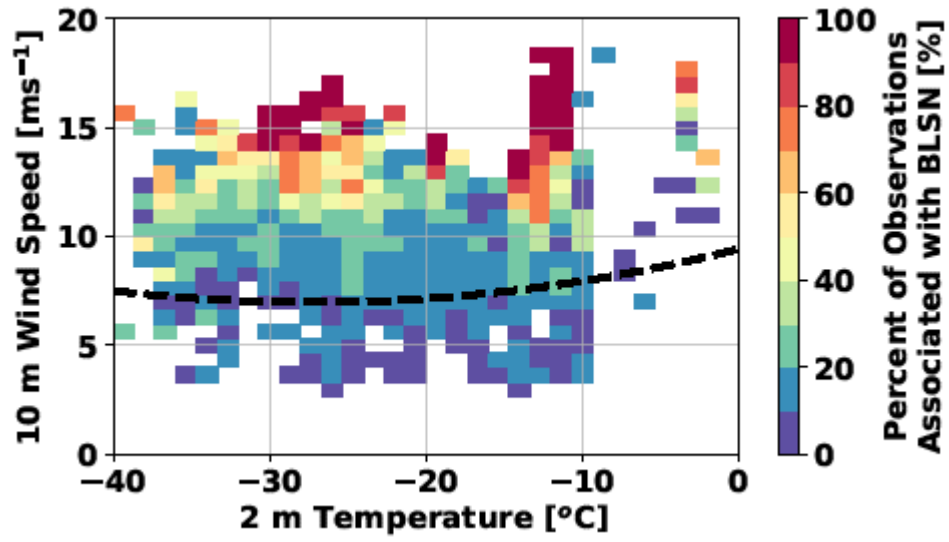


Figure 54. Percent of observations in each wind speed/temperature bin associated with BLSN detections. Bins are as those shown in Figure 53b. The dashed line shows the relationship derived by Li and Pomeroy (1997b).

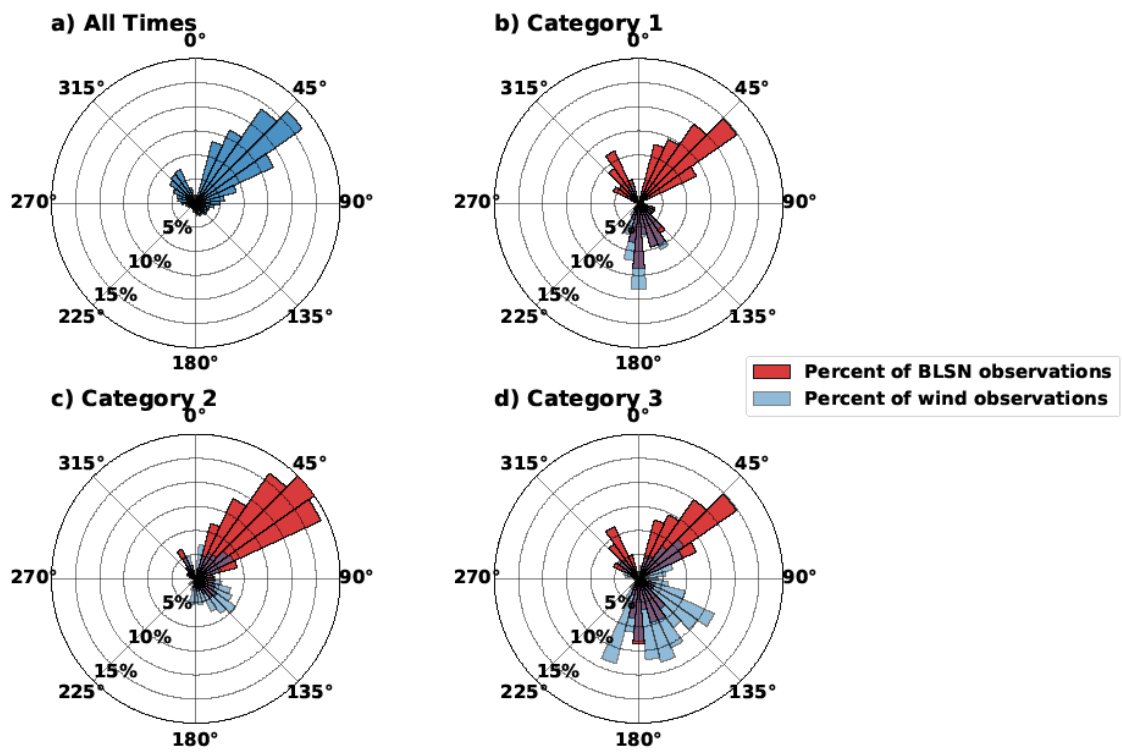


Figure 55. Distribution of 10 m wind direction occurrence for each five-minute period during 2016 for a) all times and b-d) Category 1-3 BLSN cases. Blue (red) bars represent the percent of wind (BLSN) observations in each 10° wind direction bin.

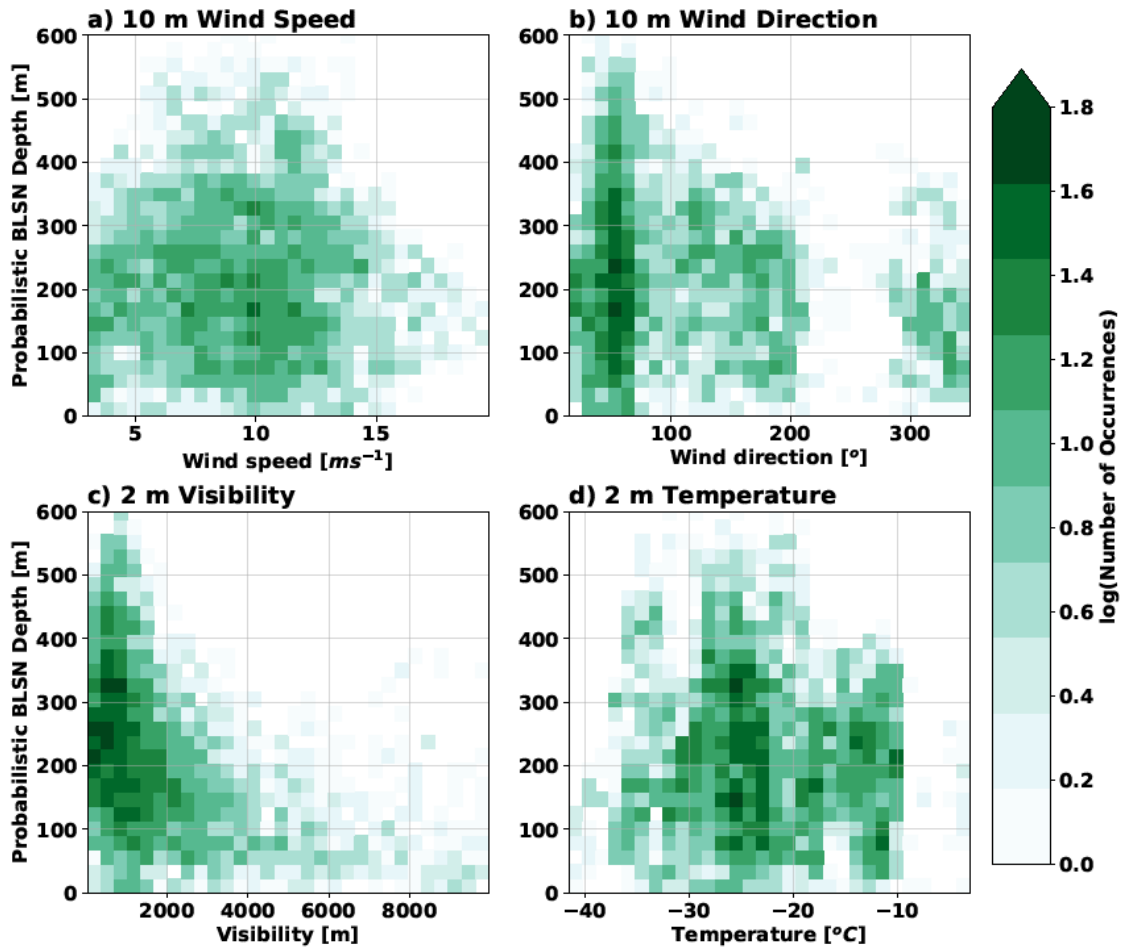


Figure 56. Two-dimensional histograms of probabilistic BLSN depth vs. meteorological variables from the MET instrumentation.

CHAPTER 6

CONCLUSIONS

The objective of this thesis was to investigate BLSN at McMurdo Station during the AWARE Field Campaign. The use of a wide range of observations available from the AMF2 allowed for the most comprehensive remote sensing study of the process to date. Characterization of BLSN was based on modifications to the ceilometer-based detection algorithm derived by Gossart et al. (2017) to improve the detection of BLSN plumes. Additional instruments such as the MPL, HSRL, and KAZR were included to generate a better estimate of BLSN plume height. Frequencies of BLSN during the AWARE campaign were compared to a climatology of human observations at this site. The results of the presented work are summarized below.

Human Climatology of BLSN at McMurdo Station

Human observers reported an average BLSN frequency of 9.2% at McMurdo Station over the 18 years of available records, with a total range of 4.0-14.0%. June had the highest frequency of the process (16.3% on average), while December had the lowest occurrence (mean of 1.6%). BLSN at this location occurred concurrently with falling precipitation most of the time, accounting for 44.5-82.2% of annual observations. Based on human observations, BLSN frequency was slightly below average during AWARE (8.2%).

BLSN During the AWARE Field Campaign

The BLSN detection algorithm derived by Gossart et al (2017) was applied to ceilometer observations from the campaign. The algorithm detected 1234.9 hours of BLSN (14.1%) in 2016, compared to 723.2 hours suggested by human observations. Through the reduction of temporal averaging and the inclusion of basic meteorological thresholds (10

m wind speed, 2 m visibility, and 2 m RH), BLSN detection was decreased to 679.0 hours (7.7%), with increased agreement with human observations. Better agreement between the algorithm and human observations was seen during the summer months, when the 90% RH threshold allowed for the removal of advective fog that was falsely detected as BLSN with the original scheme.

Based on the results of the human observations along with the Gossart and five-minute algorithms with and without thresholds, the estimated frequency of BLSN during the AWARE Field Campaign was 7.7-12.0%. Extrapolating this range of frequencies based on the record of human observations suggests that the annual frequency of BLSN occurrence at McMurdo Station is 3.5-21.3%. BLSN frequency for the region based on space-borne lidar studies is estimated to be ~5% (Palm et al. 2011, 2018a), but ground-based study allows for the inclusion of cases when cloud cover is present so a higher occurrence is expected.

Investigation of Parsivel² observations during BLSN periods yielded artifacts in the observations at high wind speeds ($> 10 \text{ ms}^{-1}$), as previously noted in Friedrich et al. (2013). These artifacts appeared as decreases in particle number density in the smallest size bins and increases in the number density of large particles, including those larger than expected for falling snow or BLSN. As a result, the reader is cautioned that Parsivel² observations are suspect during the strongest BLSN episodes associated with winds $> 10 \text{ ms}^{-1}$. It is hypothesized that number concentrations are too high for the instrument and shading by multiple particles yields voltage drops determined to be larger than reality.

During the initial investigation of BLSN, it was clear that the ceilometer only algorithm struggled with detecting plume heights during many events due to complicated backscatter profiles associated with falling snow. To improve estimation of BLSN height, the suite of remotely-sensed observations available at the AMF2 were incorporated into a probabilistic algorithm for BLSN height. This approach provided estimates of BLSN depth that were not impacted by noise/artifacts in any one set of observations. The probabilistic algorithm was applied to 41 case days during the campaign with prolonged BLSN events. This yielded an average depth of 218.3 m with Category 3 events seeing the deepest plumes. Overall, 43% of detected plumes were estimated to be less than 200 m in depth. The mean absolute difference between the depth estimated by the five-minute algorithm and that using the probabilistic approach was 97.6 m. The depth detected by the probabilistic algorithm was generally similar to that given by the five-minute algorithm for Category 1 events, with a mean absolute difference of 41.5 m. Differences were larger for Categories 2 and 3, where the mean absolute differences were 86.9 m and 119.2 m, respectively, because more plumes were deep enough to reach the detection level of the additional instruments and complex backscatter profiles are more common for these categories. The results of the probabilistic algorithm were most closely related to that of the backscatter coefficient-based algorithms, as the LDR and color ratio observations generally help to distinguish between precipitation and BLSN during mixed events. The probabilistic approach tended to regulate the heights found by the five-minute algorithm; the depth of very deep plumes was reduced while very shallow plumes were made deeper. Since the selected case days are generally more intense events, it is expected that the difference in performance would be smaller if applied to all of the BLSN that occurred.

Connections Between BLSN and Meteorological Conditions

Analysis of the BLSN environment was performed through examination of meteorological observations during detected BLSN periods. It was found that most BLSN was associated with 10 m wind speeds of 5.0-15.0 ms⁻¹ and 2 m visibilities below 6 km. The most common wind direction during BLSN was northeasterly due to topography, though southerly winds also produced some BLSN associated with downsloping events.

Relationships between estimated BLSN depth and environmental variables were also investigated. No clear relationship was found between 10 m wind speed and direction or temperature with BLSN depth, as noted by previous studies (Mahesh et al. 2003; Gossart et al. 2017). The clearest relationship emerged with 2 m visibility; the deepest plumes were observed with the lowest visibilities (< 2 km), suggesting that the most intense events at the surface may be associated with deeper BLSN plumes.

Future Work

While this study yielded promising results, further work is needed to refine and validate the detection and characteristics of BLSN. Repeating this study at additional locations (particularly other high latitude ARM sites) is required to assess the validity of the algorithms in various locations. Since most of the remote sensing instruments used in this study do not record usable data until at least ~100-200 m above the instrument, which is above the top of many BLSN layers, future studies may consider tilting the instruments such that usable data begins nearer to the surface. This technique was used by Mahesh et al. (2003) to retrieve observations from the MPL in the near-surface layer. Fine-tuning of the LDR and CR algorithms is also required to improve their performance. For example, the development of instrument-specific values for LDR will likely help to improve the

performance of the individual algorithms, since the same values were applied to observations from both the MPL and HSRL in this study. This type of alteration may bring more confidence in estimated BLSN depths. Additionally, the depth estimations may be compared to inversion heights determined by atmospheric soundings, as it is hypothesized that BLSN is limited to the surface inversion layer (Mahesh et al. 2003; Palm et al. 2018b).

Further, ground truth verification would be invaluable in assessing the performance of the developed algorithms. Large-scale field campaigns allowing for the direct observation of BLSN plumes with height would allow for direct comparisons with algorithm results, and a truthful understanding of the validity of the detection and depth estimations provided. Also, human observations of BLSN made near to the site of the instruments would be valuable to help validate BLSN occurrence.

Further investigation is needed to determine the relationships between BLSN occurrence and depth and the environment it occurs in. The complex terrain at McMurdo Station likely complicates the relationships between environmental variables, such as wind speed, and the properties of the plume. Studying the process in a flat, isolated environment would likely help to clarify whether or not such relationships exist.

Finally, this work can also be used by the modelling community to verify simulations of the process and its impacts. Having both detection and an estimation of depth can help to assess the impact of BLSN on the regional climate, allowing for improved estimations of sublimation and radiative properties, as well as impacts on the regional surface mass balance of ice surfaces.

APPENDIX A: List of Instrumentation at the AMF2

Table 16. Instruments deployed to McMurdo Station (adapted from Lubin et al. 2015).

<i>Instrument Name</i>	<i>Quantities Measured</i>
X-band and Ka-band scanning ARM cloud radar (SACR)	Cloud particle co-polar and cross-polar radar reflectivity, Doppler velocity, linear depolarization ratio, differential reflectivity
Scanning W- band ARM cloud radar (SWACR)	Cloud particle radar reflectivity, Doppler power spectrum
Ka-band ARM zenith radar (KAZR)	Cloud particle Doppler moments (reflectivity, vertical velocity, spectral width) at high (30 m) range resolution
Atmospheric emitted radiance interferometer (AERI)	Absolute thermal infrared spectral radiance emitted by the atmosphere down to the instrument
High spectral resolution lidar (HSRL)	Aerosol optical depth, volume backscatter, cross section, cloud and aerosol depolarization
Micropulse lidar (MPL)	Altitude of cloud layers
Vaisala ceilometer (VCEIL)	Attenuated backscatter coefficient, cloud base height
Beam-steerable radar wind profiler (BSRWP)	Wind and virtual temperature profiles
Parsivel optical disdrometer (PARSIVEL)	Precipitation particle size distribution and fall speed
CCN counter (CCN)	Cloud condensation nuclei as function of supersaturation
Condensation particle counter (CPC)	Total aerosol particle concentration down to diameter 10 nm
Hygroscopic tandem differential mobility analyzer (HTDMA)	Aerosol size, mass, or number distribution as function of RH
Ambient nephelometer (NEPH AMB)	Aerosol light scattering coefficient at ambient RH
Dry nephelometer (NEPH DRY)	Dry aerosol light scattering coefficient
Ozone (O3)	Ozone concentration
Particle soot absorption photometer (PSAP)	Optical transmittance of aerosol particles A_e
Aerosol filter sampling (AER FLTR)	Aerosol chemical composition
Upward-looking precision spectral pyranometer (SKYRAD PSP)	Downwelling total shortwave irradiance

<i>Instrument Name</i>	<i>Quantities Measured</i>
Upward-looking Eppley model 8-48 diffuse pyranometer (SKYRAD 8-48)	Downwelling diffuse shortwave irradiance
Upward-looking precision infrared radiometer (SKYRAD PIR)	Downwelling longwave irradiance
Upward-looking Infrared thermometer (SKYRAD IRT)	Sky equivalent blackbody temperature
Downward-looking precision spectral pyranometer (GRNDRAD PSP)	Upwelling shortwave radiation reflected by surface
Downward-looking precision infrared radiometer (GRNDRAD PIR)	Upwelling longwave radiation emitted by surface
Downward-looking Infrared thermometer (GRNDRAD IRT)	Surface equivalent blackbody temperature
Cimel sunphotometer (CSPHOT)	Multispectral direct solar irradiances
Multifilter rotating shadowband radiometer (MFRSR)	Direct normal, diffuse horizontal, and total horizontal irradiances at six standard wavelengths
Analytical Spectral Devices FieldSpec Pro shortwave spectroradiometer (ASD)	Downwelling spectral shortwave irradiance 350–2200 nm
Eddy correlation flux measurement system (ECOR)	Surface turbulent fluxes of momentum, sensible heat, latent heat, and carbon dioxide
Total sky imager (TSI)	Cloud fraction
Vaisala present weather detector (PWD)	Visibility, precipitation detection
Hotplate total precipitation sensor (TPS)	Precipitation amount
G-band vapor radiometer (GVRP)	High-time-resolution water vapor and temperature profiling, and column-integrated liquid water and water vapor
Microwave radiometer, two channel (MWR, 2C)	Column-integrated liquid water and water vapor
Balloon-borne sounding system (SONDE)	Vertical profiles of T, P, RH, wind speed and direction
Meteorological instrumentation at AMF (MET)	Near-surface (2 m) T, P, RH, wind speed and direction
Local meteorology at top of aerosol observing system (AOS) stack (AOS MET)	Wind speed, direction, T, RH, P

REFERENCES

- Andreas, A., M. Dooraghi, A. Habte, M. Kutchenreiter, I. Reda, M. Sengupta, and National Renewable Energy Laboratory, 2018: *Solar Infrared Radiation Station (SIRS), Sky Radiation (SKYRAD), Ground Radiation (GNDRAD), and Broadband Radiometer Station (BRS) Instrument Handbook*. DOE/SC-ARM-TR-025, 58 pp, <http://www.osti.gov/servlets/purl/1432706/>
- Battaglia, A., E. Rustemeier, A. Tokay, U. Blahak, and C. Simmer, 2010: PARSIVEL Snow Observations: A Critical Assessment. *Journal of Atmospheric and Oceanic Technology*, **27**, 333–344, <https://doi.org/10.1175/2009JTECHA1332.1>.
- Bharadwaj, N., A. Lindenmaier, K. Widener, K. Johnson, and V. Venkatesh, 2013: Ka-band ARM Zenith Profiling Radar Network for Climate Study. 36th Conference on Radar Meteorology, Breckenridge, Colorado, American Meteorological Society, 14A.8.
- , ———, D. Nelson, B. Isom, J. Hardin, A. Matthews and T. Wendler: 2015: Ka ARM Zenith Radar (KAZRGE). 2015-11-17 to 2017-01-02, ARM Mobile Facility (AWR) McMurdo Station Ross Ice Shelf, Antarctica; AMF2 (M1). ARM Data Center, accessed 08 January 2020. <http://dx.doi.org/10.5439/1025214>.
- Bindschadler, R., 2006: The environment and evolution of the West Antarctic ice sheet: setting the stage. *Philosophical Transactions of the Royal Society A: Mathematical, Physical and Engineering Sciences*, **364**, 1583–1605, <https://doi.org/10.1098/rsta.2006.1790>.
- Bintanja, R., 2001: Modification of the wind speed profile caused by snowdrift: Results from observations. *Quarterly Journal of the Royal Meteorological Society*, **127**, 2417–2434, <https://doi.org/10.1002/qj.49712757712>.
- , and C. H. Reijmer, 2001: A simple parameterization for snowdrift sublimation over Antarctic snow surfaces. *Journal of Geophysical Research: Atmospheres*, **106**, 31739–31748, <https://doi.org/10.1029/2000JD000107>.
- Bourdages, L., T. J. Duck, G. Lesins, J. R. Drummond, and E. W. Eloranta, 2009: Physical properties of High Arctic tropospheric particles during winter. *Atmospheric Chemistry and Physics*, **9**, 7781–7823.
- Bromwich, D. H., J. P. Nicolas, A. J. Monaghan, M. A. Lazzara, L. M. Keller, G. A. Weidner, and A. B. Wilson, 2013: Central West Antarctica among the most rapidly

- warming regions on Earth. *Nature Geoscience*, **6**, 139–145, <https://doi.org/10.1038/ngeo1671>.
- Budd, W. F., 1966: The Drifting of Nonuniform Snow Particles. *Studies in Antarctic Meteorology*, American Geophysical Union (AGU), 59–70.
- , W. R. J. Dingle, and U. Radok, 1966: The Byrd Snow Drift Project: Outline and Basic Results. *Studies in Antarctic Meteorology*, American Geophysical Union (AGU), 71–134.
- Burrows, W. R., R. A. Treidl, and R. G. Lawford, 1979: The Southern Ontario Blizzard of January 26 and 27, 1978. *Atmosphere-Ocean*, **17**, 306–320, <https://doi.org/10.1080/07055900.1979.9649068>.
- Changnon, S. A., and D. Changnon, 1978: Winter Storms and the Record-Breaking Winter in Illinois. *Weatherwise*, **31**, 218–225, <https://doi.org/10.1080/00431672.1978.9933520>.
- Clothiaux, E. E., T. P. Ackerman, G. G. Mace, K. P. Moran, R. T. Marchand, M. A. Miller, and B. E. Martner, 2000: Objective Determination of Cloud Heights and Radar Reflectivities Using a Combination of Active Remote Sensors at the ARM CART Sites. *J. Appl. Meteor.*, **39**, 645–665, [https://doi.org/10.1175/1520-0450\(2000\)039<0645:ODOCHA>2.0.CO;2](https://doi.org/10.1175/1520-0450(2000)039<0645:ODOCHA>2.0.CO;2).
- Costanza, C. A., M. A. Lazzara, L. M. Keller, and J. J. Cassano, 2016: The surface climatology of the Ross Ice Shelf Antarctica. *Int J Climatol*, **36**, 4929–4941, <https://doi.org/10.1002/joc.4681>.
- DeGaetano, A. T., T. W. Schmidlin, and D. S. Wilks, 1997: Evaluation of East Coast Snow Loads Following January 1996 Storms. *Journal of Performance of Constructed Facilities*, **11**, 90–94, [https://doi.org/10.1061/\(ASCE\)0887-3828\(1997\)11:2\(90\)](https://doi.org/10.1061/(ASCE)0887-3828(1997)11:2(90)).
- Déry, S. J., and M. K. Yau, 2002: Large-scale mass balance effects of blowing snow and surface sublimation. *Journal of Geophysical Research: Atmospheres*, **107**, ACL 8-1-ACL 8-17, <https://doi.org/10.1029/2001JD001251>.
- Elevant, K., 2010: COLLABORATIVE OBSERVATIONS OF WEATHER - A Weather Information Sharers' Community of Practice: *Proceedings of the 6th International Conference on Web Information Systems and Technology*, 6th International Conference on Web Information Systems and Technologies, Valencia, Spain, SciTePress - Science and and Technology Publications, 392–399.

- Eloranta, E. W., 2005: High Spectral Resolution Lidar. *Lidar: Range-Resolved Optical Remote Sensing of the Atmosphere*, C. Weitcamp, Ed., Springer Science+Business Media Inc., 143–163.
- Flynn, C. J., A. Mendoza, Y. Zheng, and S. Mathur, 2007: Novel polarization-sensitive micropulse lidar measurement technique. *Opt. Express*, **15**, 2785, <https://doi.org/10.1364/OE.15.002785>.
- Friedrich, K., S. Higgins, F. J. Masters, and C. R. Lopez, 2013: Articulating and Stationary PARSIVEL Disdrometer Measurements in Conditions with Strong Winds and Heavy Rainfall. *Journal of Atmospheric and Oceanic Technology*, **30**, 2063–2080, <https://doi.org/10.1175/JTECH-D-12-00254.1>.
- Gallée, H., G. Guyomarc'h, and E. Brun, 2001: Impact of Snow Drift on the Antarctic Ice Sheet Surface Mass Balance: Possible Sensitivity to Snow-Surface Properties. *Boundary-Layer Meteorology*, **99**, 1–19, <https://doi.org/10.1023/A:1018776422809>.
- Gelaro, R., and Coauthors, 2017: The Modern-Era Retrospective Analysis for Research and Applications, Version 2 (MERRA-2). *J. Climate*, **30**, 5419–5454, <https://doi.org/10.1175/JCLI-D-16-0758.1>.
- Giovinetto, M. B., D. H. Bromwich, and G. Wendler, 1992: Atmospheric net transport of water vapor and latent heat across 70°S. *Journal of Geophysical Research: Atmospheres*, **97**, 917–930, <https://doi.org/10.1029/91JD02485>.
- Goldsmith, J., 2016: *High Spectral Resolution Lidar Instrument Handbook*. DOE/SC-ARM-TR-157, 17 pp, https://www.arm.gov/publications/tech_reports/handbooks/hsrl_handbook.pdf.
- Gordon, M., and P. A. Taylor, 2009: Measurements of blowing snow, Part I: Particle shape, size distribution, velocity, and number flux at Churchill, Manitoba, Canada. *Cold Regions Science and Technology*, **55**, 63–74, <https://doi.org/10.1016/j.coldregions.2008.05.001>.
- Gossart, A., and Coauthors, 2017: Blowing snow detection from ground-based ceilometers: application to East Antarctica. *The Cryosphere*, **11**, 2755–2772, <https://doi.org/10.5194/tc-11-2755-2017>.
- , S. P. Palm, N. Souverijns, J. T. M. Lenaerts, I. V. Gorodetskaya, S. Lhermitte, and N. P. M. van Lipzig, 2020: Importance of Blowing Snow During Cloudy Conditions in East Antarctica: Comparison of Ground-Based and Space-Borne Retrievals Over

- Ice-Shelf and Mountain Regions. *Front. Earth Sci.*, **8**, 240, <https://doi.org/10.3389/feart.2020.00240>.
- Graff, J. V., and J. H. Strub, 1975: The Great Upper Plains Blizzard of January 1975. *Weatherwise*, **28**, 66–103, <https://doi.org/10.1080/00431672.1975.9931738>.
- Hanesiak, J. M., and X. L. Wang, 2005: Adverse-Weather Trends in the Canadian Arctic. *J. Climate*, **18**, 3140–3156, <https://doi.org/10.1175/JCLI3505.1>.
- Hershey, B. W., and L. F. Osborne, 2008: The Physical Nature and Prediction of Blowing Snow Within the Roadway Environment. *Surface Transportation Weather and Snow Removal and Ice Control Technology*, Vol. Number E-C126, Fourth National Conference on Surface Transportation Weather, Transportation Research Circular, 676.
- Intrieri, J. M., G. L. Stephens, W. L. Eberhard, and T. Uttal, 1993: A Method for Determining Cirrus Cloud Particle Sizes Using Lidar and Radar Backscatter Technique. *Journal of Applied Meteorology*, **32**, 1074–1082, [https://doi.org/10.1175/1520-0450\(1993\)032%3C1074:AMFDCC%3E2.0.CO;2](https://doi.org/10.1175/1520-0450(1993)032%3C1074:AMFDCC%3E2.0.CO;2).
- Kennedy, A., and C. Jones, 2020: GOES-16 Observations of Blowing Snow in Horizontal Convective Rolls on 24 February 2019. *Monthly Weather Review*, **148**, 1737–1750, <https://doi.org/10.1175/MWR-D-19-0354.1>.
- Kennedy, A. D., X. Dong, and B. Xi, 2014: Cloud fraction at the ARM SGP site. *Theor Appl Climatol*, **115**, 91–105, <https://doi.org/10.1007/s00704-013-0853-9>.
- Kind, R. J., 1981: Snow Drifting. *Handbook of Snow: Principles, Processes, Management & Use*, D.M. Gray and D.H. Male, Eds., Pergamon Press, 338–358.
- Kodama, Y., G. Wendler, and J. Gosink, 1985: THE EFFECT OF BLOWING SNOW ON KATABATIC WINDS IN ANTARCTICA. *Annals of Glaciology*, **6**, 59–62.
- Kyrouac, J. and D. Holdridge, 2015: Surface Meteorological Instrumentation (MET). 2015-11-17 to 2017-01-01, ARM Mobile Facility (AWR) McMurdo Station Ross Ice Shelf, Antarctica; AMF2 (M1). ARM Data Center, accessed 25 February 2019. <http://dx.doi.org/10.5439/1025220>.
- Lazzara, M. A., 2008: A Diagnostic Study of Antarctic Fog. University of Wisconsin-Madison, 198 pp. https://www.aos.wisc.edu/aosjournal/Volume6/theses/Matthew_Lazzara_PhD_Thesis.pdf.

- Lenaerts, J. T. M., M. R. van den Broeke, S. J. Déry, G. König-Langlo, J. Ettema, and P. K. Munneke, 2010: Modelling snowdrift sublimation on an Antarctic ice shelf. *The Cryosphere*, **4**, 179–190, <https://doi.org/10.5194/tc-4-179-2010>.
- Leonard, K. C., L.-B. Tremblay, J. E. Thom, and D. R. MacAyeal, 2012: Drifting snow threshold measurements near McMurdo station, Antarctica: A sensor comparison study. *Cold Regions Science and Technology*, **70**, 71–80, <https://doi.org/10.1016/j.coldregions.2011.08.001>.
- Li, L., and J. W. Pomeroy, 1997a: Probability of occurrence of blowing snow. *Journal of Geophysical Research: Atmospheres*, **102**, 21955–21964, <https://doi.org/10.1029/97JD01522>.
- , and J. W. Pomeroy, 1997b: Estimates of Threshold Wind Speeds for Snow Transport Using Meteorological Data. *JOURNAL OF APPLIED METEOROLOGY*, **36**, 9.
- Lubin, D., J. Verlinde, D. Bromwich, A. Vogelmann, and L. Russell, 2015: *ARM West Antarctic Radiation Experiment (AWARE) Science Plan*. <https://www.arm.gov/publications/programdocs/doe-sc-arm-15-040.pdf>.
- Lubin, D., and Coauthors, 2020: AWARE: The Atmospheric Radiation Measurement (ARM) West Antarctic Radiation Experiment. *Bulletin of the American Meteorological Society*, **101**, E1069–E1091, <https://doi.org/10.1175/BAMS-D-18-0278.1>.
- Maahn, M., 2010: Measuring Precipitation with Micro Rain Radars in Svalbard. University of Bonn, 146 pp. <https://doi.org/10.13140/RG.2.2.32317.67043>
- Mace, G. G., and Coauthors, 2006: Cloud radiative forcing at the Atmospheric Radiation Measurement Program Climate Research Facility: 1. Technique, validation, and comparison to satellite-derived diagnostic quantities. *Journal of Geophysical Research: Atmospheres*, **111**, <https://doi.org/10.1029/2005JD005921>.
- Mahesh, A., R. Eager, J. R. Campbell, and J. D. Spinhirne, 2003: Observations of blowing snow at the South Pole. *Journal of Geophysical Research: Atmospheres*, **108**, <https://doi.org/10.1029/2002JD003327>.
- Mellor, M., 1965: *Blowing Snow*. CRREL monograph; 3 sect. A3c, 85 pp, <http://hdl.handle.net/11681/2625> (Accessed September 8, 2020).

- Morris, V. and B. Ermold, 2015: Ceilometer (CEIL10M). 2015-11-30 to 2017-01-02, ARM Mobile Facility (AWR) McMurdo Station Ross Ice Shelf, Antarctica; AMF2 (M1). ARM Data Center, accessed 18 March 2019. <http://dx.doi.org/10.5439/1181954>.
- , 2016: *Ceilometer Instrument Handbook*. DOE/SC-ARM-TR-020, 26 pp, https://www.arm.gov/publications/tech_reports/handbooks/ceil_handbook.pdf
- Muradyan, P., and R. Coulter, 2020: *Micropulse Lidar (MPL) Instrument Handbook*. DOE/SC-ARM-TR-019, 20 pp, https://www.arm.gov/publications/tech_reports/handbooks/mpl_handbook.pdf.
- Nishimura, K., and M. Nemoto, 2005: Blowing snow at Mizuho station, Antarctica. *Philosophical Transactions of the Royal Society A: Mathematical, Physical and Engineering Sciences*, **363**, 1647–1662, <https://doi.org/10.1098/rsta.2005.1599>.
- NOAA, 1998: Training Guide in Surface Weather Observations. <https://www.weather.gov/media/surface/SFCTraining.pdf> (Accessed June 27, 2019).
- OTT HydroMet, 2016: Operating instructions Present Weather Sensor OTT Parsivel2. 70.210.001.B.E 12-1016, 52 pp, <https://www.ott.com/download/operating-instructions-present-weather-sensor-ott-parsivel2-without-screen-heating/>
- Palm, S. P., Y. Yang, J. D. Spinhirne, and A. Marshak, 2011: Satellite remote sensing of blowing snow properties over Antarctica. *Journal of Geophysical Research: Atmospheres*, **116**, <https://doi.org/10.1029/2011JD015828>.
- , V. Kayetha, Y. Yang, and R. Pauly, 2017: Blowing snow sublimation and transport over Antarctica from 11 years of CALIPSO observations. *The Cryosphere*, **11**, 2555–2569, <https://doi.org/10.5194/tc-11-2555-2017>.
- , ———, and ———, 2018a: Toward a Satellite-Derived Climatology of Blowing Snow Over Antarctica. *Journal of Geophysical Research: Atmospheres*, **123**, 10,301–10,313, <https://doi.org/10.1029/2018JD028632>.
- , Y. Yang, V. Kayetha, and J. P. Nicolas, 2018b: Insight into the Thermodynamic Structure of Blowing-Snow Layers in Antarctica from Dropsonde and CALIPSO Measurements. *Journal of Applied Meteorology and Climatology*, **57**, 2733–2748, <https://doi.org/10.1175/JAMC-D-18-0082.1>.
- Pomeroy, J. W., and D. H. Male, 1988: OPTICAL PROPERTIES OF BLOWING SNOW. *Journal of Glaciology*, **116**, 3–10, <https://doi.org/10.3189/S0022143000008996>.

- Rauber, R. M., and S. W. Nesbitt, 2018: *Radar Meteorology: A First Course*. Wiley-Blackwell, 488 pp.
- Ritsche, M. T., and J. Prell, 2011: *ARM Surface Meteorology Systems Handbook*. https://www.arm.gov/publications/tech_reports/handbooks/met_handbook.pdf (Accessed May 17, 2020).
- Rooney, J. F., 1967: The Urban Snow Hazard in the United States: An Appraisal of Disruption. *Geographical Review*, **57**, 538, <https://doi.org/10.2307/212932>.
- Sassen, K., 1977: Ice Crystal Habit Discrimination with the Optical Backscatter Depolarization Technique. *J. Appl. Meteor.*, **16**, 425–431, [https://doi.org/10.1175/1520-0450\(1977\)016<0425:ICHDWT>2.0.CO;2](https://doi.org/10.1175/1520-0450(1977)016<0425:ICHDWT>2.0.CO;2).
- , 1991: The Polarization Lidar Technique for Cloud Research: A Review and Current Assessment. *Bull. Amer. Meteor. Soc.*, **72**, 1848–4866, [https://doi.org/10.1175/1520-0477\(1991\)072<1848:TPLTFC>2.0.CO;2](https://doi.org/10.1175/1520-0477(1991)072<1848:TPLTFC>2.0.CO;2).
- Scarchilli, C., M. Frezzotti, P. Grigioni, L. De Silvestri, L. Agnoletto, and S. Dolci, 2010: Extraordinary blowing snow transport events in East Antarctica. *Clim Dyn*, **34**, 1195–1206, <https://doi.org/10.1007/s00382-009-0601-0>.
- Schmidt, R. A., 1982: Properties of blowing snow. *Reviews of Geophysics*, **20**, 39–44, <https://doi.org/10.1029/RG020i001p00039>.
- Seefeldt, M. W., G. J. Tripoli, and C. R. Stearns, 2003: A High-Resolution Numerical Simulation of the Wind Flow in the Ross Island Region, Antarctica. *Mon. Wea. Rev.*, **131**, 435–458, [https://doi.org/10.1175/1520-0493\(2003\)131<0435:HRNSO>2.0.CO;2](https://doi.org/10.1175/1520-0493(2003)131<0435:HRNSO>2.0.CO;2).
- Sengupta, M. and coauthors, 2015: Sky Radiometers on Stand for Downwelling Radiation (SKYRAD60S). 2015-11-16 to 2016-12-29, ARM Mobile Facility (AWR) McMurdo Station Ross Ice Shelf, Antarctica; AMF2 (M1). ARM Data Center, accessed 30 July 2020. <http://dx.doi.org/10.5439/1025281>.
- Shi, Y., 2015: Laser Disdrometer (LD). 2015-11-19 to 2017-01-01, ARM Mobile Facility (AWR) McMurdo Station Ross Ice Shelf, Antarctica; AMF2 (M1). ARM Data Center, accessed 13 May 2019. <http://dx.doi.org/10.5439/1498731>.
- Shiple, S. T., D. H. Tracy, E. W. Eloranta, J. T. Trauger, J. T. Sroga, F. L. Roesler, and J. A. Weinman, 1983: High spectral resolution lidar to measure optical scattering

properties of atmospheric aerosols. 1: Theory and instrumentation. *Appl. Opt., AO*, **22**, 3716–3724, <https://doi.org/10.1364/AO.22.003716>.

- Silber, I., J. Verlinde, E. W. Eloranta, C. Flynn, and D. Flynn, 2015: Reprocessed MPL data sets. 2015-12-01 to 2017-01-02, ARM Mobile Facility (AWR) McMurdo Station Ross Ice Shelf, Antarctica; AMF2 (M1). ARM Data Center, accessed 24 September 2019. <http://dx.doi.org/10.5439/1468777>.
- , ———, ———, and M. Cadeddu, 2018a: Antarctic Cloud Macrophysical, Thermodynamic Phase, and Atmospheric Inversion Coupling Properties at McMurdo Station: I. Principal Data Processing and Climatology. *Journal of Geophysical Research: Atmospheres*, **123**, 6099–6121, <https://doi.org/10.1029/2018JD028279>.
- , ———, ———, C. J. Flynn, and D. M. Flynn, 2018b: Polar Liquid Cloud Base Detection Algorithms for High Spectral Resolution or Micropulse Lidar Data. *Journal of Geophysical Research: Atmospheres*, **123**, 4310–4322, <https://doi.org/10.1029/2017JD027840>.
- Vaisala Oyj, 2004: *User Guide: Present Weather Detector (PWD22)*. M210543EN-B, 125 pp, <https://data2.manualslib.com/pdf6/123/12266/1226525-vaisala/pwd22.pdf?a46980cfe57b4a39dd259d0fd2064cb3> (Accessed September 21, 2020).
- , 2010: *User Guide: Vaisala WINDCAP Ultrasonic Wind Sensor (WS425)*. M210361EN-E, 86 pp, https://www.vaisala.com/sites/default/files/documents/WS425_User_Guide_in_English.pdf (Accessed September 21, 2020).
- , 2020: *User Guide: Vaisala HUMICAP Humidity and Temperature Probe (HMP155)*. M210912EN-D, 102 pp, <https://www.vaisala.com/sites/default/files/documents/HMP155-User-Guide-in-English-M210912EN.pdf> (Accessed September 15, 2020).
- Walden, V. P., S. G. Warren, and E. Tuttle, 2003: Atmospheric Ice Crystals over the Antarctic Plateau in Winter. *J. Appl. Meteor.*, **42**, 1391–1405, [https://doi.org/10.1175/1520-0450\(2003\)042<1391:AICOTA>2.0.CO;2](https://doi.org/10.1175/1520-0450(2003)042<1391:AICOTA>2.0.CO;2).
- Weber, N. J., M. A. Lazzara, L. M. Keller, and J. J. Cassano, 2016: The Extreme Wind Events in the Ross Island Region of Antarctica. *Wea. Forecasting*, **31**, 985–1000, <https://doi.org/10.1175/WAF-D-15-0125.1>.

- Widener, K., N. Bharadwaj, and K. Johnson, 2012: *Ka-Band ARM Zenith Radar (KAZR) Handbook*. DOE/SC-ARM/TR-106, 25 pp, https://www.arm.gov/publications/tech_reports/handbooks/kazr_handbook.pdf (Accessed May 17, 2020).
- Yang, J., and M. K. Yau, 2011: A case study of blowing snow cooling effects on anticyclogenesis and cyclolysis. *Journal of Geophysical Research: Atmospheres*, **116**, <https://doi.org/10.1029/2010JD014624>.
- Yang, Y., S. P. Palm, A. Marshak, D. L. Wu, H. Yu, and Q. Fu, 2014: First satellite-detected perturbations of outgoing longwave radiation associated with blowing snow events over Antarctica. *Geophysical Research Letters*, **41**, 730–735, <https://doi.org/10.1002/2013GL058932>.
- Zhdanov, L. A., 1977: Katabatic wind and identification of snow transfer over the Antarctic plateau by means of satellite photographs. *Antarkitka, doklady komissii*, **16**, 30–44.